

1-1-1987

The role of molecular clouds in the star formation process as observed in two grand design spiral galaxies.

Steven Donald Lord
University of Massachusetts Amherst

Follow this and additional works at: https://scholarworks.umass.edu/dissertations_1

Recommended Citation

Lord, Steven Donald, "The role of molecular clouds in the star formation process as observed in two grand design spiral galaxies." (1987). *Doctoral Dissertations 1896 - February 2014*. 1755.
https://scholarworks.umass.edu/dissertations_1/1755

This Open Access Dissertation is brought to you for free and open access by ScholarWorks@UMass Amherst. It has been accepted for inclusion in Doctoral Dissertations 1896 - February 2014 by an authorized administrator of ScholarWorks@UMass Amherst. For more information, please contact scholarworks@library.umass.edu.

UMASS/AMHERST



312066007696246

THE ROLE OF MOLECULAR CLOUDS IN THE STAR FORMATION PROCESS
AS OBSERVED IN TWO GRAND DESIGN SPIRAL GALAXIES

A Dissertation Presented

By

STEVEN DONALD LORD

Submitted to the Graduate School of the
University of Massachusetts in partial fulfillment
of the requirements for the degree of

DOCTOR OF PHILOSOPHY

September 1987

Department of Physics and Astronomy

Copyright © 1987 by Steven D. Lord
All rights reserved

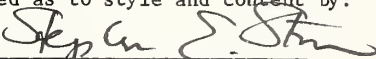
The Role of Molecular Clouds in the Star Formation Process
as Observed in two Grand Design Spiral Galaxies

A Dissertation Presented


By

STEVEN DONALD LORD


Approved as to style and content by:



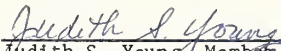
Stephen E. Strom, Chairperson




Robert L. Dickman, Member



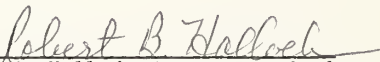
F. Peter Schloerb, Member



Judith S. Young, Member



Frank N. Bash, Outside Member



Robert Hallock, Department Head
Department of Physics and Astronomy

DEDICATION

To my Mother and Father,
for their continuous love and support.

ACKNOWLEDGEMENTS

"I've looked at clouds from both sides now,
From up and down, and still somehow
It's clouds' illusions I recall.
I really don't know clouds at all."

- Joni Mitchell ("Both Sides Now" 1967)

Sometimes my long tenure as a graduate student at the University of Massachusetts has seemed much like living within a cloud. There has been thunder and storm, darkness and gloom, and at other times airy aloofness, with the feeling of never quite touching ground. But, as with every really good cloud, there has been a silver lining: the people I've had the privilege to get to know, work with, or work along side of while here.

Steve Strom, the committee chairman has set the scope of my work, allowing me the independence to explore areas of interest while simultaneously nudging me back on track toward important issues and to completion. His "can-do" attitude, pragmatism and enthusiasm have assisted me greatly in persevering. Judy Young, the committee chairwoman, has served no lesser a role, both as a model of cheerful industry, and a believer in tackling tough problems and carefully but efficiently dispatching them. While I never approached their productivity, I shudder to think of how long my natural tendency to dwell on details would have held me back without their examples before me.

When, under Judy's instigation, the first grand wave of CO galaxy observations commenced at the Five College Radio Astronomy Observatory, she handed me M51 as a research problem. This simple act has led me to more reading, studying, and head scratching than I ever would have imagined. It allowed me to gain an ever growing respect for and fascination with those things we blithly call "normal galaxies" and the amazing half century of effort that has gone into fathoming them. There could not have been a better or more difficult place to start.

The idea that the Five College Radio Observatory was providing a unique research tool was echoed by the other committee members: Frank Bash; Pete Schloerb; and Bob Dickman. They each helped me in the areas of their expertise and tried hard to keep me honest (successfully, I think) and succinct (less successfully, I think). The scheduling committee, headed by FCRAO Director Bill Irvine were generous in their allotment of the necessarily long hours of telescope time which such observations require.

I am indebted to those people who provided me with unpublished data. These include, (M51): Rob Kennicutt; Holland Ford; Arnold Rots; Thijs van der Hulst, (M83): Reggie DuFour; Marc Ondrechen; Michele Kaufman; Ken Rumstay; Ray Talbot, (Calibration): Jeff Kenney and Dave Taylor. Very helpful discussions were had with Jeff Kenney, Rob Kennicutt, Bill Waller, Bill Dent, John Kwan, Kevin Olson, Susan Kleinmann, as well as the committee members. Jeff Kenney, Bill Waller, and Kevin Olson took an interest in the work, and found the time out of their own heavy schedules to offer invaluable criticism.

One of my obstacles in this labor has been my inability to spell English words in the manner normally expected. Many people helped me edit, although I'd often rewrite sections and redouble my errors. I'd like to thank these folks for their willing response to my often last minute requests: Jeff Kenney, Bev Smith, Alex Wilce, Silvie Cabrit (who spells better in her second language than I in my first), Lisa Prato and Sue Madden. Judy also helped me greatly with organization and editing.

I was able to produce this document on an ailing word processor only with the tactical support of Sally Rule, Denise Kuzmeskus and Jackie Golonka. They helped me with a myriad of important details. Also, Sally has kept me smiling non-stop over the years with her contagious cheer and I salute her with a graceful bow.

The Appendices are dedicated to Silvie Cabrit, as promised, who lost hers during their writing.

If I listed all those who have provided me with moral support, it would look like the departmental register, so I'll just say thanks to you all. Lodgings, companionship, and sound advice came from Bill Dent and Sue Madden, who, along with Alex Wilce, helped me finish, but made me sad to go. But we will all dance again.

Finally, I thank my parents, Don and Sue Lord, for giving me their continuous love, support, and encouragement, and for keeping me from starving while I pursued my goals. Thanks.

ABSTRACT

The Role of Molecular Clouds in the Star Formation Process
as Observed in two Grand Design Spiral Galaxies

(September 1987)

A Dissertation Presented

By

Steven Donald Lord B.S. Tufts University

M.S. University of Massachusetts

Ph.D. University of Massachusetts

Directed by: Stephen E. Strom

ABSTRACT

We have compared the molecular, neutral and ionized hydrogen distributions in two nearby spiral galaxies. To estimate H_2 surface densities we acquired observations of the CO ($J = 1 \rightarrow 0$) transition in 60 positions to a radius of $135''$ in the Sbc galaxy M51 (NGC 5194), and in 21 positions to a radius of $150''$ in the SAB galaxy M83 (NGC 5236) using the 13.7 m telescope of the Five College Radio Astronomy Observatory. The molecular component of the ISM was found to strongly dominate over the HI component in each galaxy. Extinction corrected $H\alpha$ intensities were used to compute the detailed massive star formation rates (MSFRs) in each galaxy. Estimates of the MSFR, gas density, and the ratio of these quantities, the massive star formation efficiency (MSFE), were then examined.

In M51, the spiral arms exhibit an excess gas density of 1.4 - 1.6 times the interarm values. The MSFR contrast between the arms and interarms, measuring between 1.5 and 2.3 at the same resolution, exceeds the gas density contrast and implies a nonlinear relationship between star formation and gas surface density on the spiral arms. This follows the predictions of the cloud-cloud collision scenario of star formation which relies on the occurrence of orbit crowding to bring clouds into close proximity. We note that the regions exhibiting the highest MSFEs are those in the spiral potential minimum inward of $R=124''$, and those regions outward of $R=124''$ thought to be experiencing orbit crowding due to tidal distortion caused by the close passage of M51's companion galaxy.

The total (arm and interarm) gas content and massive star formation rates in concentric annuli in the disk of M51 were computed. The two quantities fall off together with radius, yielding a relatively constant MSFE with radius. This is consistent with the increased MSFE on the arms in that the majority of the gas shows a constant MSFE. The resulting time scale for gas depletion (total SFE^{-1}) in the disk is $2.5 \pm 0.5 \times 10^9$ yr assuming a Salpeter-like initial mass function.

In M83, the molecular gas component of the inner disk mimics the bar morphology. In this galaxy there is the suggestion of enhanced star formation at the ends of the central bar due to the compression of cloud orbits found there. The gas depletion time scale is $1.2 \pm 0.3 \times 10^9$ yr.

CONTENTS

ACKNOWLEDGMENTS	v
ABSTRACT	viii
LIST OF TABLES	xiii
LIST OF FIGURES	xiv
Chapter	
I. INTRODUCTION	1
a) Motivation	1
b) Summary of Chapters	5
c) Some Definitions	7
II. OBSERVED AND DERIVED QUANTITIES	8
a) CO Observations and Molecular Gas Densities	8
b) HI Observations	16
c) H α Fluxes and Star Formation Rates	20
III. ANALYSIS AND RESULTS	28
a) Point by Point Comparisons	28
b) Azimuthal and Radial Averages	34
c) The Spiral Pattern	48
i) The degree of arm coupling	48
ii) The spiral phase diagram	54
d) The Inner 60"	66
e) Conclusions	72
IV. DISCUSSION OF THE STAR FORMATION EFFICIENCY	75
a) Introduction	75
b) The High Star Formation Efficiency on M51's Arms	76
i) Insupportable mass growth	76
ii) Cloud collision model	77
iii) The collision rate	78
c) The Radial Dependence of the Star Formation Efficiency	82
i) A model dependent on the velocity of gas through the spiral density wave	85
ii) A model dependent on the pressure of the ISM	88
d) A Linear Model with a Constant Star Formation Efficiency in Time	89
e) The Region R=130"	93

V. KINEMATIC DEPARTURES IN THE FAR NORTH	96
a) The Observations	96
b) Star Formation Rates	97
c) Far North Velocity Reversal	100
d) The Tidal Encounter Model	105
e) Problems With the Model	108
VI. CONCLUSIONS	111
a) Gas Densities and Star Forming Rates in Individual Locations and in Azimuthal Averages	111
b) Spiral Structure	112
c) Kinematics	113
VII. OBSERVATIONS OF M83	114
a) Introduction	114
b) CO Observations	115
c) HI Observations	128
d) H α Fluxes and Star Formation Rates	129
VIII. ANALYSIS AND RESULTS	134
a) Point By Point Comparisons	134
b) Averaged Values	140
c) Empirical Versus Observed Star Formation Efficiencies	149
d) Discussion and Conclusions	152
i) The previous study	152
ii) The implications of our results	158
e) A Comparison with M51	162
APPENDIX A. SUPPLEMENTARY ERROR ANALYSIS FOR M51	167
a) Introduction	167
b) The Resolution Problem	167
c) Molecular Cloud Masses from Integrated CO Intensities	171
i) Empirical Results	171
ii) Conversions using a uniform sample	172
iii) A different cloud population on the arms ?	175
d) Star Formation Rates from H α Brightnesses	176
i) Introduction	176
ii) The possible paths for a Lyman continuum photon ..	177
iii) H α extinction correction	180
iv) The star formation rate conversion	183
v) Choice of an initial mass function	195
e) Summary	206
APPENDIX B. MASS INFALL MODEL FOR M51	209
a) Introduction	209
b) Formulation	210

APPENDIX C. EXCESS EMISSION DIAGRAMS FOR M51	215
BIBLIOGRAPHY	222

LIST OF TABLES

1	Observed and Corrected Parameters	13
2	Derived Quantities	18
3a	Azimuthal Mean Values	32
3b	Sector Mean Values	32
4a	Linear Correlations Between H α Flux and Gas Surface Density ..	37
4b	Linear Correlations of the Spiral Pattern with Emission Excesses	52
5a	Star Formation Rate Model Fits	61
5b	Star Formation Rates from Arm and Interarm Terms	65
6	H α and CO Emission in Three Central Locations	71
7	Summary of Arm and Interarm Parameters	73
8	Kinematic and Derived Parameters for Positions Along $\varphi_{\text{sky}} = 23^\circ$	101
9	Global Parameters for M83 (NGC 5236)	117
10	Observed and Corrected Parameters	120
11	Derived Quantities	122
12a	Azimuthal Mean Values	146
12b	Sector Mean Values	146
13	Empirical Star Formation Efficiencies for M83	151
14	M83 Major Axis Peak Velocities	153
15	Initial Mass Functions	187
16	Gas Infall Model Results	214

LIST OF FIGURES

1	H-alpha M51 Image of Hodge and Kennicutt (1983) with 8" smoothing	10
2	I_{CO} , HI and $f_{H\alpha}$ Brightness Distributions as a Function of Radius in the Plane of the Galaxy	29
3a	The $f_{H\alpha}$ Brightness Versus the Total Gas Surface Density (10^{20} Protons cm^{-2}) at 27 positions	35
3b	The Azimuthally Averaged $f_{H\alpha}$ Brightness Plotted Against N_p (10^{20} Protons cm^{-2}) for Eight Radial Bins	38
4	The Azimuthally Averaged CO, H α , HI, and Blue Light Distributions in the Disk of M51	41
5a	The Average H α and CO Emission within 8 Sectors of M51's Disk	44
5b	The Correlation of Gas Surface Density with Star Formation Rates in Eight Sectors	46
6	The Fractional Excess in I_{CO} , H α , HI and Star Formation Efficiency Shown Against η_{arm}	50
7	The Gas Densities, Star Formation Rates, and Star Formation Rates and Star Formation Efficiencies for two Annuli	56
8	The Observed and Modeled Star Formation Efficiencies Plotted Against Galactic Radius	83
9	Four CO Spectra Taken Along $\theta_{sky} = 23^\circ$	98
10	The Spatial-Velocity Diagram for Eight Positions along the $\theta_{sky}=23^\circ$ Diameter Through the Disk	102
11	The Raw Surface Brightness of the Continuum Subtracted H α Image of M83	123
12	The Integrated CO Intensity Contours for M83	123
13	The I_{CO} (this study) and $f_{H\alpha}$ (Talbot et al. 1979) Brightness Distributions as a Function of Radius in the Plane of M83 ..	136
14	The $f_{H\alpha}$ Brightness Versus the Gas Surface Density (10^{20} Protons cm^{-2}) at 21 Positions	138

15	The Gas Surface Density in HI Against the Density in H ₂	141
16	The Azimuthally Averaged CO, H α , and HI, Distributions in the Disk of M83	143
17	The Average H α and CO Emission within 8 Sectors of M83's disk	147
18	The Observed and Modeled Star Formation Efficiencies Plotted Against Galactic Radius	154
19	M51 and M83 Integrated H α Luminosity and Gas Mass	163
20	The Radial H α Distribution in M51 Under Various Resolutions ...	169
21	The Terms Used in Computing the Star Formation Rate Conversion Factor C	189
22	The Conversion Factor, C, Against the High-Mass Cutoff for Four Initial Mass Functions	191
23	The Conversion Factor, C, Against the Low-Mass Cutoff for Four Initial Mass Functions	193
24	The Fraction of Total Mass in High Mass Stars Against High-Mass Cutoff for Four Initial Mass Functions	196
25	The Fraction of Total Mass in High Mass Stars Against Low-Mass Cutoff for Four Initial Mass Functions	198
26	Initial Mass Function Discrimination Method	201
27	The Fractional CO Emission Above the Azimuthal Mean in M51	216
28	The Fractional H α Emission Above the Azimuthal Mean in M51	218
29	The Fractional SFE Above the Azimuthal Mean in M51	220

CHAPTER I

INTRODUCTION

a) Motivation

Since the earliest observations of molecular clouds in galaxies (Rickard et al. 1975), there has been a great interest and observational effort put forth to determine the extent to which molecular clouds are confined to spiral arms in spiral galaxies. The reason for this is severalfold. First, since it is generally accepted that stars form in molecular clouds, the optical spiral patterns seen in galaxies were thought to possibly reflect a spiral pattern in the underlying distribution of molecular mass. Specifically, the spiral density wave believed responsible for the spiral pattern might provide a mechanism for molecular cloud growth through an increased incidence of cloud-cloud collisions and coalescence. Secondly, if the density wave in a galaxy were responsible for triggering star formation, either through the action of density wave shock fronts or those of cloud collisions, then the subsequent star formation and disruption of molecular clouds might prevent there being much molecular mass in the interarm regions of spiral galaxies.

Despite these reasonable expectations, the results of numerous studies of molecular clouds in spiral galaxies have shown a general lack of confinement of molecular clouds to spiral arms. While these results, based on extragalactic observations of galaxies employing 0.75' to 1.1' apertures, may have at first appeared to be the effect of

insufficient angular resolution, more recent, higher resolution studies have confirmed the general absence of molecular cloud confinement to spiral arms. Additionally, it has been pointed out (Scoville and Hersh 1979) that the degree of confinement depends on the ratio of atomic to molecular gas. They argue that if the H_2 is the dominant component of the interstellar medium of a galaxy, and is in equilibrium with HI, then it is not possible to confine H_2 to small regions in azimuth in the galactic disk, and still maintain a steady state system.

The galaxies which are sufficiently nearby and face-on to be useful in answering questions regarding molecular gas distributions in the presence of spiral structure are M31, IC 342, NGC 6946, and M51. The first indication of CO spiral structure in an external galaxy was found in M31 (Combes et al. 1977a,b; Stark 1979; Ryden and Stark 1986), where numerous observations indicate that in the outer disk, the CO emission is concentrated in a ridge which is coincident with optical arms. The observed contrast between the molecular surface density on and off the arms is 7 ± 4 to 1, as inferred from Figure 4 of Ryden and Stark (1986). But, of all the galaxies surveyed thus far, this high arm/interarm contrast appears to be peculiar to M31.

What is unusual about M31? The H_2 surface density in Andromeda is quite low compared to that in other Sb and Sc galaxies (c.f. Stark 1979; Morris and Rickard 1982; Young 1986), and also low relative to the HI surface density in M31 (Brinks 1984). Thus, if H_2 and HI are in equilibrium, the high value observed for the

arm/interarm CO contrast may be common primarily to galaxies with relatively low molecular surface densities.

The remaining candidate galaxies in which to determine the CO spiral structure are some of the more distant, face-on spiral galaxies: IC 342, NGC 6946 and M51. Observations of these galaxies with 0.75' to 1.1' resolution (Rickard and Palmer 1981; Young and Scoville 1982; Scoville and Young 1983, hereafter SY) showed no obvious correlation between the peaks in the molecular emission and spiral structure. In these galaxies the dominant feature of the azimuthally averaged CO distribution is the central peak and large intensity decrease with radius. Even when the azimuthal variations relative to the mean were analyzed (Young and Scoville 1982; SY) no global evidence was found for large enhancements in the molecular emission on the arms. In the outer disk of M51, SY found at best two locations on arms with a 1.5:1 enhancement in the CO emission relative to the mean value at that radius.

More recent CO observations in M51 have been made at 33" resolution (Rydbeck, Hjalmarson, and Rydbeck 1985, henceforth RHR) and 7" resolution (Lo et al. 1987). In the study of RHR, a CO enhancement of only 20% was found in the arms. The contrast is more apparent after subtracting the underlying exponential distribution, which contributes 75% of the emission. And although Lo et al. do observe ridges of CO emission coincident with arms in the inner disk of M51, their interferometric observations are missing over 70% of the total

emission, most of which is "resolved-out", and thus represents the extended, underlying distribution. This conclusion is verified by a series of single dish measurements taken at 15" resolution (Y. Sofue 1986, personal communication). Thus, in M51 as in the majority of luminous late-type spiral galaxies studied, any spiral structure in the molecular distribution appears to be a secondary property and not the dominant feature.

Why, then, are the spiral arms so apparent in galaxies, if the underlying distribution of star forming material is relatively smooth? The answer may lie in the efficiency with which stars form in the arm regions in a spiral galaxy. A goal of this study (Part One) is to determine the star formation efficiency across the disk of M51, and to ascertain whether the efficiency is higher in spiral arms. We will relate our results to other local galactic properties including the stellar surface density, gas kinematics, the spiral density wave, and finally the tidal forces invoked by the companion galaxy's (NGC 5195) close passage causing perturbed orbits outward of $R = 135''$.

The second part of this work (Part Two) comprises an analysis of the molecular distribution and star formation in the inner disk of the luminous southern barred spiral galaxy M83 (NGC 5236, SAB(s)). We determine the manner in which the central bar potential in this galaxy organizes the distribution of molecular clouds. Efficient massive star formation is seen here to occur throughout the galaxy's inner disk, and we present evidence suggesting that the highest star forming

efficiencies in this galaxy are to be found in the regions where cloud streamlines converge.

b) Summary of Chapters

In Chapter II we present the various data sets used for the M51 study: the CO observations of this work and the H α and HI data from the literature. We review the use of integrated CO intensity as an indicator of H₂ surface density, and H α flux as an indicator of massive star formation rates.

We produce radial and azimuthal averages of the data in Chapter III, and calculate the detailed and averaged star formation efficiencies. Finally, the data are subjected to algorithms that display the properties of the spiral pattern in M51.

Chapter IV relates the results of Chapter III to current theory. High massive star formation efficiencies on the spiral arms are interpreted as evidence for star formation triggered by cloud-cloud collisions. The star formation efficiency as a function of radius is found not to agree with the predictions of two other models of galaxian star formation. Finally, the star formation efficiency averaged over the lifetime of the disk is computed, and is found to be significantly smaller than the current efficiency. Explanations of this result are offered, including the temporary efficiency enhancement due to the tidal influence of the companion galaxy NGC 5195.

The tidal encounter disturbs the kinematics in M51's outer disk, as shown in Chapter V. Here we present the first observations of such velocity effects seen in the molecular gas. Problems with the current model of the interaction of the two galaxies are given.

Chapter VI contains a summary of the results of Part One.

Chapters VII and VIII present our data analysis for M83, and parallel the topics of Chapter II and III. Again we have used original CO observations along with $H\alpha$ and HI results from the literature. We show that in M83 there is a large uncertainty in applying extinction corrections to the $H\alpha$ data. The distribution of gas for $R < 150''$ is found to be concentrated on the central bar, and a higher star formation efficiency with radius is seen in M83 than was observed for M51. Also, as in the case of M51, the time averaged efficiencies are less than the current ones. The high current efficiencies derived from the $H\alpha$ flux measurements may be caused by an initial mass function which is unusually weighted toward the production of massive stars. Finally, M83 and M51 are compared.

Appendix A discusses the conversions to H_2 surface densities and to star formation rates in detail. In Appendix B, we show that a gas infall model will not explain the inequality between the current and past star formation efficiencies in M51. In Appendix C we display the $H\alpha$ and CO surface emission in the disk of M51 obtained after subtracting off the axisymmetric distributions.

c) Some Definitions

Throughout this work we use σ_p ($M_0 \text{ pc}^{-2}$) for the gas surface density, SFR ($M_0 \text{ pc}^{-2} \text{ Gyr}^{-1}$) for the star formation rate, and SFE (Gyr^{-1}) = SFR/σ_p for the star formation efficiency, where $\text{Gyr} = 10^9 \text{ yr}$. The quantity σ_p represents total ($\text{HI} + \text{H}_2 + \text{He}$) surface density unless specifically qualified, e.g. $\sigma_p(\text{HI})$, and $\sigma(\text{H}_2)$ will be taken to implicitly include the helium contribution. The advantage of studying surface densities is that these quantities are derived from surface brightnesses and thus are independent of the distance to the galaxy.

The SFE may most simply be understood as the inverse of the gas depletion time if the SFR remains constant and there is no gas infall or recycling.

For both galaxies, we also refer to the region $15'' \leq R \leq 60''$ as the "central region", the region $60'' \leq R \leq 160''$ as the "inner disk", and the region beyond $R=160''$ as the "outer disk". The variables R and Θ will refer to the plane of the sky coordinates while R_{gal} and Θ_{gal} refer to coordinates in the galaxy's frame, as determined by the systemic parameters.

The adopted systemic parameters for M51 are: inclination angle $i = 20^\circ$ (Tully 1974b), position angle, P.A. = -10° (Tully 1974b), and distance, $D = 9.6 \text{ Mpc}$ (Sandage and Tammann 1975). The central position used here is α (1950) = $13^{\text{h}} 27^{\text{m}} 46^{\text{s}}.327$, δ (1950) = $47^\circ 27' 10''.25$ (Ford et al. 1985).

CHAPTER II

OBSERVED AND DERIVED QUANTITIES

a) CO Observations and Molecular Gas Densities

Here we present a fully sampled CO map of the inner disk of M51 made in 60 positions with the 13.7 m telescope of the Five College Radio Astronomy Observatory (FCRAO). Sixteen of the positions presented in SY were used in this work, and an additional 47 new positions in this galaxy were observed, 19 of them lying in the inner disk and beyond. The new observations were made at the FCRAO between December 1983 and June 1985 using a slightly smaller beamwidth, HPBW = 45", an improved cooled mixer receiver, $T_{SSB} = 200$ K at 115.2712 GHz, and with integrations (1.5 hours per position) to significantly lower noise values, rms = 0.013 K, after smoothing to 12 km s^{-1} . At the CO $J=1 \rightarrow 0$ frequency (115.2712 GHz) the mean system temperature during the observations was 950 K.

The central region was oversampled in a 5 by 5 grid with spacings of 22.5" in the east and north directions. Each five positions shared two common references (10' east and west) with an observing scheme of 15 seconds at each of five positions on source, followed by 20 seconds off. These 25 spectra were acquired in parallel over several days, which allowed for sensitive pointing precision (rms = 3") because in the inner disk the line profiles change markedly with positional offset. Calibration was accomplished via the chopper wheel method and the spectra were corrected for forward scattering and spillover ($\eta_{fss} =$

0.70) in order to obtain T_R^* . An estimate of τ_c , the coupling of the main beam to the source was obtained for each position using a non-axisymmetric model of the galaxy's CO brightness and these values were used to produce T_R measurements at each position. The backend consisted of a 1 MHz x 256 channel filterbank receiver which provided 2.6 km s^{-1} resolution. The line spectra were smoothed to 12 km s^{-1} , and linear baselines removed.

The observed positions are shown superposed on the $H\alpha$ map provided for this study (Hodge and Kennicutt 1983) in Figure 1, with circles denoting the half-power beam width in the inner and outer disk and crosses in the central region. The observed locations and the integrated CO intensities, $I'_{CO} = \int T_R^* dv$, and $I_{CO} = \int T_R dv$, are given in Table 1. Errors in the integrated CO intensity at each position were calculated by adding in quadrature the uncertainties associated with baseline fitting (σ_{bl}), calibration (σ_{cal}), and the rms noise (σ_n). The values for σ_{bl} and σ_n were estimated for each individual position, and the mean values for these errors are: $\sigma_n = 0.7 \text{ K km s}^{-1}$, $\sigma_{bl} = 1.2 \text{ K km s}^{-1}$, while σ_{cal} is estimated to be 10% (Kenney 1987). The total error, σ_{tot} , is given in Table 1.

Our conversion of CO integrated intensity to an $H_2 + He$ mass surface density, expressed as N_p (protons) cm^{-2} at each beam position, was based on both empirical and theoretical results which imply a direct proportionality between these two quantities. These studies are discussed in Appendix A.c, and summarized below. In this work we adopt a conversion given by

Figure 1. The $H\alpha$ M51 image of Hodge and Kennicutt (1983) with 8" smoothing. Shown superposed are the positions of the CO observations, with the inner 25 beam centers indicated with x's and the outer 35 positions indicated with 45" HPBW circles.

RA (MIN)



TABLE 1 (NOTES)

Column (1), Position index.

Columns (2 and 3), $\Delta\alpha$ and $\Delta\delta$ are the right ascension and declination offsets of the beam center locations in arc seconds from the central position given in §I.

Columns (4 and 5), R_{sky} and θ_{sky} are the radius and position angle from North of the beam center locations measured in arc seconds and degrees respectively.

Columns (6 and 8), R'_{gal} , θ_{gal} are the beam center locations in the plane of the galaxy in arc seconds and degrees from the principal axis ($\theta_{\text{sky}} = -10^\circ$) respectively.

Column (7), R_{gal} is the beam-weighted mean radius of an observation, excluding the galaxy's inner 15".

Column (9), I'_{CO} is the integrated CO intensity. $I'_{\text{CO}} = \int (T_{\text{A}}^* / \eta_{\text{fss}}) dv = \int T_{\text{R}}^* dv$ in K km s⁻¹.

Column (10), η_{c} is the modeled, source dependent, main beam coupling coefficient.

Column (11), I_{CO} is the corrected integrated intensity, $I_{\text{CO}} = \int (T_{\text{R}}^* / \eta_{\text{c}}) dv = \int T_{\text{R}} dv$ in K km s⁻¹. The CO flux, S_{CO} , in Jy km s⁻¹ is given by $S_{\text{CO}} = I_{\text{CO}} \times 31 \text{ Jy/K}$.

Column (12), $f'_{\text{H}\alpha}$ is the raw PDS image brightness in units 10⁻¹⁶ erg cm⁻² s⁻¹ arcsec⁻².

Column (13), N is the number of cataloged HII regions within 0.75 HPBW's of the beam center.

Column (14), $f_{\text{H}\alpha}$ is the extinction corrected $f'_{\text{H}\alpha}$ in units of 10⁻¹⁶ erg cm⁻² s⁻¹ arcsec⁻², with error term from the extinction uncertainty and columns 12 and 13.

Column (15), is the integrated 21-cm line flux per interpolated 45" beam, in Jy km s⁻¹.

TABLE I
OBSERVED AND CORRECTED PARAMETERS

ln.	$\Delta\alpha$	$\Delta\delta$	R_{sky}	Θ_{sky}	R'_{gal}	R_{gal}	Θ_{gal}	I'_{CO}	n_c	$I_{\text{CO}} \pm \alpha_I$	$f'_{\text{H}\alpha}$	N	$f_{\text{H}\alpha} \pm \alpha_f$	f_{HI}
(1)	(2)	(3)	(4)	(5)	(6)	(7)	(8)	(9)	(10)	(11)	(12)	(13)	(14)	(15)
1	45	45	64	45	66	69	57	16	0.72	22.2 ± 2.7	2.0	10	7.2 ± 1.5	1.25
2	23	45	50	27	52	56	38	14	0.72	20.0 2.4	4.2	18	14.8 2.5	1.38
3	0	45	45	0	45	51	11	17	0.72	23.8 3.4	5.0	13	18.3 3.1	1.50
4	-23	45	50	333	51	55	342	2	0.72	17.3 2.1	3.4	12	13.6 2.6	1.48
5	-45	45	64	315	65	68	323	11	0.73	14.9 1.8	1.9	12	8.8 1.4	1.51
6	45	23	50	63	53	58	74	14	0.72	19.4 2.5	2.5	22	8.5 1.5	1.24
7	23	23	32	45	33	42	57	14	0.72	19.6 2.5	5.6	20	18.4 3.8	1.29
8	0	23	23	0	23	36	11	19	0.72	25.8 3.4	6.5	8	21.5 7.6	1.33
9	-23	23	32	315	33	42	323	19	0.72	26.0 3.6	4.1	8	14.0 4.9	1.34
10	-45	23	50	297	52	57	305	11	0.72	15.7 2.4	1.7	9	6.8 1.7	1.41
11	45	0	45	90	48	53	99	22	0.70	31.0 4.0	2.5	13	8.5 2.0	1.19
12	23	0	23	90	24	37	99	27	0.70	38.0 5.3	5.0	12	16.3 4.9	1.17
13	0	0	0	0	0	30	0	31	0.69	44.9 6.7	6.2	10	20.0 7.1	1.17
14	-23	0	23	270	24	37	279	25	0.70	36.1 5.1	4.3	6	14.0 6.3	1.18
15	-45	0	45	270	48	53	279	18	0.71	25.2 4.0	1.7	5	5.7 2.4	1.23
16	45	-23	50	117	52	57	125	18	0.70	26.1 3.4	1.7	8	6.8 1.7	1.25
17	23	-23	32	135	33	42	143	35	0.69	50.5 6.6	2.6	7	8.9 3.3	1.21
18	0	-23	23	180	23	36	191	36	0.69	52.6 6.3	3.2	7	10.5 4.2	1.16
19	-23	-23	32	225	33	42	237	28	0.69	40.4 6.9	2.7	5	9.0 4.0	1.07
20	-45	-23	50	243	53	58	254	14	0.71	20.3 3.5	1.2	4	4.1 1.8	1.06
21	45	-45	64	135	65	68	143	14	0.71	19.9 2.4	1.4	10	6.5 1.1	1.34
22	23	-45	50	153	51	55	162	19	0.70	27.1 3.3	1.6	9	6.6 1.4	1.32
23	0	-45	45	180	45	51	191	19	0.69	28.0 4.2	1.7	9	6.6 1.6	1.20
24	-23	-45	50	207	52	56	218	23	0.70	32.9 3.9	1.5	6	5.8 1.6	1.05
25	-45	-45	64	225	66	69	237	7	0.73	10.2 1.4	0.8	5	3.2 0.9	1.03
26	0	90	90	0	90	93	11	6	0.76	7.9 1.2	1.4	13	5.8 0.8	1.48
27	34	83	90	23	92	94	34	6	0.75	8.0 1.0	1.1	9	4.1 0.7	1.25
28	64	64	90	45	94	96	57	10	0.72	14.1 2.1	2.2	15	8.7 1.2	1.36
29	83	34	90	68	96	97	78	13	0.72	17.9 2.3	1.5	13	6.1 0.9	1.41
30	90	0	90	90	96	98	99	7	0.75	9.3 1.4	1.2	7	5.5 1.0	1.41
31	83	-34	90	113	94	96	121	10	0.73	13.5 1.8	1.0	5	4.8 1.0	1.43
32	64	-64	90	135	92	95	143	11	0.72	15.3 2.3	0.8	4	3.6 0.9	1.33
33	34	-83	90	158	90	93	167	10	0.73	13.9 1.9	0.7	5	3.3 0.7	1.22
34	0	-90	90	180	90	93	191	6	0.77	7.2 1.1	0.8	6	3.7 0.7	1.11
35	-34	-83	90	203	92	94	214	11	0.73	15.3 2.3	1.0	6	4.2 1.1	1.21
36	-64	-64	90	225	94	96	237	9	0.74	12.4 1.9	1.7	4	6.6 1.7	1.28
37	-83	-34	90	248	96	97	258	6	0.77	7.2 1.1	0.7	6	2.8 0.6	1.22
38	-90	0	90	270	96	98	279	6	0.75	8.4 1.3	0.6	7	2.5 0.5	1.38
39	-83	34	90	293	94	96	301	10	0.72	14.1 1.7	0.6	6	3.0 0.6	1.53
40	-64	63	90	315	92	95	323	5	0.75	6.5 1.0	1.0	5	4.8 1.0	1.58
41	-34	83	90	338	90	93	347	7	0.74	10.0 1.2	1.3	12	5.9 0.8	1.60

TABLE 1 (CONT.)

i_n	$\Delta\alpha$	$\Delta\delta$	R_{sky}	Θ_{sky}	R'_{gal}	R_{gal}	Θ_{gal}	I'_{CO}	η_c	$I_{\text{CO}} \pm \sigma_I$	$f'_{\text{H}\alpha}$	N	$f_{\text{H}\alpha} \pm \sigma_f$	f_{HI}
(1)	(2)	(3)	(4)	(5)	(6)	(7)	(8)	(9)	(10)	(11)	(12)	(13)	(14)	(15)
42	0	135	135	0	135	137	11	4	0.77	5.4 \pm 0.8	1.7	17	5.2 \pm 0.7	1.46
43	52	125	135	23	138	139	34	9	0.71	12.7 1.7	6.0	18	17.9 2.4	1.38
44	96	96	135	45	141	142	57	8	0.74	10.2 1.5	3.8	15	12.9 1.8	1.90
45	125	52	135	68	143	145	78	6	0.75	8.6 1.1	1.6	15	5.5 0.8	1.76
46	135	0	135	90	143	145	99	8	0.73	10.6 1.6	0.8	4	2.5 0.7	1.53
47	125	-52	135	113	141	143	121	5	0.76	6.4 1.1	0.5	5	1.7 0.4	1.42
48	96	-96	135	135	138	140	143	2	0.81	3.0 0.5	2.0	10	5.7 1.0	1.33
49	52	-124	135	158	135	137	167	4	0.75	5.7 0.7	0.8	3	2.2 0.8	1.15
50	0	-135	135	180	135	137	191	5	0.76	6.8 1.0	0.8	5	2.6 0.6	1.06
51	-52	-125	135	203	138	139	214	8	0.72	10.9 1.4	1.4	4	4.7 1.3	1.56
52	-96	-96	135	225	141	142	237	8	0.72	10.9 1.6	3.3	3	11.1 3.4	1.57
53	-125	-52	135	248	143	145	258	4	0.77	5.4 0.8	0.4	3	1.7 0.5	1.34
54	-135	0	135	270	143	145	279	4	0.77	5.4 0.8	0.2	7	0.7 0.1	1.43
55	-125	52	135	293	141	143	301	7	0.71	10.3 1.3	0.1	3	0.3 0.1	1.56
56	-96	96	135	315	138	140	323	5	0.75	6.9 1.0	0.4	4	1.3 0.4	1.82
57	-52	125	135	338	135	137	347	4	0.76	4.7 0.6	1.5	10	4.7 0.8	1.77
A	95	229	248	23	252	253	34	3	0.70	4.8 0.6	0.5	12	0.6 -	0.88
B	86	208	225	23	229	230	34	3	0.70	4.0 0.6	0.3	4	0.4 -	1.01
C	54	144	154	21	156	158	32	3	0.70	4.8 0.6	4.8	4	14.4 4.0	1.01

$$N_p(\text{H}_2) = 6 \pm 3 \times 10^{20} I_{\text{CO}} \cos(i) \quad (\text{II.1})$$

with the constant $b = (6 \pm 3) \times 10^{20}$ in units of protons cm^{-2} ($K[T_R] \text{ km s}^{-1}$) and i being the galaxy's inclination. Since η_c is near unity for Milky Way molecular cloud observations made at FCRAO ($T_R = T_R^*$), while η_c is typically about 0.70 for extragalactic observations, we convert our temperature units to $T_R = T_R^* / \eta_c$ prior to estimating N_p .

The uncertainty of the conversion factor depends largely on the extent to which extragalactic molecular cloud populations statistically resemble the well-studied Milky Way cloud population, and on whether the virial mass ($M \sim \Delta v^2 \ell$) of Milky Way clouds actually represents their true mass. Furthermore, on the basis of a theoretical derivation of the conversion factor b , Dickman, Snell and Schloerb (1986) point out that a constant b may only be applied to an ensemble of clouds when the mean cloud radiation temperature, $\langle T \rangle$, is constant as well. In the general case they find that b is proportional to $\langle T \rangle^{-1}$. We must therefore caution, that by applying a constant b to all regions of M51's disk, we may be overestimating N_p in those regions containing significant numbers of heated clouds. Since our results deal explicitly with measurements of the star forming efficiency in various regions, and $\text{SFE} \sim N_p^{-1}$, we may underestimate the true efficiency in regions where massive star formation, and thus cloud heating, can occur.

b) HI Observations

The 21 cm HI flux in each beam position was estimated using the unpublished VLA observations of Dr. Arnold Rots and collaborators (1985, personal communication). These data comprised 100 synthesized line profiles arranged in a 10 x 10 grid centered on the nucleus, with a resolution of 40" and an oversampled spacing of 20". We have integrated these profiles and interpolated the flux values to achieve the same spatial sampling scheme as that used for the CO and H α observations, with values given in Table 1. The data are of high quality ($S/N \approx 40$) and we find the error term for these observations negligible for the purposes of this study.

The HI line fluxes were converted to number surface densities by

$$N_{\text{HI}} = 2.95 \times 10^{10} \Omega^{-1} \int S_{\nu} dv \cos(i) \quad (\text{II.2})$$

after Verschuur (1974, p. 29), with N_{HI} in cm^{-2} , S_{ν} in mJy, v in km s^{-1} , and Ω , the beam area, in steradians. The 40" beam subtends 2.9×10^{-8} steradians. Only for $R > 135''$ does the HI mass surface density become as high as 20% of the H_2 mass surface density derived from our CO observations. While 20% variations in N_{HI} are seen at this radius, these contribute only marginally ($\pm 5\%$) to the total gas mass surface density. We defer presentation and discussion of the unsmoothed HI data and flux variations to Rots and collaborators. We have computed the total gas surface density at each position, and display this quantity in units of N_{p} (protons cm^{-2}) in Table 2 as well

TABLE 2 (NOTES)

Column (1), Position index.

Columns (2 and 3), R_{sky} and θ_{sky} are the radius and position angle from North of the beam center locations measured in arc seconds and degrees respectively.

Column (4), R_{gal} is the beam-weighted mean radius of an observation, excluding the galaxy's inner 15".

Columns (5 and 6), R'_{gal} , θ_{gal} are the beam center locations in the plane of the galaxy in arc seconds and degrees from the principal axis ($\theta_{\text{sky}} = -10^\circ$) respectively.

Columns (7 and 8), i_A and i_S are the radial annulus index, and the azimuthal sector index, used for the two averages.

Column (9), $N_D(\text{H}_2)$, molecular hydrogen plus He surface density, given in 10^{20} protons cm^{-2} . $N_D = 6 \times 10^{20} I_{\text{CO}} \cos(i)$.

Column (10) $N_D(\text{HI})$, Neutral hydrogen surface density, given in 10^{20} protons cm^{-2} .

Column (11), total gas number surface density in 10^{20} protons cm^{-2} , with error in N_D from δI_{CO} .

Column (12), Star formation rate in $M_\odot \text{pc}^{-2} \text{Gyr}^{-1}$ from $f_{\text{H}\alpha}$ using the modified Miller-Scalo IMF; $\text{SFR} = C f_{\text{H}\alpha} \cos(i)$. Error term is from $\delta f_{\text{H}\alpha}$.

Column (13), $\text{SFE} (\text{Gyr}^{-1}) = \text{SFR} / \sigma_{\text{gas}}$, where σ_{gas} is total gas mass surface density in $M_\odot \text{pc}^{-2}$ with formal error in SFE from δSFR and $\delta \sigma_{\text{gas}}$.

Column (14), η_{ARM} , is fraction of power of each Gaussian beam which overlaps M51's extrapolated spiral pattern, as derived from the smoothed $\text{H}\alpha$ distribution.

TABLE 2
DERIVED QUANTITIES

in.	R _{sky}	Θ _{sky}	R' _{gal}	R _{gal}	Θ _{gal}	I _A	I _S	N _{H2}	N _{HI}	N _p ± Δ _N	SFR ± Δ _R	SFE ± Δ _E	τ _{arm}
(1)	(2)	(3)	(4)	(5)	(6)	(7)	(8)	(9)	(10)	(11)	(12)	(13)	(14)
1	64	45	66	69	57	6	2	125	10.0	135 ± 15	31 ± 6	0.29 ± 0.07	0.39
2	50	27	52	56	38	5	1	113	11.0	124 14	64 11	0.65 0.13	0.70
3	45	0	45	51	11	4	1	134	11.9	146 15	79 13	0.68 0.13	0.72
4	50	333	51	55	342	5	8	97	11.8	109 12	59 11	0.68 0.15	0.53
5	64	315	65	68	323	6	8	84	12.0	96 10	38 6	0.50 0.09	0.41
6	50	63	53	58	74	5	2	110	9.9	120 14	37 6	0.39 0.08	0.42
7	32	45	33	42	57	3	2	111	10.3	121 14	79 16	0.82 0.19	0.72
8	23	0	23	36	11	2	1	145	10.6	156 19	92 33	0.75 0.27	0.70
9	32	315	33	42	323	3	8	147	10.7	157 21	60 21	0.48 0.18	0.51
10	50	297	52	57	305	5	7	88	11.2	100 13	29 8	0.37 0.10	0.33
11	45	90	48	53	99	4	3	175	9.5	184 23	36 9	0.25 0.06	0.40
12	23	90	24	37	99	2	3	214	9.3	223 30	70 21	0.39 0.12	0.58
13	0	0	0	30	0	1	-	253	9.3	263 38	86 30	0.41 0.15	0.58
14	23	270	24	37	279	2	7	204	9.4	213 29	60 27	0.36 0.16	0.51
15	45	270	48	53	279	4	7	142	9.8	152 23	24 10	0.20 0.09	0.28
16	50	117	52	57	125	5	3	147	9.9	157 19	29 7	0.23 0.06	0.39
17	32	135	33	42	143	3	4	285	9.6	294 37	38 14	0.16 0.06	0.45
18	23	180	23	36	191	2	5	297	9.2	306 36	45 18	0.19 0.08	0.50
19	32	225	33	42	237	3	6	228	8.6	236 39	39 17	0.21 0.09	0.46
20	50	243	53	58	254	5	6	115	8.5	123 20	18 8	0.18 0.08	0.23
21	64	135	65	68	143	6	4	112	10.7	123 13	28 5	0.29 0.06	0.40
22	50	153	51	55	162	5	4	153	10.5	164 18	28 6	0.22 0.05	0.43
23	45	180	45	51	191	4	5	158	9.6	167 19	28 7	0.21 0.06	0.47
24	50	207	52	56	218	5	5	185	8.4	194 22	25 7	0.16 0.05	0.42
25	64	225	66	69	237	6	6	57	8.2	66 7	14 4	0.26 0.08	0.21
26	90	0	90	93	11	7	1	45	11.8	56 6	25 4	0.56 0.10	0.27
27	90	23	92	94	34	7	1	45	9.9	55 5	18 3	0.41 0.08	0.21
28	90	45	94	96	57	7	2	79	10.8	90 12	37 5	0.52 0.09	0.36
29	90	68	96	97	78	7	2	101	11.2	112 13	26 4	0.29 0.05	0.34
30	90	90	96	98	99	7	3	53	11.2	64 8	23 4	0.46 0.10	0.28
31	90	113	94	96	121	7	3	76	11.4	88 10	21 4	0.30 0.07	0.27
32	90	135	92	95	143	7	4	86	10.6	97 13	16 4	0.20 0.05	0.20
33	90	158	90	93	167	7	4	78	9.7	88 11	14 3	0.20 0.05	0.19
34	90	180	90	93	191	7	5	41	8.8	50 6	16 3	0.40 0.09	0.25
35	90	203	92	94	214	7	5	86	9.6	96 13	18 5	0.24 0.07	0.29
36	90	225	94	96	237	7	6	70	10.2	80 11	28 7	0.45 0.13	0.24
37	90	248	96	97	258	7	6	41	9.7	51 6	12 3	0.30 0.07	0.15
38	90	270	96	98	279	7	7	47	11.0	58 7	11 2	0.23 0.05	0.17
39	90	293	94	96	301	7	7	79	12.2	92 9	13 3	0.17 0.04	0.18
40	90	315	92	95	323	7	8	37	12.6	49 6	20 4	0.52 0.12	0.24
41	90	338	90	93	347	7	8	57	12.7	69 7	25 4	0.46 0.08	0.28

TABLE 2 (CONT.)

i	R_{sky}	Θ_{sky}	R'_{gal}	R_{gal}	Θ_{gal}	i_A	i_S	N_{H_2}	N_{HI}	$N_p \pm \sigma_N$	$\text{SFR} \pm \sigma_{\text{R}}$	$\text{SFE} \pm \sigma_{\text{E}}$	η_{arm}
(1)	(2)	(3)	(4)	(5)	(6)	(7)	(8)	(9)	(10)	(11)	(12)	(13)	(14)
42	135	0	135	137	11	8	1	30	11.6	42 ± 5	22 ± 3	0.67 ± 0.11	0.42
43	135	23	138	139	34	8	1	72	11.0	83 9	77 10	1.17 0.19	0.68
44	135	45	141	142	57	8	2	58	15.1	73 9	55 8	0.96 0.16	0.72
45	135	68	143	145	78	8	2	48	14.0	62 6	24 3	0.48 0.08	0.51
46	135	90	143	145	99	8	3	60	12.2	72 9	11 3	0.19 0.05	0.22
47	135	113	141	143	121	8	3	36	11.3	47 6	7 2	0.19 0.05	0.18
48	135	135	138	140	143	8	4	17	10.6	28 3	25 4	1.12 0.23	0.34
49	135	158	135	137	167	8	4	32	9.2	41 4	10 3	0.29 0.10	0.19
50	135	180	135	137	191	8	5	38	8.5	47 6	11 3	0.30 0.08	0.29
51	135	203	138	139	214	8	5	62	12.4	74 8	20 5	0.34 0.10	0.36
52	135	225	141	142	237	8	6	62	12.5	74 9	48 15	0.81 0.26	0.37
53	135	248	143	145	258	8	6	30	10.7	41 5	7 2	0.22 0.07	0.09
54	135	270	143	145	279	8	7	30	11.4	42 5	3 1	0.08 0.02	0.05
55	135	293	141	143	301	8	7	58	12.4	70 8	2 1	0.03 0.01	0.05
56	135	315	138	140	323	8	8	39	14.5	53 6	6 2	0.13 0.04	0.10
57	135	338	135	137	347	8	8	27	14.1	41 4	20 4	0.63 0.12	0.34
A	248	23	252	253	34	-	-	27	7	34 4	2 -	0.09 0.01	0.12
B	225	23	229	230	34	-	-	22	3	30 3	2 -	0.07 0.01	0.06
C	154	21	156	158	32	-	-	27	8	35 4	61 17	2.19 0.66	0.59

as in the figures that follow. We use σ_p to indicate the total gas surface density in $M_\odot \text{pc}^{-2}$.

c) H-alpha Fluxes and Star Formation Rates

The primary data used here for comparison with the CO and HI data are H α observations kindly supplied by Dr. Rob Kennicutt and referred to in the atlas of 125 galaxies of Hodge and Kennicutt (1983). These observations were made with a Carnegie image tube at the 2.1 m telescope of Kitt Peak National Observatory (KPNO). The plates were taken with a 20Å bandwidth λ 6563 H α filter which excluded the λ 6548, and 6584 [NII] lines outside of $R=15''$. The galaxy was also observed with a 20Å wide filter offset 40 Å to the blue. The plates were digitized with the KPNO Photometric Data System (PDS) microdensitometer at a resolution of 1.5" and differenced to yield a continuum subtracted image. This image, henceforth the "PDS image", smoothed to 8" resolution and clipped to an appropriate window, is shown in Figure 1.

In order to ascertain the error associated with the observed flux of this image, as well as errors that may arise from averaging low level flux from this image over large apertures, we compared the PDS image with a more sensitive, though smaller field, CCD H α image of M51 kindly provided by Dr. Holland Ford (personal communication, 1985). After independently calibrating this image using standard stars and subtracting the red continuum flux, we found that the PDS and CCD images agreed very well in position, extent and absolute intensity of

the observed HII regions (out to $R = 110''$, which is the full extent of the CCD image field). By comparing each $45''$ aperture within the two images, we were able to determine an absolute calibration error of 7% and to rule out the possible exclusion of a significant amount of low level emission in the averaging process. It was found that the total observed flux in each aperture was dominated by the emissive regions having a brightness greater than $2.0 \times 10^{-16} \text{ erg cm}^{-2} \text{ s}^{-1} \text{ arcsec}^{-2}$, with the CCD image sensitivity extending well below this value.

No attempt was made to calibrate either the PDS or the CCD image in the nuclear region ($R < 15''$), where the strength of the [NII] line at $\lambda 6584 \text{ \AA}$ exceeds the $H\alpha$ line in intensity up to a factor of six (Ford et al. 1985). The nuclear region of this galaxy has been shown to be an active and perturbed region (Ford et al. 1985; Goad and Gallagher 1985) undergoing evolution dissimilar to that of the disk. Both molecular (CO) and atomic (HI) gas have been reported to be absent in the inner $15''$, (Rydbeck, Hjalmarsen and Rydbeck 1985, henceforth RHR; and Wellichew and Gottesman 1973, respectively), although these assertions may have to be somewhat relaxed in light of the central emission found in higher resolution CO and HI studies (Y. Sofue, personal communication; A. Rots, personal communication, respectively). Due to the unusually active nucleus, we have omitted the $H\alpha$ flux of this region from our analysis. We have masked out the inner $15''$ of the $H\alpha$ image and have compared the CO and HI emission in the central $45''$ with the average $H\alpha$ flux from the beam weighted annulus extending from

$R = 15''$ outward. For this reason, in the figures which follow, the central region is shown with a dashed line, and the $H\alpha$ brightness therein is a lower limit.

The most important source of error in the $H\alpha$ measurements arises in correcting for the effects of extinction in the disk of M51 along the line of sight to the HII region under observation. In the central region, for example, extinction estimates may yield corrected $H\alpha$ fluxes up to four times the observed value, with correspondingly large uncertainties. To obtain correction factors, we have employed the recent extinction measurements of van der Hulst and Kennicutt (1986, henceforth vK), which are based upon observations of the brightest 40 HII regions in M51 as seen in the PDS image and dual-frequency radio continuum observations. In the region $R=15''-60''$, where the vK sampling is sparse, we have augmented their data with Balmer decrement extinctions from Jensen, Strom and Strom (1976). From these combined data, we have constructed a radial extinction function and have applied it to the high resolution PDS image before computing average $H\alpha$ brightnesses over the $45''$ beam areas. Thus, our extinction measurements applied to individual beam locations maintain large uncertainties, with more reliable emission estimates resulting when azimuthal means are taken. In Appendix A we discuss our extinction correction method in detail, with the salient points listed below:

- The vK study found the extinction to be "patchy" in the sense that neighboring HII regions often showed a magnitude or more difference in

visual extinction, but that a fairly well defined mean value ($A_V=1.8\pm 0.4$) was maintained throughout the disk at radii $R=60'' - 180''$.

- The νK study found a slight falloff in $\langle A_V \rangle$ with radius (where brackets denote an azimuthal mean) which agrees well with the analogous extinction gradient found for M51 in the multi-frequency radio continuum study of Klein et al. (1984).

- The far-IR measurements of Smith (1982), of resolution $49''$, indicate that the dust opacity in M51's disk is not clumpy on the scale of our beam, nor is it systematically biased to the spiral pattern, but rather maintains a uniform distribution.

- Outside of $R=60''$, the mean extinctions obtained by comparing the radio continuum and $H\alpha$ data agree, within the errors, to the empirical measure $A_V = 2.7 \times 10^{-22} N_p (HI+H_2)$, suggested by Bohlin, Savage, and Drake (1978), where the leading constant in their relation has been halved to reflect the dust contribution, on the average, from half of the disk.

To compute the uncertainty for the corrected mean $H\alpha$ brightness in each beam, we have used the uncertainty in extinction for each HII region, $\sigma_{A_V} \approx 1.1$ mag. as found by νK , the total number of HII regions in each beam, and the total uncorrected flux (Equation A.9). The resulting uncertainties, which exceed 30% at many locations, are indicated by error bars in the figures which follow.

Corrected $H\alpha$ fluxes have been used to compute the star formation rate at each beam position by the method outlined in Kennicutt (1983). By calculating the total Lyman ionizing flux of radiation-bounded HII regions directly from the Balmer α line emission, and assuming a number distribution in mass (i.e. an initial mass function, IMF) for the newly formed O and B stars, their ionizing luminosity with mass, and their lifetimes, the $H\alpha$ brightness at each beam position may be converted to a massive star formation rate (MSFR). A drawback to the method, as discussed in §A.d is that it will tend to underestimate the total number of Lyman continuum photons from density bounded HII regions and from HII regions where dust absorbs a significant fraction of the UV continuum flux.

Obtaining the total SFR from this rate then depends critically on the selected IMF. We have taken note that the relative values of the global $H\alpha$ equivalent width (EW) and the (B-V) color index can serve as a sensitive discriminator between various IMFs (Kennicutt 1983). In particular, the measurements for M51's disk of $EW(H\alpha+[NII]) = 24 \text{ \AA}$, $(B-V)_0^T = 0.6$ (de Vaucouleurs, de Vaucouleurs, and Corwin 1976), and $\langle A_V \rangle \approx 1.8$ (vK and this study) are not consistent with a Miller-Scalo IMF, but are consistent with an "extended Miller-Scalo" IMF, which has a fall-off in the high mass end ($IMF \sim M^{-2.5}$) similar to the Salpeter (1955) function. We hasten to add that Kennicutt used his IMF discrimination method in a statistical treatment of large numbers of galaxies, and not for the characterization of individual disks. One

difficulty in applying the method to an individual galaxy is in knowing the mean extinction, a difficulty which the recent studies (vK; Klein et al.) have helped surmount.

Using the extended Miller-Scalo IMF we have estimated the total SFR at each beam position by extrapolating the MSFR to the low mass end of the function. The method and the derivation of the conversion factors, C_{SFR} , between $\text{H}\alpha$ brightness, MSFR and SFR are discussed further in Appendix A.d. In summary, we adopt conversions from $\text{H}\alpha$ brightness $f_{\text{H}\alpha}$ ($\text{erg cm}^{-2} \text{ s}^{-1} \text{ arcsec}^{-2}$), and total luminosity $L_{\text{H}\alpha}$ (erg s^{-1}) to star formation rates as follows:

for massive stars, $M > 10 M_{\odot}$

$$\text{MSFR} [M_{\odot} \text{ pc}^{-2} \text{ Gyr}^{-1}] = 4.71 \times 10^{15} f_{\text{H}\alpha} \cos(i), \quad (\text{II.3})$$

$$\int \text{MSFR} \text{ dA} [M_{\odot} \text{ yr}^{-1}] = 9.19 \times 10^{-43} L_{\text{H}\alpha}, \quad (\text{II.4})$$

and for all masses;

$$\text{SFR} [M_{\odot} \text{ pc}^{-2} \text{ Gyr}^{-1}] = 4.54 \times 10^{16} f_{\text{H}\alpha} \cos(i) = 9.63 \text{ MSFR} \quad (\text{II.5})$$

$$\int \text{SFR} \text{ dA} [M_{\odot} \text{ yr}^{-1}] = 8.92 \times 10^{-42} L_{\text{H}\alpha} = 9.63 \int \text{MSFR} \text{ dA}, \quad (\text{II.6})$$

where the galaxy's inclination i becomes important for the brightness measurements but is implicitly included in spatial integrations over a region of area A (in pc^2). It can be seen from these formulae that the extended Miller-Scalo IMF puts about 10% by mass of new stellar material into stars more massive than $10 M_{\odot}$. The way in which these

conversion factors would change for different IMFs and for a range of upper and lower mass cutoffs for each IMF are also given in Appendix A.

A distinction has been drawn in this study between absolute and relative errors. For example, the gas density conversion factor possesses a sizable uncertainty (50%) as reported by various authors. Yet, if our Galaxy may be used as a guide, the relation between L_{CO} and virial mass is seen to maintain a constant proportionality over an order of magnitude in cloud luminosity (c.f. Scoville et al. 1987, Fig. 8) independent of disk position. Thus, the use of a constant b value leads to small relative errors from location to location, especially when regions as large as 2.1 kpc are considered. The derived $H\alpha$ fluxes have an appreciable relative uncertainty due to variable extinction effects as discussed above. The conversion of these values to MSFRs and total SFRs includes absolute errors to the extent that the IMF slope we have chosen is in error, and includes relative errors in so far as the IMF changes with disk position. These latter relative errors are not known, and may be important. We have given some evidence in Appendix A for M51's IMF being both known and constant, although the evidence is far from conclusive. In summary, the error bars for all figures have been computed from the relative uncertainties in molecular mass (due to I_{CO} calibration) and $f_{H\alpha}$ (due to extinction). The range of absolute uncertainty pertaining to the H_2 mass and SFR conversions, as discussed in §A.e, most likely tend

toward overestimations of H_2 masses and underestimations of star formation rates and efficiencies.

CHAPTER III

ANALYSIS AND RESULTS

a) Point by Point Comparisons

In Figure 2a we compare the H α and CO distributions, plotted as a function of radius in the plane of the galaxy. Both the CO and H α intensities exhibit a wide scatter at each radius and the same general falloff in the inner disk. The three high values in H α emission at $R = 6.5$ kpc correspond to positions encompassing 3 of the bright HII complexes (Nos. 5, 6, 8, 10), (Nos. 14, 19, 24, 27), and (Nos. 71, 72) studied by Carranza, Crillon and Monnet (1969). These high values are extreme examples of the generally larger scatter seen in the H α distribution as compared with the CO distribution, at each radius.

In Figure 2b the CO emission has been converted to an H $_2$ surface density and plotted against the HI surface density on a logarithmic scale. The neutral hydrogen follows what is becoming a familiar pattern in "late type" spirals (c.f. Morris and Rickard 1982; Young and Scoville 1982; Tacconi and Young 1986) where the inner disk HI surface density appears as fairly flat distribution exhibiting a central depression, and displays a surface density which is typically a small fraction of the inner disk molecular surface density. Within a radius $R_{gal} = 6.5$ kpc we can see that the molecular component of the ISM in M51 dominates the total gas surface density.

Mean values at each radius and the rms deviations are given in Table 3a. Here σ represents the error associated in measuring the mean

Figure 2. a) The I_{CO} and $f_{\text{H}\alpha}$ brightness distributions as a function of radius in the plane of the galaxy. The resolution is 2.1 kpc as indicated by the bar, and the radius positions are the mean radii within each aperture. b) The molecular ($\text{H}_2 + \text{He}$) and HI surface densities as a function of radius. The molecular distribution approximates a R^{-1} distribution and accounts for 94% of the gaseous disk mass and 12% of the total disk mass within $R=6.6$ kpc. HI spectra of 40" resolution were provided by A. Rots (1985).

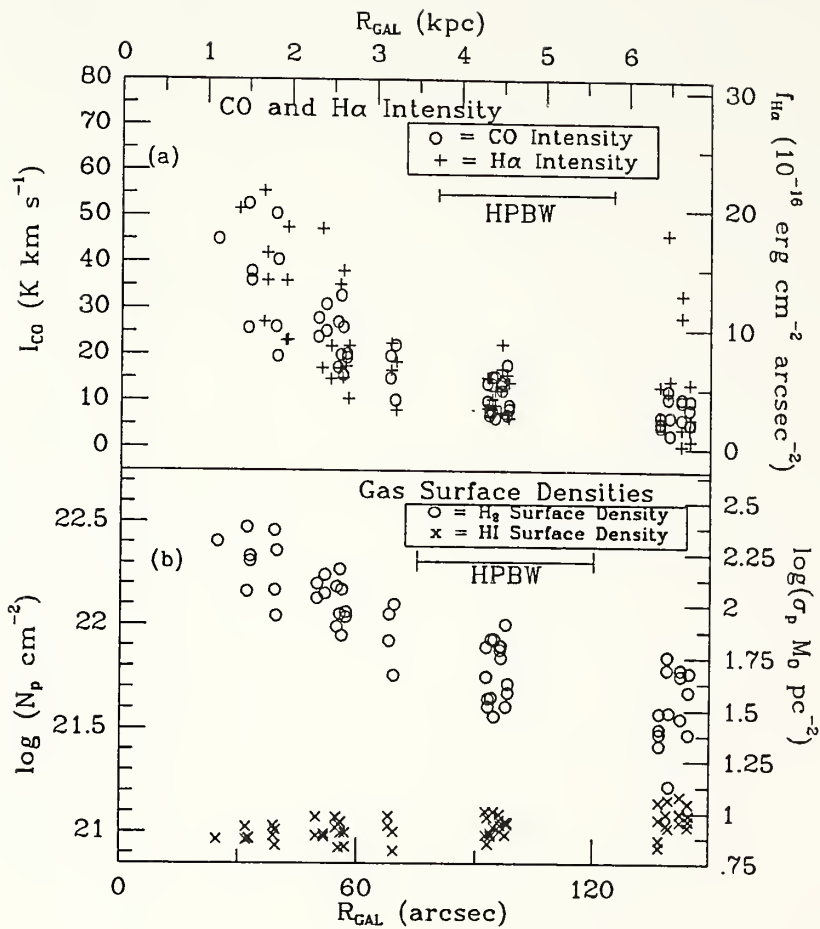


TABLE 3a AND 3b (NOTES)

These azimuth and sector mean values were obtained from the individual data of Tables 1 and 2. All quantities were spatially averaged in the frame of the galaxy with the mean sector values produced through an interpolation and averaging scheme described in §IIIb. The sectors are wedges with a 45° opening angle and extending from $R_{gal}=20''$ to $R_{gal}=160''$.

Row (1) i_A is the annulus index, i_S is the sector index.

Row (2) N is the number of observations used to compute the mean.

Row (3) $\langle R_{gal} \rangle$ is the mean radius of an annulus in the plane of the galaxy, $\langle \theta_{gal} \rangle$ is the mean position angle of a sector, measured east of the principle axis $\theta_{sky} = -10^\circ$.

Row (4) $\langle I_{CO} \rangle$ is the mean CO integrated intensity.

Row (5) δI_{CO} is the dispersion of the I_{CO} values about the mean.

Row (6) $\sigma_{I_{CO}}$ is the uncertainty of $\langle I_{CO} \rangle$ determined from the σ_I values of Table 1.

Row (7) $\langle f_{H\alpha} \rangle$ is the mean brightness over the region.

Row (8) $\delta f_{H\alpha}$ is the dispersion of the $f_{H\alpha}$ values about the mean.

Row (9) $\sigma_{f_{H\alpha}}$ is the uncertainty of $\langle f_{H\alpha} \rangle$ determined from the σ_f values of Table 1.

Row (9a) $\langle L_B \rangle$ is the normalized blue luminosity with 100 units equal to a blue magnitude of $16.96 \text{ mag arcsec}^{-2}$, from Boroson, (1981)

Row (10) $\langle HI \rangle$ is the average HI surface density in each region.

Row (11) $\langle N_p \rangle$ is the average gas (molecular and atomic) surface density in each region. The uncertainty is given by $\sigma_{N_p} = 6.0 \times 10^{20} \cos(20) \sigma_{I_{CO}}$.

Row (12) $\langle SFR \rangle$ is the average star formation rate over the region. The uncertainty σ_{SFR} is obtained from $\sigma_{SFR} = 4.52 \times 10^{16} \cos(20) \sigma_{f_{H\alpha}}$

Row (13) $\langle SFE \rangle = \langle SFR \rangle / \langle \sigma_p \rangle$ where $\langle \sigma_p \rangle [M_\odot \text{ pc}^{-2}] = 0.798 \times 10^{-20} \langle N_p \rangle$.

Row (14) δSFE is the dispersion of the SFE values about the mean.

Row (15) σ_{SFE} is the uncertainty of $\langle SFE \rangle$ determined from the σ_E values of Table 2.

TABLE 3a
AZIMUTHAL MEAN VALUES

(1) i_A	1	2	3	4	5	6	7	8
(2) N	1	4	4	4	8	4	16	16
(3) $\langle \theta_{gal} \rangle$ (arc seconds)	30	36	42	52	56	69	95	141
(4) $\langle v_{CO} \rangle$ (K km s ⁻¹)	45	38	34	27	22	17	11	8
(5) δv_{CO} (K km s ⁻¹)	-	10	12	3	5	5	4	3
(6) $\sigma_{v_{CO}}$ (K km s ⁻¹)	4.7	2.0	1.9	1.4	0.9	1.0	0.3	0.2
(7) $\langle f_{H\alpha} \rangle$ 10 ⁻¹⁶ erg/(cm ² s arcsec ²)	20.0	15.6	12.6	9.8	8.4	6.4	4.7	5.0
(8) $\delta f_{H\alpha}$ 10 ⁻¹⁶ erg/(cm ² s arcsec ²)	-	4.0	3.9	5.0	3.6	2.0	1.6	4.8
(9) $\sigma_{f_{H\alpha}}$ 10 ⁻¹⁶ erg/(cm ² s arcsec ²)	7.1	2.9	2.0	1.2	0.7	0.6	0.2	0.3
(9a) $\langle L_B \rangle$ (normalized luminosity)	99	72	54	34	29	22	19	13
(10) $\langle HI \rangle$ (10 ²⁰ protons cm ⁻²)	9	10	10	10	10	10	11	12
(11) $\langle n_p \rangle$ (10 ²⁰ protons cm ⁻²)	263	225	202	162	136	106	75	56
(12) $\langle SFR \rangle$ (M _⊙ pc ⁻² Gyr ⁻¹)	86	67	54	42	36	28	20	22
(13) $\langle SFE \rangle$ (Gyr ⁻¹)	0.41	0.42	0.42	0.33	0.36	0.33	0.36	0.48
(14) δSFE (Gyr ⁻¹)	-	0.20	0.26	0.20	0.19	0.09	0.13	0.36
(15) σSFE (Gyr ⁻¹)	0.15	0.09	0.07	0.05	0.03	0.04	0.02	0.03

TABLE 3b
SECTOR MEAN VALUES

(1) i_S	1	2	3	4	5	6	7	8
(2) N	7	7	7	7	7	7	7	7
(3) $\langle \theta_{gal} \rangle$ (°)	23	67	113	158	203	248	293	338
(4) $\langle v_{CO} \rangle$ (K km s ⁻¹)	12	14	14	14	15	12	13	10
(5) δv_{CO} (K km s ⁻¹)	6	5	9	12	12	9	8	6
(6) $\sigma_{v_{CO}}$ (K km s ⁻¹)	0.5	0.6	0.6	0.6	0.7	0.5	0.6	0.4
(7) $\langle f_{H\alpha} \rangle$ 10 ⁻¹⁶ erg/(cm ² s arcsec ²)	10.8	9.0	4.8	4.5	4.5	5.4	3.0	5.9
(8) $\delta f_{H\alpha}$ 10 ⁻¹⁶ erg/(cm ² s arcsec ²)	6.5	3.7	3.4	2.0	1.8	3.6	3.3	3.9
(9) $\sigma_{f_{H\alpha}}$ 10 ⁻¹⁶ erg/(cm ² s arcsec ²)	0.8	0.6	0.5	0.4	0.5	0.8	0.4	0.5
(10) $\langle HI \rangle$ (10 ²⁰ protons cm ⁻²)	11	12	11	10	10	10	12	12
(11) $\langle n_p \rangle$ (10 ²⁰ protons cm ⁻²)	76	93	92	88	96	79	83	68
(12) $\langle SFR \rangle$ (M _⊙ pc ⁻² Gyr ⁻¹)	46	38	21	19	19	23	13	25
(13) $\langle SFE \rangle$ (Gyr ⁻¹)	0.73	0.55	0.27	0.43	0.29	0.39	0.16	0.47
(14) δSFE (Gyr ⁻¹)	0.27	0.25	0.10	0.36	0.07	0.23	0.11	0.18
(15) σSFE (Gyr ⁻¹)	0.06	0.04	0.03	0.06	0.04	0.06	0.02	0.04

values, and δ represents the rms scatter of the individual points. The scatter in each of the two gas distributions is quantitatively different. At the 2.1 kpc resolution used in this study, the HI shows only 25% variations from point to point while the H₂ distribution shows 40% variations. It is possible to crudely measure the number of molecular clouds to which the magnitude of these variations would correspond. Using a "standard cloud" (a statistically contrived entity) of diameter 34 pc and mass $2.9 \times 10^5 M_{\odot}$, obtained from the mean values of the survey results of Sanders, Scoville and Solomon (1985), the observed 40% variations in the I_{CO} measurements would correspond, for example, to 240 ± 100 clouds in a beam, if in that beam $I_{CO} = 4 K [T_R]$ km s⁻¹. While the HI distribution appears smoother than the H₂ distribution, it may well be that the HI distribution is clumpy but on a significantly smaller absolute scale, as noticed in more nearby galaxies (Mihalas and Binney 1981, p. 539), and that HI spiral structure is present, but unresolved in these observations.

The CO emission falloff in the inner positions of Figure 2b shows a steeper gradient than do the outer positions, even after smoothing by the 45" Gaussian beam, indicating that the entire distribution can not be well modeled by single exponential function. A 1/R functional dependence provides a better description, having a χ^2 which is 25% lower than the best fit exponential curve (of scale length 2.6 kpc) and five times lower than the best fit Gaussian curve. Our few CO observations of the North and South arm in the outer disk (not shown

here) indicate that the molecular emission falls rapidly outside of $R_{gal} = 220''$ (except toward the tidal arm, as discussed in §Vb). We therefore have a situation similar to that encountered in NGC 6946 (Tacconi and Young 1986), where $N_p(H_2)$ drops off to equal $N_p(HI)$, at a value of about $N_p = 10^{21} \text{ cm}^{-2}$ between $R_{gal} = 10-12 \text{ kpc}$, a region where the blue magnitude for each galaxy is nearly equal as well: $m_B = 23.6 \pm 0.2 \text{ mag arcsec}^{-2}$ (Boroson 1981; Ables 1971).

The atomic and molecular gas surface densities at each point were added to produce detailed map of the total gas density, σ_p . In Figure 3a we display σ_p against $f_{H\alpha}$ at each position in a log-log plot. One may see a rough correlation between the two distributions. Linear correlation coefficients and the probabilities of uncorrelated populations are given in Table 4a for the different radius regimes. Approximately the same correlation is maintained throughout the disk. The scatter apparent in the figure is a product of the scatter in each distribution with radius and the occurrence of many emissive HII regions found on the spiral arms which are unaccompanied by a corresponding enhancement of molecular emission. The detection of the spiral pattern is discussed fully in §IIIc.

b) Azimuthal and Radial Averages

The $H\alpha$ and gas density data have been binned according to radius into 8 groups. The mean values at each radius were plotted against each other in Figure 3b, and are listed in Table 3a. The correlation

Figure 3a. The $f_{\text{H}\alpha}$ brightness vs. the total gas surface density (10^{20} protons cm^{-2}) at 57 positions. Correlation coefficients are given in Table 4a, with a linear fit yielding $\text{SFE} = \text{SFR}/\sigma_{\text{gas}} = 0.54 \text{ Gyr}^{-1}$, with the SFR computed as described in §III.

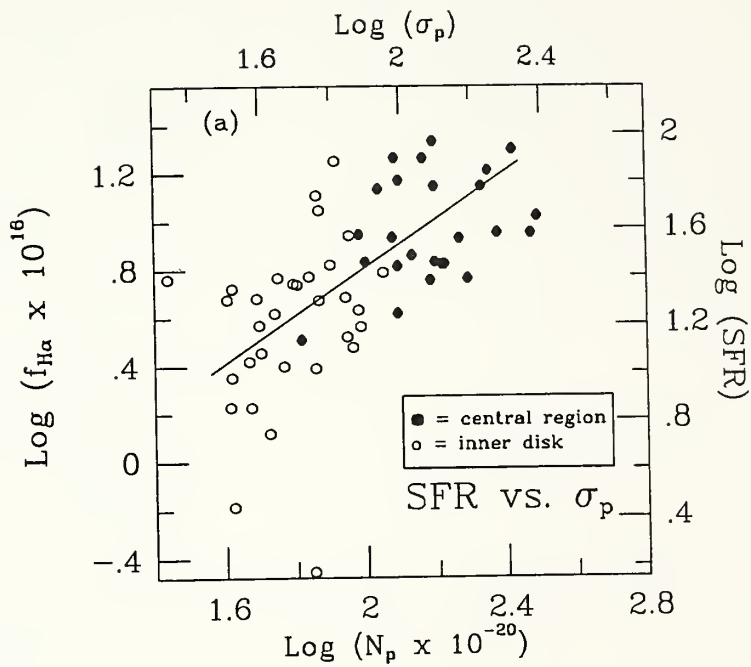


TABLE 4a

LINEAR CORRELATIONS BETWEEN H α FLUX AND GAS SURFACE DENSITY

Rmin (1)	Rmax (2)	N (3)	SAMPLE (4)	b (5)	Pr(b,N) (6)	m (7)	C (8)
0"	- 70"	25	HI+H ₂	0.23	0.27	-	-
70"	- 150"	32	HI+H ₂	0.32	<0.01	-	-
0"	- 150"	57	H ₂	0.55	<0.01	0.4 \pm 0.1	-7 \pm 1
0"	- 150"	57	HI+H ₂	0.54	<0.01	0.4 \pm 0.1	-12 \pm 1

TABLE 4a (NOTES)

Column (1 and 2) Rmin and Rmax define the radius regime in arc seconds in the plane of the galaxy from which the data sample was taken.

Column (3) n is the number of data points used in determining b and Pr(b,n).

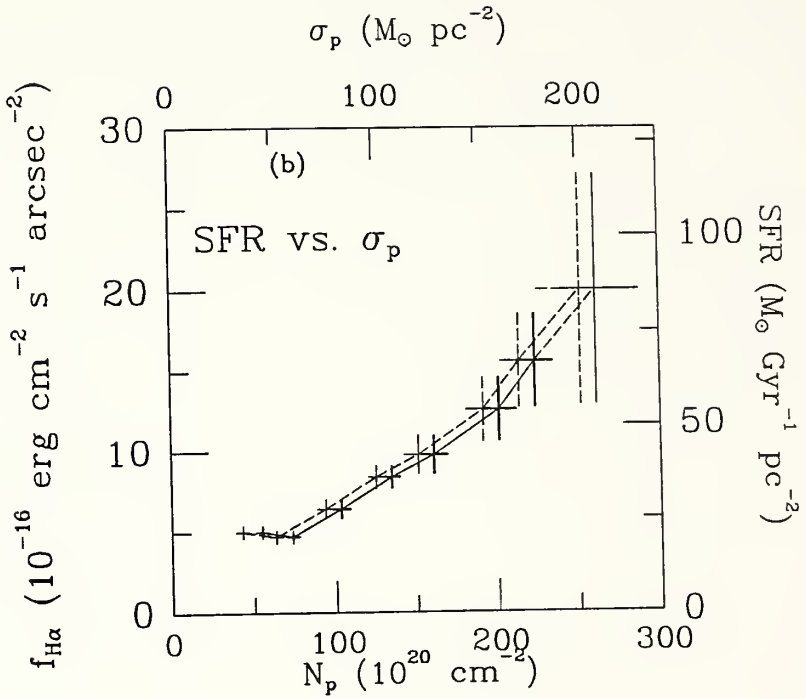
Column (4) Displays the gas density parameter used for comparison with the $f_{H\alpha}$.

Column (5) b is the formal correlation coefficient between the gas densities and H α fluxes.

Column (6) Pr(b,N) is the probability of a correlation coefficient as high as b originating from two uncorrelated populations.

Column (7 and 8) The constants m and C are the best fit to the equation: $f_{H\alpha} \times 10^{16} = m (N_p \times 10^{-20}) + C$, displayed in Figure 3. A slope of 0.4 ($f_{H\alpha}/N_p$) corresponds to a star formation efficiency of 0.5 Gyr⁻¹.

Figure 3b. The azimuthally averaged $f_{H\alpha}$ brightness plotted against N_D (10^{20} protons cm^{-2}) for eight radial bins. Dashed lines represent N_D computed without the contribution of HI. The outer annulus (leftmost data point) displays a departure (increased $f_{H\alpha}/I_{C0}$) from the trend seen at interior radii.



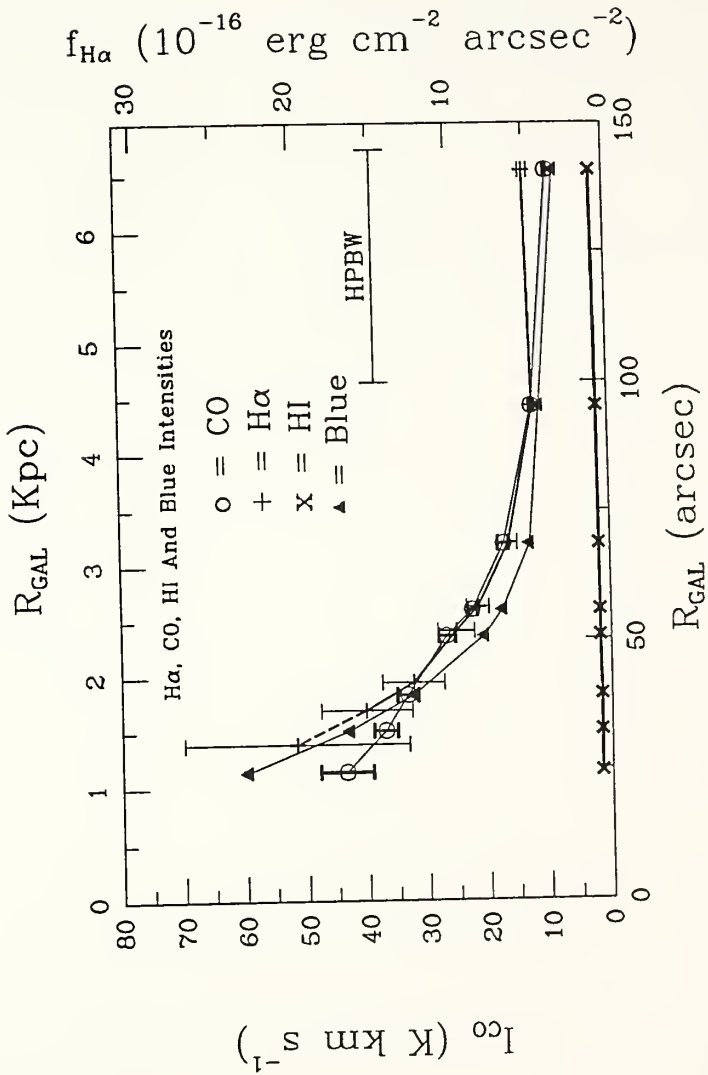
between the $H\alpha$ emission and gas density is apparent in this figure. The leftmost data point alone shows a departure from the linear trend and indicates a higher $H\alpha$ to CO ratio in the region $R=125''-145''$. In this region, the molecular surface density maintains a relatively shallow falloff whereas there exist extended HII complexes which are among the most emissive of any found in the galaxy. These HII regions are also apparent in Figure 1.

Figure 4 illustrates the azimuthal average of the $H\alpha$ emission and gas surface densities versus radius. Also shown in Figure 4 is the blue luminosity radial function smoothed to equal resolution, from Boroson (1981). The average intensities of the CO and blue luminosities fall off with radius in remarkable accord, as shown for several luminous late type galaxies (Young and Scoville 1982). The linear proportionality between the $H\alpha$ and CO emission between 1 and 7 kpc is seen here to be even more pronounced than shown in SY, due to the improved data sets. This result implies a linear proportionality between SFR and the total ($H\text{I}+\text{H}_2$) gas surface density N_p when the total content of an annulus is considered. As we have shown in Figure 3a, this linear relation is not strictly maintained in the case of individual disk locations. The error bars in Figure 3b represent measurement uncertainty and not the dispersion of the points comprising the average, and the $H\alpha$ intensity at the central position has a large uncertainty for the reasons discussed in §IIb.

The high correlation evident in the azimuthally averaged $H\alpha$ and σ_p distributions might suggest the possibility that spatial averaging

Figure 4.

The azimuthally averaged CO, H α , HI, and Blue light distributions in the disk of M51 (see text for references). All data are smoothed to 45" resolution and plotted against mean radius in the plane of the galaxy. The HI distribution is plotted correctly relative to the CO such that multiplying the left y-axis values by 6×10^{20} gives the gas surface density in protons cm^{-2} for both the molecular and atomic species.



over any large area of this galaxy yields a high correlation in the $H\alpha$ and α_p values. In order to test this hypothesis, averages over a different set of comparably large areas is shown in Figures 5a and 5b. Eight equal pie-shaped wedges (sectors) with 45° opening angles extending from $R_{gal}=20''$ to $R_{gal}=160''$ in the plane of the galaxy were considered, and care was taken to average the emission within each wedge so as to treat the observations in an unbiased fashion. Within each $2''$ by $2''$ pixel the intensity values from the nearest beam centers were weighted by the magnitude of the Gaussian point spread functions, thus weighting the overlapping interior beams and the areal growth of the wedges correctly. Figure 5a shows that the average CO intensity in each of the eight sectors of M51 is nearly equal, whereas the $H\alpha$ intensities vary by a factor of 4, with excesses evident in the Northeast and Southwest. There is no apparent correlation in the averaged $H\alpha$ and CO values as seen in Figure 5b. Mean intensities for the sector averaging scheme are given in Table 3b.

From these studies we conclude that the average H-alpha emission at a given radius is well determined and follows the average gas distribution, but in a given sector of the galaxy the $H\alpha$ flux is not a constant. The molecular distribution, on the other hand, maintains an equal distribution over all eight sectors. In fact, the mean CO intensity in each sector is at least as well determined as at each radius.

Figure 5a.

The average H α and CO emission within 8 sectors of M51's disk. Each sector extends 45° in azimuth in the plane of the galaxy with $\theta_{gal} = 0$ on the principle axis, and in radius from $R_{gal} = 20''$ to 160''. The bright Northeast HII regions appear in the first two sectors causing elevated H α brightnesses. The molecular gas is globally more evenly distributed than the ionized gas.

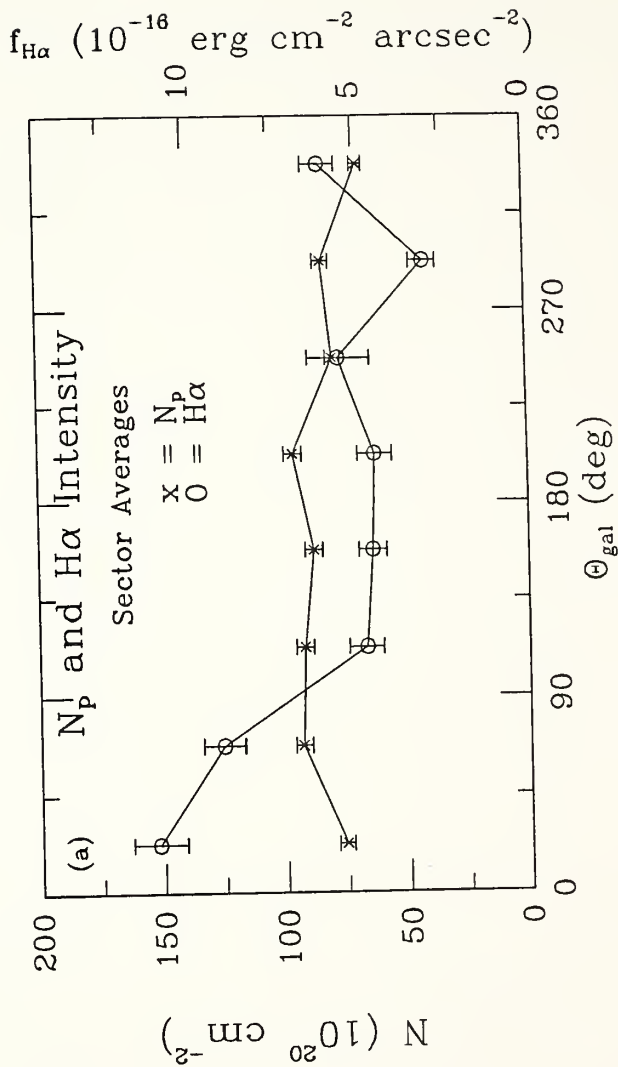
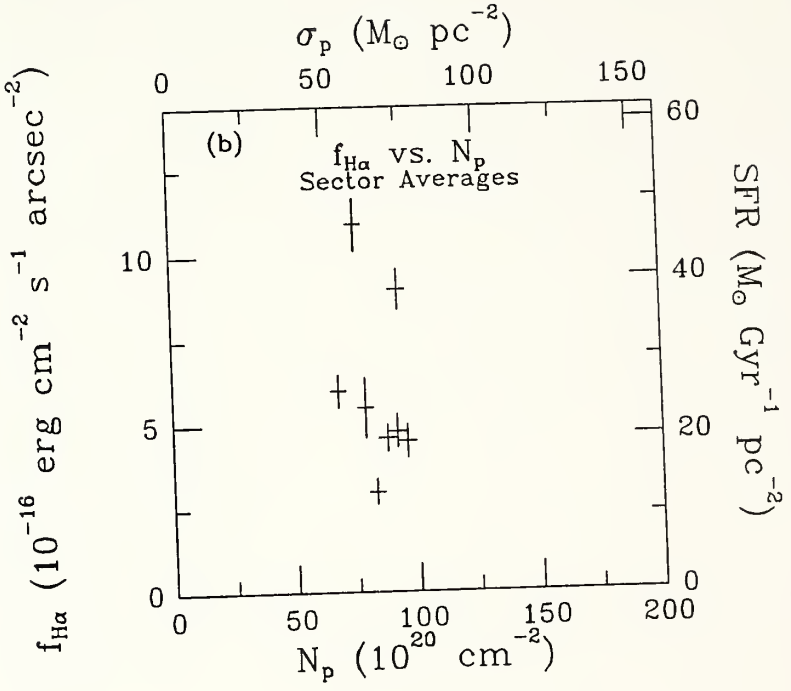


Figure 5b. The correlation of gas surface density with star formation rates in eight sectors. No correlation is seen, indicating that additional, azimuthally dependent factors, such as the action of the spiral density wave and tidal forces, must go into determining $SFR(\sigma_p)$.



c) The Spiral Pattern

Two tests were conducted to delineate the role played by the spiral density wave in the star formation process. These tests are denoted as the degree of arm coupling, and the spiral phase distribution, and we discuss each in turn below.

(i) The Degree of Arm Coupling

In the first test, a determination was made of the extent to which star formation rates and efficiencies vary within the spiral arms and the interarms. Obstacles to producing these measurements include: 1) the lack of a rigorous definition of a spiral arm, and 2) our resolution being such that the total area of any aperture falls simultaneously on regions that might be characterized as arm and interarm regions. Thus, with fractional sensitivity to spiral arms, the observed emission strength in any aperture must be interpreted in terms of the fraction of that aperture which falls on the spiral pattern. By defining the spiral pattern as a smoothed and thresholded version of the $H\alpha$ map of Figure 1, with regions assigned either zero or unit intensity on the basis of the local $H\alpha$ brightness, we have produced a narrow but nearly continuous two-armed structure serving as a silhouette of the spiral pattern. The coupling parameter, τ_{arm} , listed in Table 2, is the fractional power of a Gaussian beam illuminating this pattern, and ranges between 0.2 and 0.7. For each position we have also computed the relative excesses in the parameters

N_p , $f_{H\alpha}$, and SFE, defined as the fractional deviation from the mean value at that radius, e.g. excess gas surface density $N_{ex} = (N_p - \langle N_p \rangle) / \langle N_p \rangle$, using the mean values of Table 3a.

In light of our adopted definition of the spiral pattern, it is not surprising to find that the $H\alpha$ fractional excess of each beam is well correlated with the arm coupling parameter, as can be seen in Figure 6a. The vertical scatter in this figure is indicative of the variability of the number density and total luminosities of spiral arm HII regions. The excesses exhibited by the other distributions -- CO, HI, and SFE -- each acquired at the same resolution, are correlated against the arm coupling parameter with the results given in Table 4b, and shown plotted in Figures 6b-d. The results have yielded the following conclusions.

- 1) The $H\alpha$ emission excesses show a strong correlation with the spiral pattern, while the CO excesses generally do not. If the molecular clouds are confined to a broad (width $> 45''$) spiral pattern, then this result could be a resolution effect.
- 2) The CO emission varies less than 60% from its mean value both on the arms and on the interarms, variations which, in general, are not correlated with radius or the spiral pattern at $45''$ resolution.
- 3) The $H\alpha$ emission varies less than the CO emission on the interarms, with a scatter of 30%. The scatter becomes much more than this on the arms, with differences from the mean of up to 100%.

Figure 6a-d. The fractional excess in I_{CO} , $H\alpha$, $H I$ and star formation efficiency shown against η_{arm} , the fraction of the beam overlapping the spiral pattern. The scatter in CO emission intensity is generally not correlated with η_{arm} , although seven positions (filled circles), located near the brightest $H II$ regions in the spiral pattern, do stand out in excess CO emission. The star formation efficiency is correlated with the pattern.

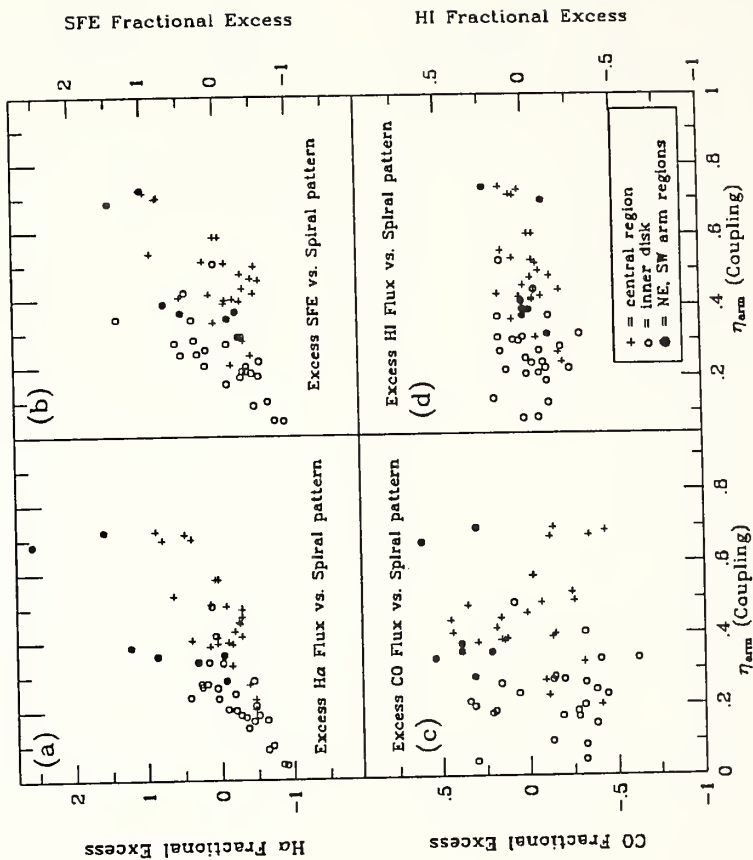


TABLE 4b

LINEAR CORRELATIONS OF THE SPIRAL PATTERN WITH EMISSION EXCESSES

Parameter (1)	N (2)	b (3)	Pr(b,N) (4)
SFR _{ex}	32	0.87	<0.01
SFE _{ex}	32	0.76	<0.01
N(H ₂) _{ex}	32	0.37	0.37
N(HI) _{ex}	32	0.24	0.24

TABLE 4b (NOTES)

Column (1) The parameters are the fractional deviations from the mean values, defined in §IIIc. For example $SFR_{ex}(R) = (SFR(R) - \langle SFR(R) \rangle) / SFR(R)$. These parameters are correlated against the parameter η_{arm} as discussed in the text and displayed in Figure 7a.

Column (2) N is the number of points used in the correlation. All points outside of $R_{gal} = 70''$ were used because outside of the radius the spiral pattern is sufficiently resolved by a $45''$ aperture to detect correlations.

Column (3) b is the linear correlation coefficient between the parameter and η_{arm} .

Column (4) Pr(b,n) is the probability of a correlation coefficient as high as b originating from two uncorrelated populations.

4) The HI emission, at 45" resolution for $R < 160''$ shows little correlation with the spiral pattern, and maintains a small ($\approx 25\%$) variation on the arms and interarms.

5) As a consequence of points 1 and 2 above, the SFE excesses are correlated with the spiral pattern and are correlated in the same way as are the $H\alpha$ emission excesses, as can be seen by comparing Figures 6a and 6b.

6) Seven positions lying along the bright HII complexes prominent in the Northeast and Southwest at $R = 135''$ (position numbers 28, 29, 35, 43, 44, 51 and 52, in our notation) and shown in the figure as filled circles, are of special interest. These regions dominate the CO and $H\alpha$ emission in the outer two annuli in our observations, giving evidence that the spiral pattern in this galaxy, while not generally evident in the molecular distribution with our resolution, is in fact apparent and available for quantitative treatment at these locations.

Our results here demonstrate that the point by point SFRs, as measured from the $H\alpha$ flux, do not linearly follow the gas surface density. We will show in the next section that, with the use of an optimal averaging scheme, the spiral pattern will become visible in the CO distribution, and furthermore that a nonlinear relation will be found to hold between σ_p and $f_{H\alpha}$. Were the gas density and star formation rates linearly related, then this relation would be apparent at any resolution which included an appreciable number of clouds (HPBW

$> 20'' = 1 \text{ kpc}$). We will show that the spiral arm star formation efficiency is generally higher than the interarm efficiency and that our results can be expressed by a nonlinear dependence of SFR on ρ_p . To account for the relative strength of the $f_{H\alpha}$ on the arms we must consider the various attributes of the spiral density wave: its ability to compress the stellar and gaseous populations into higher surface density configurations, to increase cloud-cloud collision probabilities, and perhaps to increase mean cloud sizes. These considerations will be taken up in the following sections.

(ii) Spiral Phase Diagram

The emission properties of the spiral pattern may be more fully brought out by averaging the observed data in the coordinate system of the pattern itself, with the spiral represented as a continuous function of position angle with radius, $\Theta_{\text{arm}}(R_{\text{gal}})$. Because the two arms are nearly a constant 180° apart in position angle throughout the inner disk, a single function with an appropriate phase constant added will track either arm, although some corrections for distortions at $R = 140'' - 160''$ are required. The spiral phase function of Tully (1974c, Figure 4) was used for this purpose. It traces the spiral pattern, as defined by the innerarm dust lanes, and, in the absence of these, the innerarm optical edge, for over $5\pi/2$ radians.

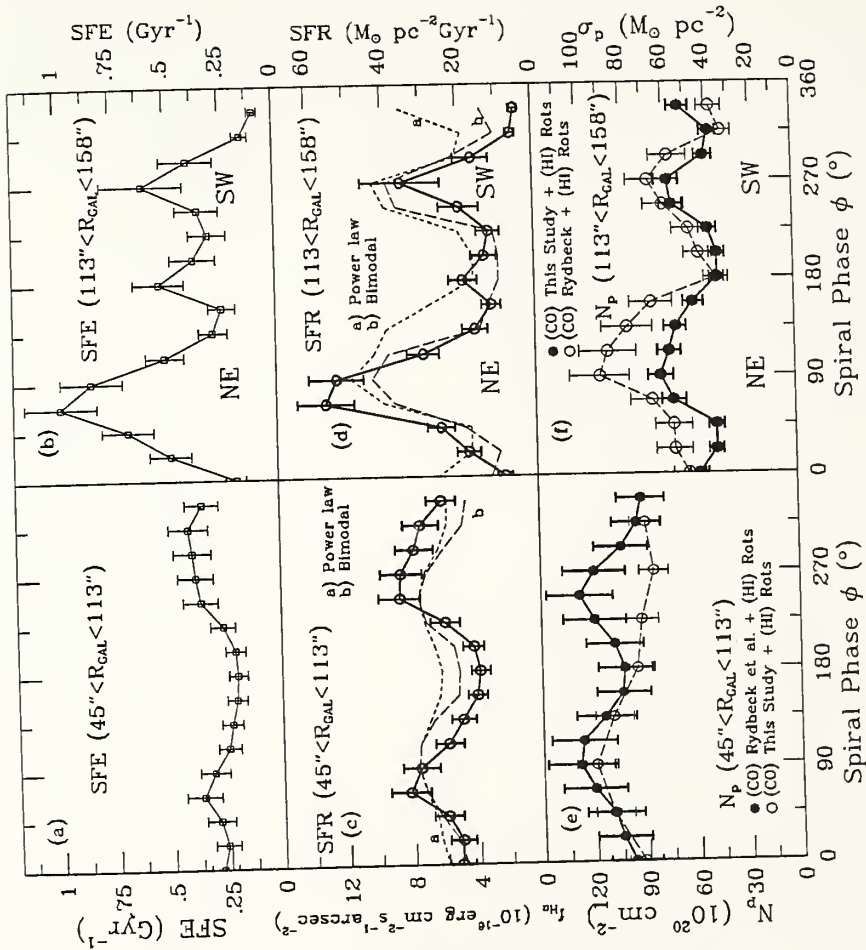
By interpolating the low resolution CO and $H\alpha$ data given in Table 1, we produced smooth deprojected surface distributions over the face

of the galaxy. Profiles in azimuth, $f_{H\alpha}(\theta_{gal})$, $I_{CO}(\theta_{gal})$, $\theta_{gal} = 0^\circ - 360^\circ$, were taken from $R_{gal} = 45''$ to $R_{gal} = 158''$ at each $2''$ increment. These azimuthal profiles were then binned into two groups, $R_{gal}=45''-113''$, and $R_{gal}=113''-158''$, and averaged, after first rotating each profile by $\theta_{arm}(R_{gal})$. In this way the arm terminating optically in the far South is always tracked with its dust lane appearing at $\phi = 90^\circ$, and the far North arm with its dust lane appearing at $\phi = 270^\circ$. The outer edges of each arm appear at higher $\phi = \theta_{gal} + \theta_{arm}(R_{gal}) + 90^\circ$ values than the inner edges.

The resultant distributions, sampled at 22.5° intervals in ϕ , are shown in Figure 7a-f and constitute a smoothing over radius in the coordinate system of the arms, which served to eliminate much of the intrinsic variation in the distributions. For each averaged annulus the final resolution was determined by inserting a delta function into the raw data and measuring the width at half power of the resulting peak. The resolution varies between $41''$ and $100''$ as described in the caption to Figure 7.

The outer annulus raw data points take on more weight in these averages because they sample a larger surface area, accentuating the positions of enhanced emission found therein. The above procedure was also repeated for the CO observations of Rydbeck, Hjalmarson and Rydbeck (1985; RHR) which comprised 74 spectra of the inner disk of M51 taken with $33''$ resolution and a different sampling scheme, with results included in Figures 7e and 7f. The spiral structure is clearly seen in

Figure 7a-f. The gas densities, star formation rates, and star formation efficiencies for two annuli, $45'' < R_{\text{gal}} < 113''$ (fig.s a,b,c) and $113'' < R_{\text{gal}} < 157''$ (fig.s d,e,f) as a function of phase angle relative to the spiral density wave. Dust lanes in the arm terminating in the far North are at $\phi=270^\circ$ and in the arm terminating (optically) in the South are at $\phi=90^\circ$. The arms' outer portions appear at larger ϕ values. The data, including the CO observations of Rydbeck, et al. (1985), were interpolated to yield a smooth distribution and then integrated in the coordinate system of the spiral pattern with final resolution of $100''$ in the inner arm and $76''$ in the outer arm for the data of this study and $54''$ and $41''$ for the Rydbeck et al. (1985) data. Averaging the data in this way smooths out the intrinsic scatter in the CO data and reveals the molecular arms (fig.s 8a,d). Shown in fig.s b and e are the best fits to the $\text{SFR}(\phi)$ functions using a power-law dependence (Model 8) and a "bimodal" dependence (Model 7), the latter including a linear term in ϕ_p on the interarm and a quadratic term in ϕ_p on the arm.



each radius regime in the SFR ($f_{\text{H}\alpha}$) distributions at 90° and 270° . The seven positions mentioned in the previous section dominate the Northeast and Southwest CO emission, and are chiefly responsible for the maxima seen in Figures 7e and 7f. The $f_{\text{H}\alpha}$ distribution shown in Figure 7d is verified via comparison with the similar result obtained by Tully (1974c, Figure 8).

The quantities plotted in Figures 7e and 7f are $N_{\text{p}} = N_{\text{p}}(\text{H}_2) + N_{\text{p}}(\text{HI})$, with the H_2 derived from the RHR and the present CO data sets, and the HI from the VLA observations (Rots 1985, personal communication), extrapolated to the same positions and comparable resolutions. The largest discrepancy between the data of this work and the RHR data is apparent at $\phi \approx 270^\circ$ in Figure 7e. The region in question is the origin of the far North arm, located just north to northwest of the central region ($R_{\text{sky}} \approx 60''$, $\Theta_{\text{sky}} \approx 335^\circ$). The sampling scheme of the present work straddles the spiral arm with positions 2-5 on the inside and positions 26, 39-41 on the outside, crossing it only at position 38. The RHR data crosses this arm three times with oversampled radial strips, each time detecting a relative maxima in I_{CO} at positions (0,4), (-4,4) and (-8,0) (RHR's notation). Because the RHR data, with its better resolution and comparably complete sampling inward of $R = 113''$ detects the arm, we will use these results for the inner annulus model fitting (Figure 7c) described below. Outside of $R_{\text{sky}} = 113''$, the data of the present work have much more complete sampling than the RHR data, so we use the results of this

work for the outer radii model fits. The selected data sets are shown with a heavy solid line in Figures 7e and 7f. (Note that the solid circles in Figure 7e are from Rydbeck et al., while the solid circles in Figure 7f are our data.)

We now examine the profiles of $f_{H\alpha}(\phi)$ and $N_p(\phi)$ shown in Figures 7c-f, where the interarm intensities appear as minima between the broad arm peaks centered at $\phi=90^\circ$ and 270° . Looking across the figure, the vertical scales are equal for each pair of panels. In Figures 7c and 7d the $H\alpha$ surface brightnesses have also been converted to star formation rates as per Equation II.5 as indicated on the right hand scale. Comparing Figure 7e to 7f, we can see the falloff in gas surface density going from the inner to the outer annulus. A smaller drop in the interarm $H\alpha$ emission is seen going to the outer radii, while the peaks of the spiral pattern in $H\alpha$ emission in the outer annulus appear to be stronger and show a greater fractional deviation from the interarm value there. It is evident that the star formation rates indicated by the $H\alpha$ profiles and the gas density profiles are related. To better establish their relationship, we have taken the 16 gas density and SFR values in each annulus from the spiral phase diagram and have looked for some simple functional dependence between these data. It is important to keep in mind that the results reported below are highly dependent on the spatial resolution employed.

We have considered three different types of models (Table 5a) to describe the σ_p , SFR relationship: a) models which treat the arms and

TABLE 5a (NOTES)

In all cases A and IA stand for the arm and interarm positions.

These model fits have been computed using linear regression techniques (Bevington 1969). In all models the χ^2 values are derived from: $1/(N-\text{PARAM}-1) \sum (\text{SFR}_o - \text{SFR}_f)^2$, where N is the number of data points (N=16), PARAM is the number of free parameters, (PARAM=1-4), SFR_o is the observed star formation rate, and SFR_f is the rate from the model fit.

*Model fits 8-11 are computed from a linearized form of the model using $(\ln(\sigma_p), \ln(\text{SFR}_o))$ values and a SFR^2 weighting factor. The errors quoted for leading coefficients, e.g. σ_{C_1} for the form $\ln(\text{SFR}) = \ln(C_1 \sigma_p^2)$, represents the error such that C_1 (within errors) = $C_1 \exp(\pm \sigma_{C_1})$.

TABLE 5a
STAR FORMATION RATE MODEL FITS

Index	Model	Inner Annulus (45" < R _{gal} < 113")			Outer Annulus (113" < R _{gal} < 158")			
		C ₁	σ _{C1}	C ₂ ± σ _{C2}	χ ²	C ₁ ± σ _{C1}	C ₂ ± σ _{C2}	χ ²
1	SFR = C ₁ σ _p (IA & A)	0.32 ± 0.01	---	---	48	0.50 ± 0.02	---	175
2	SFR = C ₁ σ _p ² (IA & A)	0.0035 ± 0.0002	---	---	49	0.0098 ± 0.0004	---	139
3	SFR = C ₁ + C ₂ σ _p (IA & A)	-2.63 ± 12.9	---	0.35 ± 0.14	53	-22.8 ± 5.5	0.96 ± 0.12	199
4	SFR = { C ₁ σ _p (IA) C ₂ σ _p (A)	0.29 ± 0.02	---	0.34 ± 0.02	32	0.28 ± 0.02	0.68 ± 0.04	99
5	SFR = { C ₁ σ _p (IA) C ₂ σ _p ² (A)	0.29 ± 0.02	---	0.0035 ± 0.0002	37	0.28 ± 0.02	0.012 ± 0.0007	93
6	SFR = { C ₁ σ _p ² (IA) C ₂ σ _p ² (A)	0.0035 ± 0.0003	---	0.0035 ± 0.0002	39	0.0058 ± 0.0005	0.012 ± 0.0007	104
7	SFR = { C ₁ σ _p (IA) C ₁ σ _p + C ₂ σ _p ² (A)	0.29 ± 0.02	---	0.0005 ± 0.0003	33	0.28 ± 0.02	0.007 ± 0.0009	92
8*	SFR = C ₁ σ _p ^{C₂} (IA & A)	0.55 ± 2.78	---	0.90 ± 0.62	59	0.015 ± 0.18	1.97 ± 0.83	282
9*	SFR = { C ₁ σ _p ^{C₂} (IA) C ₁ σ _p ^{C₃} (A)	87.8 ± 4.03	---	-0.29 ± 0.92	49	0.41 ± 0.25	0.97 ± 0.72	148
		C ₃ : -0.21 ± 0.01	---	---	---	C ₃ : 1.16 ± 0.69	---	---
10*	SFR = { C ₁ σ _p (IA) C ₂ σ _p ^{C₃} (A)	0.29 ± 0.02	---	2.81 ± 0.65	52	0.28 ± 0.14	0.084 ± 0.29	129
		C ₃ : 0.54 ± 0.14	---	---	---	C ₃ : 1.56 ± 0.07	---	---
11*	SFR = { C ₁ σ _p ^{C₂} (IA) C ₃ σ _p ^{C₄} (A)	4.6 × 10 ⁸ ± 1.3	---	-3.3 ± 0.29	39	110. ± 0.5	-0.54 ± 0.15	135
		C ₃ : 2.8 ± 0.7	C ₄ : 0.54 ± 0.14	---	---	C ₃ : 0.08 ± 0.29	C ₄ : 1.56 ± 0.07	---

interarms with the same functional dependence (Models 1, 2, 3 and 8.); models which treat the arms and interarms separately with a linear and/or quadratic dependency (Models 4, 5, 6 and 7); and models treating the arms and interarms independently leaving the arm and/or interarm exponent as a free parameter (Models 9, 10 and 11). A good indication of the success of the various models is given by the χ^2 value resulting from each fit (Table 5a). One of the best results is obtained from Model 7, which incorporates a linear dependence on the arms and a linear and quadratic dependency on the arms. In Figure 7c and d we display this model termed the "Bimodal Fit" and contrast its performance with the "Power Law" model (No. 8) which treats the arms and interarms with the same exponential form, $SFR = C_1 \alpha_p^{C_2}$. The difference in the χ^2 results for two models is not due to the number of parameters used, because models 7 and 8 each have 2 free parameters. In Figures 7c and 7d the power law model can be seen to fit the data poorly on the interarms.

The results of the model fits of Table 5a show that the spiral arm nonlinear dependence ("non-linear" as compared to the off-arm coefficient) becomes most important in the outer annulus. In models 4 and 6 the on-arm coefficient in the outer annulus is 2 to 4 times larger than the off-arm coefficient. This suggests that there may be some mechanism causing an increase in the efficiency of star formation on the arms in the outer annulus, a mechanism that does not effect the star formation rate on the inner annulus arms.

In comparing models 5 and 7, we see that the resulting χ^2 was not significantly lower in model 7 (mixed linear and quadratic star formation on the arms), indicating that the importance of linear star formation within the spiral arms is undetermined. The χ^2 values in Table 5a do indicate that the presence of a linear term on the interarms and a nonlinear term on the arms, provides a better fit to the data than the other models. We wish to restate, however, that a quadratic exponent can not uniquely selected by the data. Our observations do not resolve the inferred spiral pattern, so that if star formation occurs nonlinearly with gas density on the arms, the exponent found will be largely resolution dependent. Experimentation with models of bimodal star formation following higher powers of the gas density on the arms alone ($\alpha_p^3 - \alpha_p^7$) yielded χ^2 values that are within a few percent of the quadratic-bimodal model (No. 7) indicating that, even at a fixed resolution, we can not uniquely specify the nonlinear exponent. In Table 5b we show that very different models will tend to produce the same ratio of arm to total star formation indicating that most of the "bimodal" models are capable of replicating the observed values, and none is uniquely selected. Furthermore, we have found that the fraction of star formation resulting from the nonlinear term in the models using exponents greater than 2 on the arms remains nearly equal to the fractions listed in Table 5b. This only indicates that when the exponent is introduced as a third free parameter, the exponent and its leading coefficient are not sufficiently independent to yield a unique solution. It is still a

TABLE 5b (NOTES)

*See notes of Table 5a.

Column (1) The mean interarm star formation rate in $M_{\odot} \text{ pc}^{-2} \text{ Gyr}^{-1}$.

Column (2) The mean arm star formation rate in $M_{\odot} \text{ pc}^{-2} \text{ Gyr}^{-1}$.

Column (3) The (mean arm/mean total) star formation rates in the annulus.

Column (4) For model 7 A_1 indicates the mean on-arm star formation rate resulting from the linear term $C_1 \sigma_p$.

Column (5) For model 7 A_q indicates the mean on-arm star formation rate resulting from the quadratic term $C_2 \sigma_p^2$.

Column (6) The ratio of the mean quadratic on-arm star formation rate to the mean total (arm+interarm) star formation rate in the annulus.

Column (7) The ratio of the mean quadratic on-arm star formation rate to the mean on-arm linear star formation rate in the annulus.

TABLE 5b

STAR FORMATION RATES FROM ARM AN INTERARM TERMS

Index	Model	Inner Annulus (45" < R _{gal} < 113")			Outer Annulus (113" < R _{gal} < 158")						
		IA (1)	A (2)	A/TOT (3)	IA (1)	A (2)	A/TOT (3)				
4	SFR = $\begin{cases} C_1 \alpha_p & \text{(IA)} \\ C_2 \alpha_p & \text{(A)} \end{cases}$	23	32	0.58	12	36	0.75				
		IA	A	A/TOT	IA	A	A/TOT				
10*	SFR = $\begin{cases} C_1 \alpha_p & \text{(IA)} \\ C_2 \alpha_p C_3 & \text{(A)} \end{cases}$	23	34	0.60	12	41	0.77				
		IA	A	A/TOT	IA	A	A/TOT				
11*	SFR = $\begin{cases} C_1 \alpha_p^{C_2} & \text{(IA)} \\ C_3 \alpha_p^{C_4} & \text{(A)} \end{cases}$	24	34	0.58	15	41	0.73				
		IA	A ₁	A _q	q/TOT	q/A ₁	IA	A ₁	A _q	q/TOT	q/A ₁
		(1)	(4)	(5)	(6)	(7)	(1)	(2)	(3)	(6)	(7)
7	SFR = $\begin{cases} C_1 \alpha_p & \text{(IA)} \\ C_1 \alpha_p + C_2 \alpha_p^2 & \text{(A)} \end{cases}$	23	27	4.7	0.09	0.17	12	15	21	0.44	1.4

possibility that linear star formation on the spiral arms (i.e. on-arm star formation with the same coefficient as that found on the interarms) may still be present. In the case of the mixed linear and quadratic model (no. 7) it can be seen from Table 5b that the linear term on the arms can account for as much as half of the total on-arm star formation.

Because the quadratic and higher order bimodal models produce significantly lower χ^2 values than a linear or power law model, we have evidence that the star formation as indicated by the H α flux follows a nonlinear rule and does so principally on the spiral arms. It should also be noted that there are no constants C_{b1} , C_{b2} which produce a good fit to both radius regimes simultaneously. Thus, this simple law is incomplete in describing the factors that go into determining the SFRs in M51. In the following section we look for such additional factors while including in our consideration the $15'' < R < 60''$ radius regime.

d) The Inner 60''

Despite the fact that the inner 60'' of M51 has now been observed in the CO ($J = 1 \rightarrow 0$) transition at resolutions including 45'' (this work), 33'' (RHR), 15'' (Sofue, personal communication), and 7'' (Lo et al. 1987), there still exists some controversy as to the molecular gas distribution in this region. One major discrepancy concerns the presence or absence of a central hole in CO emission from $R \sim 0''-20''$, an issue which is not germane to the topic of this paper: the star

formation in the disk. In the following discussion we will only consider the central region outward of $R_{\text{sky}}=20''$.

Between $R=20''$ and $R=60''$, the CO interferometric map of Lo et al. (1987) and the zero spacings provided by single dish observations (OVRO and this study), are compared to the PDS and CCD H α images in an attempt to extend our analysis to the central region and to higher resolution.

The interferometer map shows CO emission structures, some as long as 3 kpc, extending out from the nucleus, and curving along, if not always directly atop, the spiral arms defined by radio continuum ridges and HII regions. The majority of the CO emission is missed, however, by the interferometer. Lo et al. (1987) estimate that, due to the limited velocity coverage afforded their spectrometers, that 10% of the emission in a 60" field north of the nucleus, and 33% of the emission in a 60" field south of nucleus is undetected. With our comparable beam size and matching positions (nos. 8 and 18), we are able to confirm this estimate. Furthermore, Lo et al. (1987) find that of the remaining flux, 70% is resolved-out in the sense that it presents structure greater than 40", thereby establishing a background distribution of molecular clouds. If uniformly distributed, the cloud background implies an arm/interarm N_p ratio of between 15/1 and 3/1 where a constant conversion to N_p is assumed. But the detected emission does not extend continuously along the arms, but rather is seen in interrupted structures, much in the way HII regions are seen to be arranged in groups along the arms.

We have compared the detailed CO map with the 3" resolution CCD H α image, and find that the large CO features detected by Lo et al. (1987) lie in part upon bright HII regions, but also to extend along the arm pattern across stretches where no HII regions are seen. Also present in the CO map are smaller (20") emission features, some of which lie just interior to the H α arms and others located in definitive interarm regions. These features appear in the version of their map (Figure 2, Lo et al. 1987) produced by including channel fluxes down to a low threshold value and may possibly be artifacts. Thus, in comparing the CO and H α map, we are unable to select a particular mechanism for the interaction of the clouds with the spiral density wave, both because of the unknown distribution of the undetected CO emission component, and because there may exist cloud complexes visible both upstream and downstream of the spiral arms. We also do not see in the detailed CCD image a clear trend for the HII regions to lie downstream of the dust lanes. For example, HII regions are seen to lie upstream of the dust lanes and molecular emission in a region 45" northwest from the nucleus.

Using the interferometer map and the PDS H α image we have attempted to assess the arm and interarm star formation rates and N_p values. To do so, we choose the CO emission regions from the Lo et al. (1987) map that are the most confined to the spiral arms. We selected three on-arm CO emission regions located 60" north of the center (I), 30" to the SSW (II) and 30" to the ESE (III) of the center

(see Table 6). For comparison, interarm SFR values were established by taking azimuthal means of the interarm $H\alpha$ brightness at each radius. Our computation of the parameters for these regions were hampered by calibration uncertainties, mainly in the $H\alpha$ data set. Extinction values for these particular regions were estimated from the average of extinction measurements from the literature for regions inward of $R=60''$ (Jensen, Strom and Strom 1976; McCall 1982; vK). These studies show a large scatter in A_V from region to region, which produces the large uncertainties given for $f_{H\alpha}$ in Table 6.

Likewise, the arm CO intensities have an associated 25% uncertainty (Lo, personal communication). We have obtained the upper and lower estimates of the interarm intensity by using the estimated 3/1 - 15/1 arm/interarm contrast found in brightness temperature by the authors. The $H\alpha$ and CO uncertainties combined allow us to only coarsely bracket the star formation efficiencies in these three regions. Of note is region I (Table 6), the most compact of the three, which manifests a very high efficiency. Further conclusions regarding the detailed SFEs in the central region will have to await the acquisition of $H\alpha$ extinction measurements for the particular HII regions associated with the cloud complexes seen by Lo et al. (1987), and intermediate resolution (HPBW $\approx 15''$) single dish measurements to locate the CO flux unresolved by the interferometer.

TABLE 6 (NOTES)

Row (1) These three regions are selected from bright CO features in the interferometric map of Lo et al. (1987) because they lie upon the H α spiral arms.

Row (2) R_{gal} is the radial extent of the region as measured in the plane of the galaxy.

Row (3) θ_{sky} is the azimuthal extent of the feature as measured in the plane of the sky.

Row (4) The approximate length of the major and minor axes of the region.

Row (5) C is the extinction correction factor derived from central A_V measurements as discussed in Appendix A.

Row (6) $f'_{H\alpha}$ is the uncorrected H α flux from the PDS image.

Row (7) $f_{H\alpha} = C f'_{H\alpha}$ is the range of the corrected brightness.

Row (8) I_{CO} of the feature is obtained from the maps of Lo et al. (1987) by adding the middle emission contour value and the underlying "resolved-out" background component measured by single dish observations.

Row (9) SFE is the range star formation efficiency is obtained from $f_{H\alpha}$ and I_{CO} following the methods described in the text.

Row (10) $f'_{H\alpha}$ is obtained by identifying and averaging the H α brightness seen at the R_{gal} range on the PDS image.

Row (11) $f_{H\alpha} = C f'_{H\alpha}$ is the corrected brightness.

Row (12) I_{CO} is the "resolved-out" I_{CO} component which we put following Lo et al. (1987) between 1/15 and 1/3 the arm intensity.

Row (13) SFE, the range star formation efficiency is obtained from $f_{H\alpha}$ and I_{CO} following the methods described in the text. The upper limits in row 13 correspond to the situation of almost no interarm gas, a situation we consider unlikely.

TABLE 6
 H α AND CO EMISSION IN THREE CENTRAL LOCATIONS

(1) Region	I	II	III
(2) R_{gal}	55-60"	30-45"	35-55"
(3) θ_{sky}	-15° - 10°	40° - 170°	175° - 275°
(4) length x width	27 x 18"	90 x 10"	70 x 16"
(5) C (extinction correction factor)	3.3 \pm 2.1	3.3 \pm 2.1	3.3 \pm 2.1

On-Arm Values for these locations			
(6) $f'_{H\alpha}$ 10^{-16} erg/(cm ² s arcsec ²)	16	6	5
(7) $f_{H\alpha}$ 10^{-16} erg/(cm ² s arcsec ²)	19-86	7-32	6-27
(8) I_{CO} (K[T _R] km s ⁻¹)	12 \pm 25%	34 \pm 25%	31 \pm 25%
(9) SFE (Gyr ⁻¹)	1.4-6.4	0.18-0.71	0.17-0.78

Interarm Values at these Radii			
(10) $f'_{H\alpha}$ 10^{-16} erg/(cm ² s arcsec ²)	0.3	0.7	0.7
(11) $f_{H\alpha}$ 10^{-16} erg/(cm ² s arcsec ²)	0.3-1.6	0.8-3.8	0.8-3.8
(12) I_{CO} (K[T _R] km s ⁻¹)	0.8-4.0	2.3-11	2.1-10.3
(13) SFE (Gyr ⁻¹)	0.07-1.8	0.07-1.5	0.8-1.6

e) Conclusions

We summarize our results for the arm and interarm SFRs and N_p in Table 7. In this table we include our results from the previous sections. While the interarm SFRs and N_p values are seen to be lower in the inner 60" than those in the disk, this is most likely a resolution effect.

The most striking result shown in Table 7 is that the SFR on the arms rises in the outer annulus while the gas density falls. We will compare this result to theoretical models of star formation in the next chapter.

We summarize below the major conclusions of this chapter.

1) In the inner disk and central region the molecular hydrogen density strongly dominates over the atomic hydrogen density, with $\sigma_p(\text{HI})/\sigma_p(\text{H}_2)$ rising from 3% to 20% between $R=20''$ and $R=145''$.

2) The $\sigma_p(R)$ distribution falls off with radius as $1/R$.

3) In azimuthal annuli, the total $\text{H}\alpha$ flux falls off in direct proportion to the CO flux, implying $\text{MSFR} \sim \sigma_p$, and the MSFE is roughly constant. The MSFE does show a small upward trend in the outer annulus, at $R \sim 145''$.

4) In 45° sector averages, a constant σ_p density is maintained while the $\text{H}\alpha$ brightness varies from sector to sector.

TABLE 7
SUMMARY OF ARM AND INTERARM PARAMETERS

R_{gal}	SFR_A	SFR_{IA}	N_{PA}	N_{PIA}	SFE_A	SFE_{IA}	SFE_A/SFE_{IA}
	$(M_{\odot} \text{ pc}^{-2} \text{ Gyr}^{-1})$		(protons cm^{-2})		(Gyr^{-1})		
40"	110-267	8-13	72±25%	10-55	-	-	-
80"	30	20	115	95	0.33	0.26	1.2
135"	35	15	70	45	0.63	0.42	1.5

TABLE 7 (NOTES)

The subscripts A and IA stand for the arm and interarm regions. The first row quantities were derived from the mean values of Table 6. Star formation efficiency estimates in this region contain prohibitably large uncertainties as discussed in §IIIId. The values in the second and third rows are obtained from the spiral phase analysis of §IIIc.

5) Excesses in the $H\alpha$ brightness and the σ_p density are correlated with the spiral pattern, i.e., there are both $H\alpha$ and gas "arms", although the patterns shown in these distributions are not strictly continuous.

6) By taking radial averages while rotating in azimuth (so as to maintain a constant spiral phase) we have found the average arm overdensity in σ_p and $f_{H\alpha}$. Both the $H\alpha$ and the σ_p distributions are elevated on the spiral arms, with the $f_{H\alpha}$ more highly elevated than the σ_p distribution, especially outward of $R=113''$. The dependence of the MSFR, (and the implied SFR) upon σ_p is also both resolution and radius dependent. While a unique functional form cannot be specified, the observed rates are consistent with SFR proportional to σ_p on the interarms and SFR proportional to σ_p^2 on the arms. The arm and interarm distributions sum together to yield an overall linear relation between the SFR and σ_p .

CHAPTER IV

DISCUSSION OF THE STAR FORMATION EFFICIENCY

a) Introduction

In this chapter we will relate our findings concerning the star formation rates and efficiencies in M51's disk to currently held theories. We will first examine the result that the spiral arms manifest higher star forming efficiencies than the interarms and show that this result is in agreement with the cloud-cloud collision model(s) of star formation. Collisions are expected to be more frequent on the arms because of cloud number density enhancements and cloud velocity dispersion enhancements, and we relate the observations, models and simulations of these effects to the particular case of M51. A second result which we will discuss is the radial behavior of the averaged SFE. It is interesting that this function is fairly flat with radius out to the region $R=135''$ to $160''$, and in this outer annulus higher efficiencies are seen. We shall show that this result is not in agreement with the predictions of two different models of disk star formation. We suggest that the interaction of M51 with the nearby companion galaxy NGC 5195 might be responsible for the higher outer disk efficiencies. Finally, we compare the star forming efficiency as averaged over the lifetime of the galaxy to that currently observed. The large difference seen could indicate that the entire galaxy is in a period of high activity due to the close proximity of the companion.

b) The High Star Formation Efficiency on M51's Spiral Arms

The results of the power law and bimodal fits in the spiral phase analysis have led us to conclude that there is a nonlinear dependency of star formation upon gas density on the arms. This assumes that the same IMF applies to the arms and interarms, which may not be the case. Since $H\alpha$ flux traces the massive stars, our result more directly implies that that massive star formation efficiency is elevated on the arms. We now discuss two current models of massive star formation where such nonlinear dependence on the gas density is expected.

i) Insupportable Mass Growth

Any mechanism which produces massive stars in molecular clouds must do so by overcoming the cloud's internal means of support. Shu, Adams, and Lizano (1986) argue that support through magnetic fields is dominant over turbulent support. They base this conclusion on the observation that polarization maps of individual clouds show polarization vectors maintaining well ordered alignment over the clouds' entire extents, as opposed to a tangled configuration expected in clouds supported by turbulence. In their star formation scenario, cloud-cloud collisions result in agglomerations which, while containing the sum of the individual cloud masses, do not necessarily contain the sum of the magnetic fluxes. The extent to which the net flux increases is determined by the extent to which the clouds collide across, rather than along their average field directions. Thus, on the

average, cloud mergers lead to a pressure imbalance with gravity dominating, and to eventually insupportable mass growth. Shu et al. suggest that O and B stars are favored in this production mechanism, because a cloud merger which results in a supercritical mass configuration can produce rapid (although magnetically decelerated) contraction. This suggests that cloud growth occurs principally on the spiral arms, with super critical clouds remaining in such a state for a short time. A consequence of this model would be a high fraction of the most massive clouds situated on the spiral arms. This, however, is not borne out in the Milky Way.

ii) Cloud Collision Model

In the observations of Scoville et al. (1987) for a sample of 314 clouds with determined distances and masses, the large (diameter $\ell > 20$ pc) and small ($\ell < 20$ pc) clouds were found to be similarly distributed in the longitude-velocity plane, with neither population resembling an arm population in this plane, as do, for example, the HII regions and molecular clouds with HII regions (c.f. Solomon, Sanders and Rivolo 1985). (However, Kwan and Valdez 1987, henceforth KV, point out that the presence of noncircular motions may make a spiral arm population difficult to discern on the l-v plane.) Furthermore, in clouds with HII regions, the Lyman flux per cloud mass diminishes with increasing cloud mass (c.f. Scoville, Sanders, and Clemens 1986), implying that the sort of violent collapse which could encompass a supercritical cloud's entire volume is not in evidence. Scoville et al. (1987)

suggest that the dominant mode of O and B star production is due to the shock wave and compression experienced in cloud-cloud collisions. In support of this idea, the authors note that the typical HII region is found to be very centrally located within a GMC's CO emission area; they identify the heated molecular gas surrounding the HII region as the interface between clouds in collision. Despite their small linear cross-sections, $\sigma_{1CS} \sim \ell$, small molecular clouds are expected to have high collision rates. Since the collision rate for clouds goes as N_c^2 , the number surface density squared, and number distribution in diameter goes as $N_c(\langle \ell \rangle) \sim \ell^{-2.5}$ for the Milky Way, small cloud collisions are expected to be far more frequent than large cloud collisions. Scoville et al. identify a population of relatively small GMCs ($5 \text{ pc} < \ell < 30 \text{ pc}$) which possess HII regions and display internal dispersion velocities nearly twice as large as clouds of the same size lacking HII regions. The enhanced velocity dispersion and temperatures of these clouds are interpreted to be artifacts of collisions.

iii) The Collision Rate

The rate ω (number of collisions per time per area) is given by $\omega = N_c^2 \sigma_v \sigma_{1CS}$, where N_c is the number surface density of clouds, σ_v is the population's velocity dispersion, and σ_{1CS} is the mean linear cross-section; $\sigma_{1CS} \approx \langle \ell \rangle$ with $\langle \ell \rangle$ being the mean cloud diameter. This simplistic relationship assumes a cloud monolayer, which, for our present purposes, will suffice.

Assuming, to first order, that the cloud size distribution is equally maintained on the arms and interarms (Scoville, Sanders and Clemens 1986; but see also KV), then $N_c \sim \rho_p$. With collisions responsible for initializing star formation, $SFR \sim \omega \sim \rho_p^2 \alpha_V \sigma_{1CS}$. This form provides a physical motivation for the bimodal model of Figures 7c and 7d. The enhancement of N_p on the arms is also in agreement with the predictions of the SDW theory. On the spiral arms, gas densities predicted from linear and nonlinear density wave theory are 50% to 300% higher than underlying distribution (Tully 1974c). Similarly high density enhancements are predicted for the Milky Way by way of computer simulations of its cloud population under the influence of a spiral potential as shown by KV. Their study of a discrete cloud population subjected to a 5% spiral potential above the underlying Schmidt potential, with the inclusion of inter-cloud gravitational attraction and cloud mergers, shows molecular arms appearing as broad structures (of azimuthal width 51° at $R=6$ kpc) having average density enhancements of 150% - 300% and containing 50% of the total molecular disk mass. Cloud growth is halted in the KV models through cloud fragmentation when a cloud's mass exceeds $10^6 M_\odot$, effectively accounting for the disruptive effect of star formation and to produce a cloud upper mass limit commensurate with observations. They find that the degree to which massive ($M > 10^6$) clouds are confined to the arms is proportional to the fragmentation timescale, t_{gs} . With $t_{gs} = 70$ Myr (Model A) the spiral phase diagrams of KV resemble our Figures 7e and 7f. In this case, while the SDW increases N_c on the arms, it leaves as much as 50% by mass of the GMC population on the interarms.

The effect of the SDW on the cloud velocity dispersion is somewhat less clear. In KV's simulations, the 5% potential produces no spiral shock front (the simulations include no hydrodynamic modeling) and the net effect of the spiral potential and cloud interactions is to stabilize the mean σ_v near 3 km s^{-1} , as is observed for the Milky Way (Clemens 1985), with some increase on the arms. M51's spiral potential appears, however, to be stronger than the 5% potential employed by KV, and its strength is evidenced both by nonthermal radio continuum ridges seen along the inner arm dust lanes (Mathewson, van der Kruit, and Brouw 1974) and the coherent streaming motions in both the radial and tangential directions seen by Tully (1974c). Tully (1974c) fit these motions to linear density wave theory, and so obtained a spiral potential strength of 15%-20%. The $\text{H}\alpha$ streaming motions are of magnitude $20\text{-}40 \text{ km s}^{-1}$, while RHR find even stronger molecular streaming motions (in CO) as high as 70 km s^{-1} , where the minor axis crosses the spiral arms at $R \approx 88''$. We are unable to confirm this latter result due to insufficient spatial resolution, but we note that if the phenomenon is a global one, the consequences of the cloud streaming may be profound. The result of such streaming, where the molecular clouds respond fully to the shock wave associated with the nonlinear density wave model (Roberts 1969), is dramatically portrayed in the M51 disk simulations of Kimura and Tosa (1985). Following the methods of Bash (1979) and Bash and Peters (1976), clouds emerging from the shock produced by a 15% spiral potential follow ballistic trajectories determined by their postshock velocities and the spiral and underlying

potentials. The net effect, for clouds living 1.6×10^8 years after ejection (the longest lifetime considered) is the filling-in of the interarm regions with clouds in perturbed trajectories, with a steady state configuration greatly resembling that of KV. The spiral arms still stand out as 100% density enhancements in the model of Kimura and Tosa, in part because the model ascribes the role of cloud creation (from HI) to the spiral shock. Thus, we have seen, under two extremely different sets of premises regarding cloud creation, evolution, and kinematics, (i.e. the KV and Kimura and Tosa simulations) similar equilibrium configurations emerging, each resembling that found in M51. The two pictures can be observationally distinguished only with high resolution observations of the preshock and postshock gas densities and kinematics. Some initial evidence for the large cloud velocities, but against the creation of GMCs from HI at the arms is found from the fact that the molecular surface density does not increase while crossing the observed velocity discontinuities seen at $R=88''$ in the $33''$ resolution observations of RHR.

All of the models discussed above yield enhanced values of α_v and N_c on the arms, and therefore provide a natural explanation for the high efficiencies seen on the spiral arms if cloud collisions and mergers drive the SFR. Assuming that the massive star formation rate is proportional to the cloud collision frequency ω , and ω is in turn proportional to $(\alpha_v \sigma_{lcs} \sigma_p^2)$, the model fits of Table 8a can be given physical meaning. In model 6, for example, with quadratic star

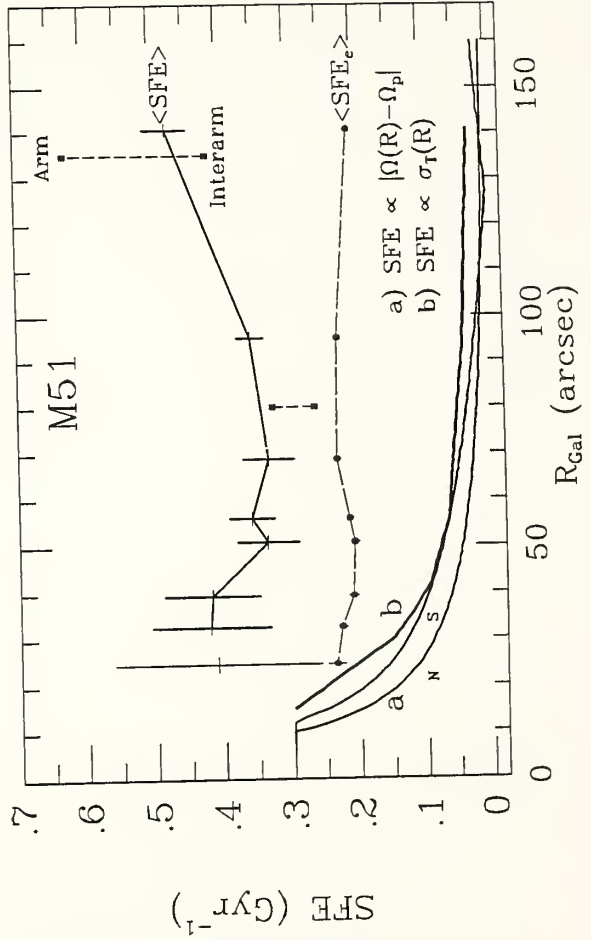
formation ($SFR = C \alpha_p^2$) on both the arms and interarms, the two-fold higher coefficient C for the on-arm term as compared with the interarm term in the outer annulus may be interpreted as the combination of enhanced α_v and σ_{lcs} values on the arms. Likewise, in comparing the α_p^2 coefficients for model 7 (linear off-arm, quadratic on-arm), we see a 14-fold increase in this coefficient (C_2) between the on-arm terms of the inner and outer annulus. This may be in part due to an increase of ($\alpha_v \sigma_{lcs}$) with radius. Resolution effects dependent on radius (such as beam size vs. arm and interarm widths) may also play an important role in determining the modeled value of this coefficient between the two annuli.

While cannot uniquely determine the functional dependence of SFR on α_p , we do note that in each radius regime examined, the arms show higher efficiencies (SFR/α_p) than the interarms. The simplest explanation of this phenomenon is that, on the arms, the conditions are favorable for enhanced collision rates, with rate ω given by $\omega \sim \alpha_v \sigma_{lcs} \alpha_p^2$, and that these collisions are responsible for the high star formation rates and efficiencies seen.

c) The Radial Dependence of the Star Formation Efficiency

The radial behavior of the star formation efficiency, $\langle SFE(R_{gal}) \rangle$, was obtained using azimuthal averages (§IIIb and Table 3a) and is presented as the top curve in Figure 8. There is large uncertainty for this function in the central region due to calibration uncertainty in

Figure 8. The observed and modeled star formation efficiencies plotted against galactic radius. The upper curve shows the current efficiency $\langle \text{SFR} \rangle / \langle \rho \rangle$ averaged over each radial bin, where the SFR is extrapolated from the MSFR using an extended Miller-Scalo IMF. The vertical dashed lines show the arm and interarm efficiencies at $R_{\text{gal}} = 80''$ and $135''$ using η_H , estimates Rydbeck et al. (1985) and this study, respectively. The dashed curve shows $\langle \text{SFE} \rangle = 1/[T(1-f)] \ln[\sigma_1(R)/\sigma_{\text{gas}}(R)]$, a measure of the efficiency averaged over the lifetime of the disk, as indicated by the low mass stellar population. Here $T=10$ Gyr and $f=0.2$. Curves a, (N and S), give the normalized angular velocity of material passing through the spiral density wave (an important parameter in the model of GM, see §IV.c.iii) using the North and South rotation curves of Goad, deVerry and Goad (1979) and the pattern speed from Tully (1974c). Curve b shows the total mass distribution with radius, an important parameter in the $\text{SFR} \sim \rho_{\text{gas}} \sigma$ model of Dopita (1985). All parameters are scaled to $D=9.6$ Mpc.



the $H\alpha$ data, but the outer 3 points in the top curve of Figure 8, being derived from the average of over 40 observations in each distribution, (CO , HI , and $H\alpha$), and the extinctions of about 30 HII regions, are of higher reliability. A distinct rise in the function is visible at the radius $R_{gal} \sim 140''$. Superimposed on this curve, as hatched vertical lines, are the arm and interarm efficiencies from the spiral phase analysis (§IIIc). The arm and interarm efficiencies at $R_{gal}=75''$ are lower than the mean value of $\langle SFE(R) \rangle$ here because the former points were established using the CO observations of RHR who measure higher σ_p at this radius than was found by us. We turn our attention now toward two models which give predictions concerning the arm, interarm, and azimuthal mean SFEs.

i) A Model Dependent on the Velocity of Gas Through the
Spiral Density Wave

We have compared our results to the density-wave stellar-production model of Gusten and Mezger (1983, henceforth GM). The motivation for this model was to account for the observed variations in the longitudinal distribution of radio continuum emission from the Milky Way, in terms of star formation rates that depend strongly on the location of a two-armed density wave. Recasting their expression III.7 into our nomenclature, the MSFRs on the arms and interarms, τ_a and Ψ_{1a} , are given by:

$$\Psi_a(R) = \alpha_a \sigma_p(R) R (\Omega(R) - \Omega_p) \quad (IV.1)$$

$$\psi_{ia}(R) = \alpha_{ia} \alpha_p(R) \quad (IV.2)$$

where $R(\Omega(R) - \Omega_p) = V(R)$ is the speed with which the gas α_p travels through the spiral density wave (SDW) and α_a and α_{ia} are undetermined constant coefficients. In this model the SFE = SFR / α_p is given by:

$$SFE_a(R) = \alpha_a R (\Omega(R) - \Omega_p) \quad (IV.3)$$

$$SFE_{ia}(R) = \alpha_{ia} \quad (IV.4)$$

and the annular average value $\langle SFE(R) \rangle$ by:

$$\langle SFE(R) \rangle = A_T^{-1} (A_a SFE_a + A_{ia} SFE_{ia}) \quad (IV.5)$$

where the A values are the arm, interarm, and total surface areas in an annulus; $A_T = A_a + A_{ia}$.

The SFE results, shown in Figure 8, do not show these functional forms. In particular, GM have SFE_a going as $V(R) = V_{circ} - R\Omega_p$. For M51, within the range $20'' < R < 124''$, $R \Omega(R) = V_{circ} \approx \text{constant}$, giving:

$$SFE_a = \alpha_a V_{circ} (1 - R/124'') \quad (IV.6)$$

which comprises a linear decrease in SFE_a with radius, where 124'' marks the corotation radius, ($\Omega(124'') = \Omega_p$, Tully 1974c). It can be seen in Figure 8 that the SFE_a points (upper squares) do not show this decline with radius.

The mean efficiencies of the model may be found by inserting the area fractions into the equation for $\langle SFE(R) \rangle$. GM treat A_a as a

constant. In this representation, A_a accounts for the immediate shock front associated with a density wave, and depends only upon the linear extent of the SDW through the annulus. Since M51's arms open nearly logarithmically (i.e. with a constant pitch angle, Kennicutt 1981), then A_a is approximately constant, while A_{1a} grows in proportion to radius. For large R , $A_{1a} \approx A_T$. Thus,

$$\langle \text{SFE}(R) \rangle \approx (\text{SFE}_a A_a + \text{SFE}_{1a} A_T) / A_T \quad (\text{IV.7})$$

$$\approx \alpha_a (\Omega(R) - \Omega_p) + \alpha_{1a}' \quad (\text{IV.8})$$

where $A_T \sim R$, and α_{1a}' is another constant. At large radii, the R component of the $V(R)$ term in the SFE_a expression is canceled by the R dependence of the total area term A_T . Thus the model predicts that $\langle \text{SFE}(R) \rangle$ should fall-off with radius as $(\Omega(R) - \Omega_p)$. The particular form $(\Omega(R) - \Omega_p)$ for M51 is shown in Figure 8 (curves a, North and South), and is not evident in the observed $\langle \text{SFE}(R) \rangle$ function. An even steeper fall-off would be predicted had we not used the $A_{1a} \approx A_T$ approximation. Growth in $\langle \text{SFE}(R) \rangle$ with R could be produced using this model if A_a were to grow with radius. While GM define the arm location and width for the Milky Way in their model as a narrow ridge line of radio continuum emission, we might alter the definition to correspond to the arm width indicated by other tracers. Schweizer (1976) has measured arm widths for M51 in the U, B, and O bands as a function of radius. The results show a relatively constant width out to $R=215''$. However, if $H\alpha$ widths are used, then the bright Northeast HII complex does show a greater arm

width at $R=135''$ than that seen at interior radii. This radius is slightly beyond the corotation radius, and here the simple density wave picture is incomplete in accounting for the higher SFRs and SFEs observed.

ii) A Model Dependent on the Pressure of the ISM

In a different approach, Dopita (1985) suggests that star formation within a galactic disk is accompanied by events such as massive outflows and supernovae which serve to pressurize the ISM and induce further star formation (c.f. Seiden and Gerola 1979). In this picture, by measuring the pressure of the ISM, we can indirectly infer the current MSFR. Under the assumptions of z -distributions in stars and gas which follow a Gaussian form near the disk, and an exponential form at large distances, the z -velocity of the gas may be related to the total galaxy potential and scale height. By breaking the pressure term into the product of the gas density and the mean squared z -velocity of the gas and then solving for these quantities in terms of the total and stellar surface densities, an indirect measure of the SFR is obtained. The pressure term is found to be proportional to $\sigma_p \sigma_T$, where σ_T is the surface density in stars, gas and dark matter, and σ_p is our usual expression for the gas surface density. The pressure implies a SFR given by: $SFR = C \sigma_p \sigma_T z_0$, with C a constant and z_0 the scale height of ". . . the newly formed stars . . . [and] the parent clouds" (Dopita 1985). If we assume that z_0 does not vary appreciable with R (an assumption which is good to 30% for $R \sim 4 - 10$ kpc in the

Milky Way, Sanders 1981), then Dopita's law of star formation becomes $SFE(R) \sim \sigma_T(R)$ in a disk where new star formation is the dominant contributor to the pressure.

We compare this functional form in Figure 8 (curve b) to our observed $\langle SFE(R) \rangle$ and again find little adherence. We note that regions of massive star formation on the spiral arms probably do manifest a higher gas scale height, in both the H_2 and HI clouds, but this is an effect well beyond our means to detect. It is worth noting, however, that if the rising $z_{1/2}(R)$ function of Sanders (1981) for GMCs in the Milky Way were arbitrarily inserted into the SFR dependence equation for M51, this would not reverse the downward $\langle SFE(R) \rangle$ trend given by $\sigma_T(R)$ in curve b. Finally, we have not attempted to incorporate detailed $\sigma_T(R, \theta)$ variations which might be obtained from the 1 micron observations of Jensen (1977). For these reasons, we can not make a serious claim to have tested the Dopita (1985) model on a detailed level.

d) A Linear Model with a Constant Star Formation Efficiency in Time

The inverse of the SFE is the time period for the total depletion of the local gas in the absence of gas recycling from stellar outflows and if a constant SFR is maintained, i.e. SFR independent of ρ_p . If recycling is considered, with a fraction f of new stellar mass being constantly returned to the ISM, the timescale becomes $(1-f)^{-1} SFE^{-1}$. The second assumption, that the SFR is independent of ρ_p , does not seem

to be a very realistic one. The consequence of such an assumption is that most disk galaxies will consume their entire gas supplies in about 4 Gyr (Kennicutt 1983), which places us in an suspiciously privileged epoch. For example, selecting f between 0.2 and 0.3 gives time scales for the azimuthal averages in M51 between 2.8 and 3.6 Gyr, presumably a fraction of the galaxy's age. A more reasonable assumption is that the galaxy's SFR changes in time.

In §IIIb we have shown that azimuthal averages in the disk yield a linear proportionality between $\langle q_p \rangle$ and the $\langle \text{SFR} \rangle$ of $\text{SFE} = 0.4 \pm 0.1 \text{ Gyr}^{-1}$, while $\langle q_p \rangle$ varies with radius by a factor of 5. We postulate that this relatively constant SFE reflects an overall control of the total gas present in an annulus to limit the total SFR in a linear manner, even while arm and interarm regions are utilizing the gas resource with different efficiencies. The imposition of this linear relationship allows us to use the general treatment of Talbot (1980) as follows. We relate the observed SFR to the disk density by

$$(1-f) \text{SFR}(t) = \sigma'_*(t) = -\sigma'_p(t) \quad (\text{IV.9})$$

where the primes indicate time derivatives and SFR is the observed quantity, which includes mass yet to be recycled. In this sense, $\sigma'_*(t)$ is the net rate of change of stellar surface density (fraction locked up) and $\sigma'_p(t)$ is the net rate of change of gas surface density. The linear relation then gives

$$\text{SFR}(t) = \text{SFE}_e \sigma'_p(t) \quad (\text{IV.10})$$

or, equivalently,

$$\sigma'_p(t) = -(1-f) \text{SFE}_e \alpha_p(t) \quad (\text{IV.11})$$

with SFE_e , the empirical star formation efficiency, a constant in time. This differential equation has as its solution,

$$\alpha_p(t) = \alpha_p(0) \exp \{-(1-f) \text{SFE}_e t\}. \quad (\text{IV.12})$$

Thus, $(1-f) \text{SFE}$ is the inverse scale time for a nucleon to remain in the gas phase. If this relationship holds back in time to $t=0$ in the disk, we can use the current total (stars and gas) density to obtain an empirical efficiency estimate, SFE_e . Setting $\alpha_p(0)$ to the total local density, $\alpha_p(0) = \sigma_T = \alpha_p(t) + \alpha_*(t)$ in the expression above gives

$$\text{SFE}_e = [T(1-f)]^{-1} \ln[\sigma_T/\alpha_p(T)] \quad (\text{IV.13})$$

where T is the age of the galaxy, and σ_T may be obtained from mass models derived from the galaxy's rotation curve. Total masses and surface densities derived in this way are somewhat model dependent. For M51, the total mass estimate, M_T , ranges from $M_T=7.7 \times 10^{10} M_\odot$ for $R < 155''$ (Tully 1974, scaling $\sigma_T(R)$ to $D=9.6$ Mpc), to $M_T = 10 \times 10^{10} M_\odot$ (SY) for $R < 215''$. Inserting minimum and maximum estimates for $f = 0.2 - 0.3$ (Tinsley 1980; Talbot 1980), $T = 10 - 15$ Gyr, the α_p results from the individual annuli of Table 3a, and σ_T from Tully (1974), we find $\langle \text{SFE}_e \rangle = 0.16 - 0.23 \text{ Gyr}^{-1}$ over the entire disk. Thus, the time averaged star formation efficiencies are uniformly lower than

the values obtained using the $H\alpha$ flux measurements which gave $\langle SFE \rangle = 0.4 \pm 0.1 \text{ Gyr}^{-1}$. We have plotted $\langle SFE_e \rangle$ for a representative case in Figure 8.

A similar discrepancy, in the same absolute sense, between the estimated and observed efficiencies have been noted for the Milky Way and M83 (Talbot 1980; Larson 1986). Because the SFE is obtained solely through measurements of the current high mass stars, and SFE_e through the low mass stars dominating σ_T , explanations for the observed discrepancy alternatively involve different sorts of IMFs or $SFR(t)$ for the two populations of stars. Specifically, Larson (1986) postulates different decay time scales for the two SFRs, as well as a non-monotonic IMF for stars of $M < 2 M_\odot$, while Talbot (1980) and Jensen, Talbot, Dufour (1981) suggest an IMF biased toward but truncated at the high mass end, and spatially distinct birthsites for the high and low mass stars. Alternatively, Silk (1986) suggests a feedback process in which the star formation in molecular clouds heats the clouds and provides a low mass cutoff to the IMF as high as $10 M_\odot$ due to the increased critical mass necessary for fragment collapse. Finally, Talbot (1980) points out that gas infall during the lifetime of a galaxy will simulate a lower SFE_e , as compared to the observed SFE. In Appendix B we have investigated this possibility for M51. We have derived the necessary infall rates over the lifetime of the galaxy required to put our SFE and SFE_e estimates into accord. The result is that about 1/3 to 1/2 of the current galaxy mass would have had to

originate from constant infall. Such reserves of gas are not to be seen in the vicinity of M51, and, assuming the infalling material is gaseous, we have ruled out this possibility for M51.

e) The Region R=130"

We now turn our attention to the region at $R \approx 124''-135''$, where the SFRs and SFEs seem anomalously high as compared to the inner disk. This region must be viewed in the context of the spiral density wave and the tidal interaction .

A pattern speed, $\Omega_p = 37 \text{ km s}^{-1} \text{ kpc}^{-1}$, and corotation radius ($\Omega_p = \Omega(R_{\text{gal}})$) at $R_{\text{gal}} = 124''$ were obtained by Tully (1974c) by fitting the observed radial streaming motions to the linear density wave theory. At $R_{\text{gal}} = 124''$ the effects of corotation become apparent. The arms no longer open logarithmically, but suffer spatial distortions (discussed in §Vb). Furthermore, at this radius the Northeast and Southwest arms broaden in H α emission, and the dust lanes and radio continuum ridges which serve to demarcate the inner arm edge at radii outward from $R = 20''$ lose their definition. While some density wave models predict that the corotation region should display a gap or paucity of gaseous material (e.g. Schommer and Sullivan 1976, and references therein), a recent study contradicts this expectation. In a detailed 2-dimensional simulation using a powerful array processor, Nelson, Johns and Tosa (1985) studied a spiral potential much like that of M51 (20% potential and 20° pitch angle). They found that such a gaseous disk maintains a

sharp arm overdensity through corotation, while the spiral shock front crosses over to the leading outer arm edge beyond this radius. This results provides the possibility that the high efficiency at the Northeast and Southwest regions can be ascribed to the SDW.

In fact, it is in this region that the SDW and the tidal interaction with the companion are most linked. Julian and Toomre (1966) have shown that a non-axisymmetric force (i.e. the gravitational attraction from a nearby accreted clump of matter such as a satellite galaxy), acting upon a disk galaxy, will induce a spiral density wave that will establish itself in the outer disk and propagate inward. This wave will propagate through the disk on the time scale of a few epicyclic periods (Toomre 1969) which for M51 is 10^7 - 10^8 yr (Tully 1974c). The close passage of NGC 5195 each 5.3×10^9 yr (Toomre and Toomre 1972, scaled to $D=9.6$ Mpc) will provide just such an impetus to M51. A second effect of the tidal interaction is the transformation of outer circular orbits into oval orbits and more highly distorted forms. In the next chapter we will see that our outer disk observations kinematically verify the tidal model of Toomre and Toomre (1972). The great relevance of the tidal disruption is that converging streamlines are predicted to occur for the disturbed orbits which will increase N_c and σ_v , and therefore the collision rate, where the orbits crowd or cross. These effects are present in the Northeast and Southwest just where we see the exceptionally bright HII regions at $R_{\text{sky}}=135''$, $\theta_{\text{sky}}=45^\circ, 135^\circ$. In the Southwest, test particles (e.g. molecular

clouds) in the tidal disruption model cross at 30° angles, which can raise the collision probability for an individual cloud to near unity.

As has been pointed out by many authors, theory indicates that spiral density waves tend to be dissipative, i.e., they damp out in time. This is especially true if a galaxy possesses an inner Lindblad resonance (ILR), because the ILR serves to feed energy into randomizing stellar motions at this radius, which in turn damps out the spiral perturbation (Kormendy and Norman 1979, and references therein). For the flat rotation curve of M51, an ILR is present for $\Omega_p < 42 \text{ km s}^{-1} \text{ kpc}^{-1}$. The modeled $\Omega_p = 37 \text{ km s}^{-1} \text{ kpc}^{-1}$ (Tully 1974c, scaled to 9.6 Mpc) puts the ILR at $R=25''$, which is in fact the radius where spiral structure terminates. Thus, M51's SDW is especially prone to dissipation. The implications are that the sharply delineated spiral structure we now see in this galaxy may be ephemeral, existing only a short time ($\sim 10^8 \text{ yr}$) during each close passage of the companion, about once each $5.3 \times 10^9 \text{ yr}$. It may be that the galaxy is now experiencing more rapid and efficient star formation due to the present close passage. This would tend to explain why the observed present SFE is significantly larger than the past average SFE_e . It would not, however explain why the SFE_e values for the Milky Way and M83 are less than the present value, because these galaxies have not been recently subjected to any obviously perturbing encounters, although passages in the past between the Milky Way and the LMC may be important (Toomre 1969).

CHAPTER V

KINEMATIC DEPARTURES IN THE FAR NORTH

In this chapter we describe our observations of the far northern ($R=247''$) tidal arm of M51 (§Va and b). We show that the kinematic perturbations which have been found in the H α and HI distributions in this region have now been recorded in CO emission as well (§Vc). This result is important because it gives further evidence of the strong influence that the companion galaxy, NGC 5195, has on the stellar and cloud orbits in M51's disk (§Vd). The interaction is of special relevance to our study because orbital crowding in the Northeast and Southwest (at $R\sim 135''$) could be the dominant cause of cloud collisions and thus of massive star formation, rather than the spiral density wave. The current tidal model, however, is not without its difficulties (§Ve).

a) The Observations

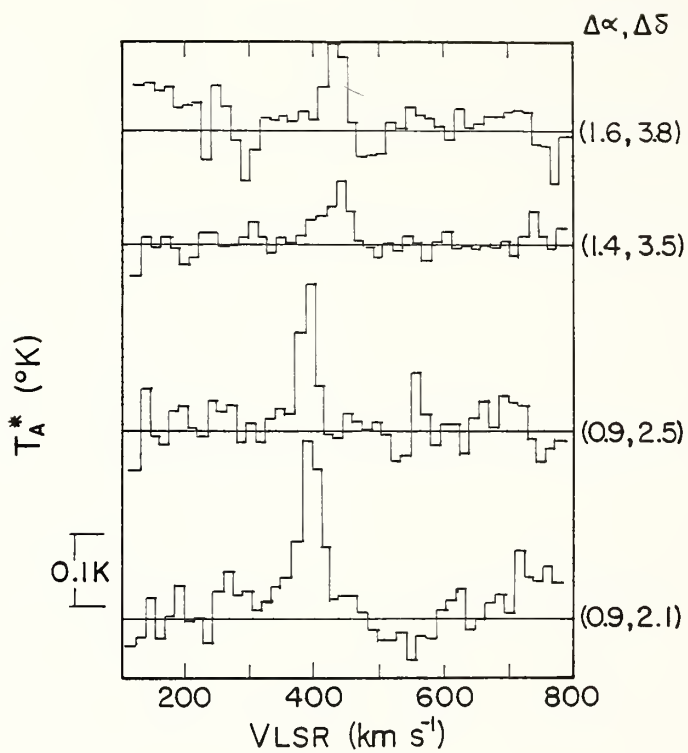
Our observations of the outer disk of M51 have included 12 detections of CO emission in selected regions along the North and South optical arms. Here we present results on the emission in the region at $R_{\text{sky}} = 247''$, $\theta_{\text{sky}} = 22.5^\circ$, where the northern "tidal arm" crosses in front of the western portion of the companion galaxy NGC 5195. The positions which we term A and B are shown superposed on the H α image in Figure 1 and are situated along M51's far northern arm near where the companion's nucleus appears as a white oval. The spectral line profiles at A and B are displayed as the upper two profiles in Figure

9. The two lower spectra in this figure were taken along the same position angle as A and B but at substantially smaller radii, $R_{\text{sky}} = 158''$, and $R_{\text{sky}} = 137''$ and we denote these as C and 43 (of Table 1) respectively. All four positions lie along a line of P.A. = $22.5 \pm 3^\circ$.

b) Star Formation Rates

We have estimated the N_{H_2} , N_p , SFRs and SFEs for positions A and B using our molecular observations, the PDS image and the HI results of Weliachew and Gottesman (1972). While the H_2 density is seen to be low at these positions as compared with the inner disk values, we note that the values ($N_p \approx 26 \times 10^{20} \text{ cm}^{-2}$) are greater than expected than if the molecular disk falls off exponentially with the scale length of 4.3 kpc found by SY, (which would predict $N_p = 11 \times 10^{20} \text{ cm}^{-2}$). These densities at $R=250''$ are comparable to densities found at radii 100" inward. Therefore, at least in the North, with our scant sampling, the outer molecular disk emission from $R = 135''$ to $R = 230''$ appears to show little variation. Within this same radial extent, Weliachew and Gottesman see the HI emission fall off, yet at positions A and B, the HI component accounts for as much as 1/3 the total N_p . Likewise, the SFRs at positions A and B are low as compared with the mean inner disk values (Table 3), yet comparable to the interarm values in the outer annulus at $R_{\text{sky}} = 135''$. We credit these low SFR values to the extreme narrowness of the $\text{H}\alpha$ emission in the tidal arm; the width here is only 5-10", versus the 40" wide complex in the Northeast at $R_{\text{gal}} = 135''$, which is more commensurate with our resolution (especially at position

Figure 9. Four CO spectra taken along $\theta_{\text{sky}} = 23^\circ$. The top two spectra lie on the far northern tidal arm, $58''$ from the companion galaxy, and show a velocity reversal 70 km s^{-1} redshifted from M51's nominal rotation curve. The effect is due to tidal forces.



C). The SFEs found for regions A and B are within one standard deviation of the mean value found within the outer annulus. Observational parameters for the CO spectra, SFRs, and SFEs and are given in Table 8. Insufficient coverage of the outer disk CO emission precludes our making any conclusions regarding the role of spiral structure in influencing the SFRs and SFEs in this region.

c) Far North Velocity Reversal

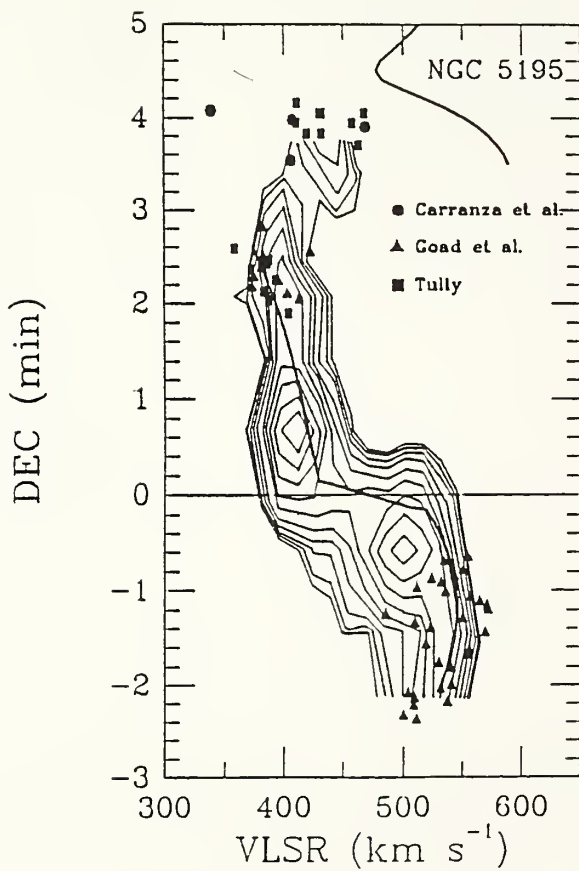
As can be seen at the top of Figure 9, the line center velocities show a dramatic change from 390 km s^{-1} to 440 km s^{-1} moving outward along $\theta_{\text{sky}} = 22^\circ$ from positions C to B. The velocity shift is in the direction opposite that expected from the galaxy's rotation curve. The measured H α velocities of NGC 5194 measured from slit spectra (Goad, de Veny and Goad 1979, henceforth GDG) show a strongly rising rotation curve in the northern half of the galaxy out to $R=2.8'$. But in the particular region of positions A and B, a velocity reversal of 50-100 km s^{-1} is apparent, seen clearly in our spectra and in the H α Fabry-Perot interferometry results of Tully (1974b,c) and Carranza, Crillon and Monnet (1969). A comparison of the molecular and ionized gas velocities along the vector $\theta_{\text{sky}} = 22^\circ$ extending North and South is shown in Figure 10, where the H α velocities are drawn from the sources above. The lower dark line in this figure ($\Delta\delta = -2.2 -2.8'$) is the GDG fit to the galaxy's rotation curve projected onto the sky, while the upper dark line ($\Delta\delta = 3.4 -5.0'$) represents sky velocities expected for the companion NGC 5195.

TABLE 8

KINEMATIC AND DERIVED PARAMETERS FOR POSITIONS ALONG $\Theta_{\text{sky}} = 22^\circ$

Index	R_{sky} (sec)	Θ_{sky} (deg)	V_{peak} (km s^{-1})	V_{mean} (km s^{-1})	ΔV_{FWHM} (km s^{-1})	$N_{\text{p}}(\text{H}_2)$ (10^{20} cm^{-2})	$N_{\text{p}}(\text{HI})$ (10^{20} cm^{-2})	SFR ($M_{\odot} \text{ pc}^{-2} \text{ Gyr}^{-1}$)	SFE (Gyr^{-1})
A	247	22.5	440	450	40	27	7	2.4	0.09
B	225	22.6	460	440	70	22	8	1.7	0.07
C	154	20.6	400	390	35	27	8	61	2.2
43	135	22.5	400	410	40	71	11	77	1.2

Figure 10. The spatial-velocity diagram for eight positions along the $\theta_{\text{sky}}=23^\circ$ diameter through the disk. The velocity reversal in the north tidal arm is seen above $\Delta\delta=3.5'$. The heavy lines show the projected, three component rotation curve for M51 (of GDG) and that of NGC5195 (from Schweizer 1977). Also displayed are the detailed H α velocities along this diameter, suggestive of a systematic velocity shift between the molecular and ionized gas at $\Delta\delta = 2.4'$ and $-1.5'$ (but see §Va).



Since position A is located just 58" from the center of the companion NGC 5195, an SB(pec) galaxy, it is important to us to show that the CO emission we see at positions A and B originate from the main galaxy and not the companion. We have shown this by extrapolating Schweizer's (1977) rotation curve for NGC 5195. The NGC 5195 rotation curve gives apparent velocities for the companion 100 km s^{-1} greater than those observed in CO emission at positions A and B. This may be seen at the top of Figure 10, where the sinusoidal curve represents NGC 5195's rotation velocity projected onto the sky along the radius vector $\theta_{\text{sky}} = 22^\circ$ emanating from NGC 5194. Because of projection effects which depend both on the companion's inclination and the azimuth angles made by positions A and B, circular velocities five times in excess of those seen by Schweizer would be required to ascribe the gas velocities seen in the CO emission at these locations to NGC 5195. Furthermore, we have seen no evidence for molecular emission at the anticipated velocity $v_{\text{LSR}} = 580 \text{ km s}^{-1}$ in our spectra, nor did SY find emission at the center of the companion ($v_{\text{sys}} = 597 \text{ km s}^{-1}$), down to a 3σ level of 1.5 K km s^{-1} . The CO emission therefore appears to originate from M51 itself and we conclude that the velocity perturbations in the tidal arm which have heretofore only been seen in H α (Tully 1974c) and HI (Weiliachew and Gottesman 1973; Rots 1985, personal communication) have now been detected in CO emission as well.

In Figure 10 we also see that in the North, from $\Delta\delta = 1.8'$ to $2.8'$, and in the South, from $\Delta\delta = -0.2'$ to $-1.5'$, there appear to be

systematic 25 km s^{-1} departures from the mean ionized and molecular gas velocities, in the sense that the ionized gas is "rotating faster" than the molecular gas. Similar conclusions were reached by Rydbeck, Hjalmarson and Rydbeck 1984, who found a velocity difference in the same sense of 40 km s^{-1} along a nearby position angle. A more careful analysis of the observational data shows that both of these values are in fact overestimates of any velocity difference between the ionized and molecular gas and are caused by the incompatible resolutions employed in the comparisons. The narrow $\text{H}\alpha$ slit spectra taken near the major axis in each case, perforce, record the very highest projected velocities of the galaxy. The broader resolution CO beams in each case are biased toward lower velocity emission from the inner radii and the $20\text{-}30 \text{ km s}^{-1}$ lower velocity emission which is prevalent $20''$ to either side of the major axis (Tully 1974a). Such additional velocity information must be employed to make a fair comparison with the CO data. To test for a systematic velocity difference, we have constructed synthetic $\text{H}\alpha$ line profiles at the same resolution as our CO data for the inner galaxy using Tully's velocity field and a modeled exponential CO distribution. In these spectra we find that at no position is the $\text{H}\alpha$ velocity peak displaced from the CO velocity peak by more than 10 km s^{-1} , which is our resolution limit.

d) The Tidal Encounter Model

In an attempt to match certain observed morphological and kinematic attributes of the NGC 5194/5195 system, Toomre and Toomre

(1972) conducted a series of tidal encounter simulations, arriving at an orbit for the companion with a closest approach of 13 kpc occurring 10^8 years ago, an eccentricity of $e = 0.8$, a relative inclination of 70° , and a mass for the companion equal to $1/3$ the mass of the main galaxy. The model replicates a host of observed features (see Tully 1974c, for a review); most notable are the broad Southern arm, the inward deformity and sharp outer edge cutoff of the Northwest arm, and the formation of the narrow tidal arm. Furthermore, the model made specific predictions which have been borne out by subsequent observations, including the relative mass of the two systems, the sense of the companion's rotation (approaching in the West) and the gross kinematics of the tidal arm. The 70 km s^{-1} velocity reversal at position A is the combined result of z-motions and departures from circular rotation due to the tidal forces brought on by the companion as it traveled over the Northwest quadrant of M51 about 10^8 years ago. What makes the model so remarkable is the motion of test particles outward of $R = 2.5'$ from NGC 5194's center. These particles travel in ellipses for the majority of their orbits, but leave these elliptical paths in the Northeast and Southwest. In the Northeast, the test particles travel to the outer disk in a trajectory that takes them along elongated closed loops, first up the leading edge of the tidal arm and then back down the trailing edge, crossing their own paths to resume their counter-clockwise circuit about the center. A range of velocity departures from circular rotation results, with a maximum line-of-sight value of -100 km s^{-1} predicted for particles along the

inner edge of the tidal arm. Such a velocity spread is seen in the molecular and H α data shown in Figure 11, although even with 6.75" resolution, Tully was unable to isolate the lowest velocity inner arm streamlines.

A second effect of the tidal model, bearing directly on our results, is the predicted crowding of tidally-invoked elliptical orbits at R=135" in the Northeast and Southwest. The encounter model shows streamlines bunching together precisely where the two giant HII complexes (and the molecular emission peaks) are seen in the outer annulus. The hypothesis has been advanced by Tully (1974c) that these two regions (at $\theta_{\text{sky}} \approx 45^\circ$ and 235°) mark both the termini of the spiral density wave and material clumping due to the crowded streamlines. The effect of the tidal force is thought to become insignificantly weak interior to this radius, and the gas motions therein are dominated by the potential of the interior mass.

At R=135" where the tidal force is strong, the density wave is beyond its corotation radius. With the pattern speed fit by Tully, $\Omega_p = 37 \text{ km s}^{-1} \text{ kpc}^{-1}$ (scaled to D=9.6 Mpc), the corotation occurs at R=124". Tully points out that at the Northeast giant HII complex, classical indicators of a spiral density wave are missing. Absent are both a sharp radio continuum gradient along the inner arm edge (cf. Klein et al. 1986) and a well defined inner dust lane, features which are common to most of the interior spiral pattern. For these reasons we must regard the two arm-related peaks in the spiral phase diagram

for this radius bin (Figure 7c-f) possibly as the result of tidal clumping. It is of little comfort to point out that the fortuitous superposition the SDW and tidal crowding mechanisms at $R=135$ and $\theta_{\text{sky}} \approx 45^\circ$ and 235° cannot be maintained in-phase for very long; in a few $\times 10^8$ yr they will appear at spatially distinct locations, with the orbital crowding leading the spiral pattern counterclockwise around the galaxy.

e) Problems with the Model

The Toomres' model, while scoring many successes for this system, is now due for revision in light of both new observational data and the advent of more modern computer simulation capabilities. Self gravity of the mass tracers is ignored in their simulations and the authors point out "self gravity may tend to aggravate tidal damage". Furthermore, newly observed features exist which are definitely not included in the model's predictions. Recent unpublished 21-cm interferometric observations of Rots show an HI arm extending from the broad Southern optical arm and curving continuously north to a position over $20'$ (55 kpc!) northeast of the center. Seen also are several highly redshifted debris-like clouds at a comparable distance to the North. Such remnants may be the witnesses of a far more violent interaction than the one advanced by the Toomres. An inspection of the Toomres' (1972) catalog of galaxy-galaxy encounters leads one to opt for a more head-on collision than the current grazing approach, or a succession of such events to explain these features. The difficult

goal of such a simulation is to reproduce the newly observed features without doing violence to the existing, observationally verified ones. Self gravity may help in such a venture by allowing for the observed self-containment of the northern HI arm in the presence of a more violent encounter.

The correct portrayal of the tidal forces operating on M51's disk is essential in learning about the role played by the molecular clouds in forming stars. Even as the model now stands, point masses, and thus possibly molecular clouds, move radially outward from $R=150''$ to $R=250''$, stall to near zero velocity in a clumped distribution in the tidal arm, and then somehow cross back through their own streamlines to return to the inner radius. While stars may be able to accomplish such a feat without collisions, clouds cannot. A simple calculation using typical GMC parameters from Sanders, Scoville and Solomon (1985), in conjunction with our outer disk N_p estimates, give a cloud surface filling factor of $f_s \approx 0.04$ at the crossing point. The resulting mean cloud separation of 125 pc implies that crossing molecular cloud streams, with velocities given by the model, will collisionally damp out in less than 10^6 years. A somewhat fanciful way out of this dilemma would be to have the outgoing and incoming streams isolated at different z heights, i.e. a three dimensional loop structure, which might be a conceivable ramification of the non-coplanar encounter of the two galaxies.

Without the means for steady state transport, it remains an open question if the molecular emission seen at $R=250''$ is from molecular

clouds brought there by tidal forces operating on the outer disk, or else from clouds formed in situ by a corresponding clumping of the HI, subjected to the same velocity stalling as the test masses. To determine the molecular cloud motions occurring between $R=150''$ and $R=250''$, higher resolution molecular studies are needed. Our few observations in the outer disk suggest that the cloud population may be sufficiently pervasive and emissive as to allow for the acquisition of detailed velocities in the disrupted regions, especially at locations where $H\alpha$ emission is spotty or entirely absent. The fact that the companion has little or no emission down to the 1.5 K km s^{-1} level might aid in sorting out the distortions suffered by NGC 5194 in the encounter.

CHAPTER VI

CONCLUSIONS

a) Gas Densities and Star Forming Rates in Individual Locations, and in Azimuthal Averages

1) An immediate conclusion of this work is that the star formation rates and the gas densities are generally correlated in that the two distributions fall off together in radius, but there is a lack of strict correlation in the point to point comparisons when regions 2.1 kpc in diameter are considered. In the inner disk, the HII regions, and thus the regions with high star formation rates are found predominantly on spiral arms, while the interstellar gas, consisting mostly of molecular hydrogen, appears more uniformly distributed.

2) We find 40% variations in gas density and over 100% variations in SFR at any radius in the inner disk. While the SFR variations occur mainly on the spiral arms (as inferred from the H α flux), the variations in the gas density (as inferred from I_{CO} measurements) occur throughout the disk.

3) Because the gas density and star formation rates falloff in a similar manner with radius, a fairly constant $\langle \text{SFE} \rangle = 0.4 \pm 0.1 \text{ Gyr}^{-1}$ is obtained at all radii.

4) The azimuthally averaged $\langle \text{SFE}(R) \rangle$ function shows its highest values near the nucleus and at a radius of $R \approx 135''$. This function does not follow a $(\Omega(R) - \Omega_p)$ proportionality nor a $\sigma_T(R)$ proportionality as

suggested by Gusten and Mezger (1982) and Dopita (1985) in their models of star formation in galactic disks.

5) Efficiency measurements based on the density of gas and low mass stars in the present epoch, $\langle \text{SFE}_e \rangle$, and representative of the time-averaged SFE in the disk over the galaxy's lifetime, is smaller by a factor of 0.6 than the current SFE as estimated by the H α flux and the gas density. This discrepancy suggests the galaxy is currently undergoing star formation with an efficiency higher than that averaged over its lifetime. Such events may be linked to the passage(s) of the companion galaxy, NGC 5195. Of the alternative explanations for this discrepancy between SFE_e and SFE, the possibility of mass infall has been ruled out, while the possibility of an incorrect extrapolation from a high mass star formation rate total star formation rate has not.

b) Spiral Structure

1) The molecular spiral pattern is revealed by averaging the observations in the coordinate system of the pattern. With a resulting resolution of 50"-70" in this frame, the intrinsic variations in the molecular distribution are smoothed-out and the arms stand out as a 20-55% enhancement in gas surface density, as compared to the 100% to 400% seen enhancements seen in the H α distribution.

2) The SFR can be modeled as a function of gas density, with higher star formation efficiency, SFR/σ_p apparent on the spiral arms. The arm efficiency is consistent with, but not uniquely selected by, a

quadratic or higher power law relation between the spiral arm gas density and SFR. High arm efficiencies are most pronounced in the region $113'' < R_{\text{gal}} < 158''$ where the on-arm efficiency is seen to be nearly twice the interarm efficiency. This result lends support to the idea of massive star formation through cloud-cloud collisions on the spiral arms. Cloud orbits are crowded together due to the compressive action of the spiral density wave, and, outside the corotation radius at $R=124''$, by the tidal distortions caused by the close passage of the companion galaxy.

3) Despite the high efficiency on the arms, azimuthal means show a relatively constant star formation efficiency over the disk, implying that the total star formation in an annulus is governed by the total gas density. We ascribe a role to the spiral density wave of localizing star formation, rather than globally raising the total rate.

c) Kinematics

We have detected the North tidal arm ($R=248''$) in CO emission. The gas velocities display the 50 km s^{-1} drop from the flat rotation curve as predicted from Toomre and Toomre (1972).

CHAPTER VII

OBSERVATIONS OF M83

a) Introduction

The bright Southern galaxy M83 (NGC 5236 SAB(s) I-II) in Hydra is one of the most luminous galaxies known in molecular emission ($I_{\text{CO}} = 59 \text{ K } [T_{\text{R}}^*] \text{ km s}^{-1}$ in the inner 2 kpc) and is also the nearest of the barred spiral galaxies. With its large angular size (Holmberg diameter $d=16.2'$), its massive and extended bar, bright HII regions, and clearly defined global spiral structure, it poses as an ideal testing ground for current models of gas dynamics and star formation in this class of galaxies. Here we present new CO (J=1-0) observations of the central 300" (with HPBW=45") and use these results to show how the molecular gas component of the inner disk mimics the bar morphology. The derived molecular gas distribution is then used in combination with HI and H α images of this galaxy, which were obtained from the literature, to determine the dependency of the massive star formation rate on the total gas density at each position. A linear relationship results. We discuss the implications this has regarding the evolution of the disk, and compare our results to an earlier study of M83 (Jensen, Talbot, and Dufour 1981, henceforth JTD) in which estimates of the star formation rates in M83 were derived in several different ways.

In the following sections we will discuss the acquisition and calibration of the observational data sets and give the conversion factors used to obtain star formation rates and total gas densities

(§VIIb,c,d). In §VIIIa,b, we present the data in point by point comparisons and in two different averaging schemes which will display the star formation characteristics with radius and azimuth in the inner disk, $R_{\text{gal}} < 150''$. Finally, in §VIII.c,d, we impose the assumption of a linear relation over time between the star formation and the gas density, which enables us to draw conclusions regarding the star forming history of the galaxy and the validity of the IMF employed. The casual reader may at this point wish to pass over the calibration discussion below and turn directly to the results which begin at §VIII.

b) CO Observations

Millimeter observations of M83 were conducted between November 1984 and June 1985 using the 13.7 m telescope of the Five College Radio Astronomy Observatory. At the 115 GHz transition of CO (J=1-0) the antenna has a HPBW=45" which subtends 1.9 kpc on the galaxy at the adopted distance, $D=8.9$ Mpc (see Table 9). The cooled mixer receiver ($T_{\text{SSB}}=200$ K) typically obtained system temperatures of 900 K at el.= 60° and 1800-3000 K at el.= 16°-18°, where the transit elevation of M83 is 18°. The filterbank employed was 256 channels by 1 MHz yielding a velocity resolution 2.6 km s^{-1} which was subsequently smoothed to 12 km s^{-1} in the data reduction process. Reference spectra were subtracted in a double position switching mode using 10' offsets in RA, with 30 s integration times. The total integration time per position was 3 hr, producing rms noise of $T_A^*(\text{rms})= 0.05-0.10 \text{ K}$ at 12 km s^{-1} resolution, after atmospheric corrections were applied, as described below.

TABLE 9 (NOTES)

(1) Rumstay and Kaufman (1983). All offsets in this work refer to this central position.

(2) de Vaucouleurs et al. (1976, RC2). This position provided the original center for the CO map of this study.

(3) Ondrechen (1985). M_{HI} is derived by us from Ondrechen (1985, Figure B12).

(4) Sandage and Tammann (1975).

(5) de Vaucouleurs et al. (1983).

(6) Talbot, Jensen, and Dufour (1979).

(7) This work.

(8) Young, et al. (1987).

TABLE 9
GLOBAL PARAMETERS FOR M83 (NGC 5236)

Parameter	Value	Reference
Type:	SAB(s)c I-II	(5)
Center Position:		
R.A. (1950)	13 ^h 34 ^m 11 ^s .55	adopted (1)
Dec.	-29° 36' 42".2	value
R.A.	13 34 10.2	(2)
Dec.	-29 36 48	
R.A.	13 34 11.1	(3)
Dec.	-29 36 34.6	
Inclination	26 ± 6°	adopted value (2)
Major Axis Position Angle	46 ± 4°	adopted value (2)
Distance, D	8.9 Mpc	adopted value (4)
	3.7 Mpc	(5)
V _{sys} , w.r.t the LSR (V _{LSR} -V ₀ =1.92 km s ⁻¹)	511 km s ⁻¹	adopted value (5)
B Magnitude B _T ⁰ Corrected	8.24	(6)
log L _B (M ₀) at D=8.9 Mpc	10.95	(8)
log L _{IR} at D=8.9 Mpc	10.78	(8)
Corrected Isophotal Diameter D ₂₅	16.2'	(6)
M _{H2} within R _{gal} = 115"	15.6 × 10 ⁹ M ₀	(7)
M _{H I} within R _{gal} = 115"	1.9 × 10 ⁸ M ₀	(3)

Pointing and focus were determined during each transit using Saturn and IRC+10216. The total pointing accuracy was 3" rms. The RC2 central position was used for the molecular observations, which is offset from the optical and radio HI centers (Table 9). The latter values are more nearly correct, and we refer all subsequent offsets in this paper to the central position used by Talbot, Jensen, and Dufour (1979, henceforth TJD) as later determined by Rumstay and Kaufman (1983). Table 9 also lists other relevant systemic parameters adopted in this study. For positional accuracy in the data presentation of Tables 10 and 11, we draw a distinction between the 45" beam centers and their radius centroids, that is, the mean radius averaged over the beam's point spread function.

The galaxy was sampled along 4 axes, 45° apart, going through the center, with the positions along each axis spaced by 1 HPBW. We detected CO emission in each of the 21 positions sampled. Figure 11 shows these positions overlayed on the $H\alpha$ map of the galaxy (TJD) and the CO observational results are shown in an integrated intensity map in Figure 12.

Calibration of the M83 CO observations required special care due to the extremely low elevation of the source. In the calibration process, the source elevation comes into play twice, once in correcting the chopper wheel calibration method (Penzias and Burrus 1973) for the temperature difference between the ambient lower atmospheric temperature, T_{amb} , and the upper atmospheric temperature, T_{atm} , (Davis

TABLE 10
OBSERVED AND CORRECTED PARAMETERS

ln	$\Delta\alpha$	$\Delta\delta$	R_{sky}	Θ_{sky}	R'_{gal}	R_{gal}	Θ_{gal}	I'_{CO}	η_c	$I_{CO} \pm \sigma_I$	$f'_{H\alpha}$	N	$f_{H\alpha} \pm \sigma_f$	f_{HI}		
(1)	(2)	(3)	(4)	(5)	(6)	(7)	(8)	(9)	(10)	(11)	(12)	(13)	(14)	(15)		
1	-18	-7	19	247	20	34	25	59	0.55	108.3	± 20.2	27.9	10	72.6 ± 6.9	0.13	
2	-18	38	42	335	46	51	108	19	0.60	31.0	5.8	13.5	2	34.5	7.3	0.13
3	14	24	28	30	28	39	163	33	0.58	56.5	10.5	22.4	10	57.6	5.5	0.46
4	27	-7	28	105	31	40	243	11	0.63	17.4	3.2	12.4	5	32.2	4.3	0.13
5	14	-39	42	160	46	51	293	10	0.64	16.1	3.0	9.6	4	24.4	3.7	0.21
6	-18	-52	55	199	57	61	331	15	0.61	24.9	4.6	8.9	4	21.8	3.3	0.37
7	-48	-39	63	232	63	67	8	16	0.63	25.6	4.8	9.4	4	22.1	3.3	0.17
8	-63	-7	63	263	66	70	42	6	0.68	8.8	1.6	6.4	1	15.2	4.5	0.21
9	-50	24	55	296	61	65	73	10	0.61	17.0	3.2	6.4	1	15.6	4.7	0.21
10	-18	83	85	348	92	94	120	6	0.67	9.5	1.8	4.0	1	9.0	2.7	0.76
11	46	56	73	39	73	76	174	25	0.58	42.4	7.9	15.7	8	36.3	3.9	0.46
12	72	-7	73	96	78	81	234	8	0.66	12.3	2.3	5.1	1	11.5	3.4	0.69
13	46	-71	85	147	95	96	281	17	0.57	30.1	5.6	2.6	1	5.8	1.7	0.13
14	-18	-97	99	190	103	115	322	5	0.68	7.7	1.4	5.2	1	11.3	3.4	0.59
15	-82	-71	108	229	108	110	4	29	0.56	52.1	9.7	24.1	10	51.2	4.9	0.97
16	-108	-7	108	266	114	116	44	18	0.60	29.6	5.5	15.0	3	31.6	5.5	1.16
17	-82	56	99	305	111	112	81	11	0.64	17.5	3.3	15.1	3	32.3	5.6	1.05
18	78	88	117	41	117	119	176	12	0.62	20.0	3.7	6.6	3	14.2	2.5	0.64
19	78	-103	129	143	144	146	277	4	0.64	6.8	1.3	4.0	2	8.2	1.7	0.63
20	-113	-103	153	228	153	155	3	10	0.64	14.9	2.8	8.1	2	15.9	3.4	1.15
21	-113	-88	144	308	161	162	84	11	0.61	17.9	3.3	13.2	4	26.1	3.9	0.74

TABLE 10
OBSERVED AND CORRECTED PARAMETERS

i_n	$\Delta\alpha$	$\Delta\delta$	R_{sky}	Θ_{sky}	R'_{gal}	R_{gal}	Θ_{gal}	I'_{CO}	η_c	$I_{CO} \pm \sigma_I$	f'_{Ha}	N	$f_{Ha} \pm \sigma_f$	f_{HI}		
(1)	(2)	(3)	(4)	(5)	(6)	(7)	(8)	(9)	(10)	(11)	(12)	(13)	(14)	(15)		
1	-18	-7	19	247	20	34	25	59	0.55	108.3 \pm 20.2	27.9	10	72.6 \pm 6.9	0.13		
2	-18	38	42	335	46	51	108	19	0.60	31.0	5.8	13.5	2	34.5	7.3	0.13
3	14	24	28	30	28	39	163	33	0.58	56.5	10.5	22.4	10	57.6	5.5	0.46
4	27	-7	28	105	31	40	243	11	0.63	17.4	3.2	12.4	5	32.2	4.3	0.13
5	14	-39	42	160	46	51	293	10	0.64	16.1	3.0	9.6	4	24.4	3.7	0.21
6	-18	-52	55	199	57	61	331	15	0.61	24.9	4.6	8.9	4	21.8	3.3	0.37
7	-48	-39	63	232	63	67	8	16	0.63	25.6	4.8	9.4	4	22.1	3.3	0.17
8	-63	-7	63	263	66	70	42	6	0.68	8.8	1.6	6.4	1	15.2	4.5	0.21
9	-50	24	55	296	61	65	73	10	0.61	17.0	3.2	6.4	1	15.6	4.7	0.21
10	-18	83	85	348	92	94	120	6	0.67	9.5	1.8	4.0	1	9.0	2.7	0.76
11	46	56	73	39	73	76	174	25	0.58	42.4	7.9	15.7	8	36.3	3.9	0.46
12	72	-7	73	96	78	81	234	8	0.66	12.3	2.3	5.1	1	11.5	3.4	0.69
13	46	-71	85	147	95	96	281	17	0.57	30.1	5.6	2.6	1	5.8	1.7	0.13
14	-18	-97	99	190	103	115	322	5	0.68	7.7	1.4	5.2	1	11.3	3.4	0.59
15	-82	-71	108	229	108	110	4	29	0.56	52.1	9.7	24.1	10	51.2	4.9	0.97
16	-108	-7	108	266	114	116	44	18	0.60	29.6	5.5	15.0	3	31.6	5.5	1.16
17	-82	56	99	305	111	112	81	11	0.64	17.5	3.3	15.1	3	32.3	5.6	1.05
18	78	88	117	41	117	119	176	12	0.62	20.0	3.7	6.6	3	14.2	2.5	0.64
19	78	-103	129	143	144	146	277	4	0.64	6.8	1.3	4.0	2	8.2	1.7	0.63
20	-113	-103	153	228	153	155	3	10	0.64	14.9	2.8	8.1	2	15.9	3.4	1.15
21	-113	-88	144	308	161	162	84	11	0.61	17.9	3.3	13.2	4	26.1	3.9	0.74

TABLE 11 (NOTES)

Column (1) Position index.

Columns (2 and 3) R_{sky} and θ_{sky} are the radius and position angle from North of the beam center locations measured in arc seconds and degrees respectively.

Column (4) R_{gal} is the beam-weighted mean radius of an observation.

Columns (5 and 6), R'_{gal} , θ_{gal} are the beam center locations in the plane of the galaxy in arc seconds and degrees from the principal axis ($\theta_{\text{sky}}=226^\circ$) respectively.

Columns (7 and 8) i_A and i_S are the radial annulus index, and the azimuthal sector index, used for the azimuthal and sector averaging of the various distributions.

Column (9), $N_p(\text{H}_2)$, molecular hydrogen plus He surface density. N_p (protons cm^{-2}) = $6 \times 10^{20} I_{\text{CO}} \cos(i)$. In this table, N_p is given in units of 10^{20} protons cm^{-2} .

Column (10) $N_p(\text{HI})$, neutral hydrogen surface density, given in 10^{20} protons cm^{-2} .

Column (11), Total gas number surface density in 10^{20} protons cm^{-2} , with error in N_p from α_I of Table 10.

Column (12), Star formation rate in $M_\odot \text{pc}^{-2} \text{Gyr}^{-1}$ from $f_{\text{H}\alpha}$ using the modified Miller-Scalo IMF; $\text{SFR} = C f_{\text{H}\alpha} \cos(i)$, where $C = 4.54 \times 10^{16} (M_\odot \text{pc}^{-2} \text{Gyr}^{-1}) / (\text{erg cm}^{-2} \text{s}^{-1} \text{arcsec}^{-2})$. The error term is from α_f of Table 10.

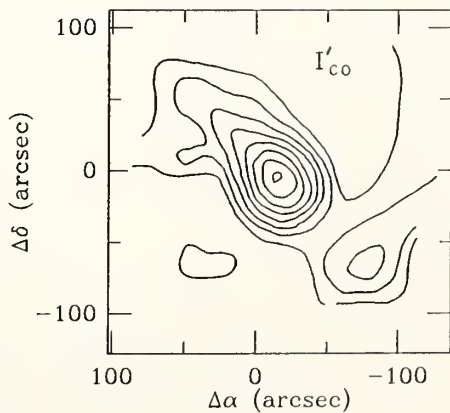
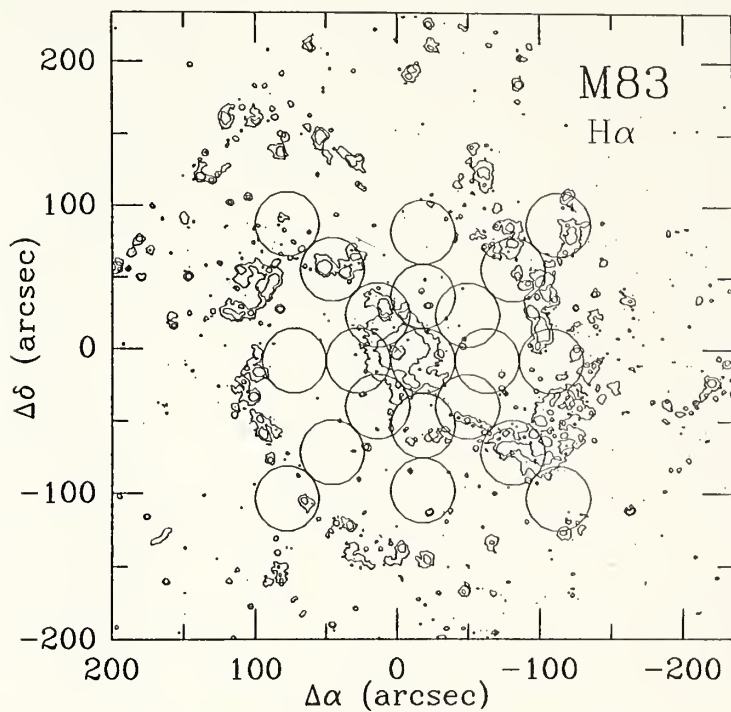
Column (13), $\text{SFE} (\text{Gyr}^{-1}) = \text{SFR} / \alpha_p$, where α_p is total gas mass surface density in $M_\odot \text{pc}^{-2}$ with formal error in SFE from α_R and α_N .

TABLE 11
DERIVED QUANTITIES

in.	R_{sky}	Θ_{sky}	R'_{gal}	R_{gal}	Θ_{gal}	i_A	i_S	N_{H_2}	N_{HI}	$N_p \pm \sigma_N$	$\text{SFR} \pm \sigma_R$	$\text{SFE} \pm \sigma_E$
(1)	(2)	(3)	(4)	(5)	(6)	(7)	(8)	(9)	(10)	(11)	(12)	(13)
1	19	247	20	34	25	1	-	650	1.0	586 ±121	311 ±30	0.67 ±0.15
2	42	335	46	51	108	2	1	186	1.0	168 36	148 31	1.10 0.31
3	28	30	28	39	163	2	2	339	3.7	308 63	247 23	1.00 0.22
4	28	105	31	40	243	2	3	104	1.0	95 19	138 19	1.82 0.44
5	42	160	46	51	293	2	4	97	1.6	88 18	105 16	1.49 0.37
6	55	199	57	61	331	2	5	150	2.9	138 28	93 14	0.86 0.21
7	63	232	63	67	8	2	6	154	1.3	140 29	95 14	0.86 0.21
8	63	263	66	70	42	2	7	53	1.6	50 10	65 20	1.67 0.56
9	55	296	61	65	73	2	8	102	1.6	93 19	67 20	0.90 0.30
10	85	348	92	94	120	3	1	57	6.1	57 11	39 12	0.86 0.28
11	73	39	73	76	174	3	2	254	3.7	232 47	156 17	0.84 0.19
12	73	96	78	81	234	3	3	74	5.5	71 14	49 15	0.87 0.29
13	85	147	95	96	281	3	4	181	1.0	164 34	25 7	0.19 0.07
14	99	190	103	105	322	3	5	46	4.7	45 9	49 15	1.34 0.44
15	108	229	108	110	4	3	6	313	7.7	288 58	220 21	0.96 0.21
16	108	266	114	116	44	3	7	178	9.2	168 33	136 24	1.01 0.26
17	99	305	111	112	81	3	8	105	8.3	103 20	139 24	1.70 0.42
18	117	41	117	119	176	4	2	120	5.1	113 22	61 11	0.68 0.17
19	129	143	144	146	277	4	4	41	5.0	41 8	35 7	1.05 0.29
20	153	228	153	155	3	4	6	90	9.2	89 17	68 14	0.95 0.26
21	144	308	161	162	83	4	8	108	5.9	103 20	112 17	1.37 0.33

Figure 11. The raw surface brightness of the continuum subtracted $H\alpha$ image of M83, (Talbot et al. 1979). Shown superposed are the positions of the CO observations indicated with $45''$ HPBW circles. The $f_{H\alpha}$ contours are at 15 and 40 $\text{erg cm}^{-2} \text{s}^{-1} \text{arcsec}^{-2}$.

Figure 12. The integrated CO intensity contours for M83. The same scale and center as in Figure 11 are used. Here I'_{CO} ($\text{K}[T_R^*] \text{km s}^{-1}$) has been corrected for atmospheric temperature differences as discussed in the text. The contours run from 15 to 50 K km s^{-1} in increments of 5 K km s^{-1} . The central bar and the trailing arm in the Southwest are apparent.



and Vanden Bout 1973) and then in obtaining the true source radiation temperature, T_R , from the elevation dependent beam coupling coefficient, $\eta_c(e1)$.

After obtaining observed T_A^* values with the chopper wheel calibration method, several corrections were made. The data were first scaled upward by C_{fac} , where $C_{fac} = 1 + (\Delta T/T_{amb}) (\exp(\tau_0 A) - 1)$, with $\Delta T = T_{amb} - T_{atm}$, τ_0 , the zenith opacity, and $A = \csc(e1)$, the airmass (Davis and Vanden Bout 1973; Snell and Schloerb 1983). This factor was estimated and applied during data taking at 5 minute intervals. The average value of C_{fac} was 1.3, with ΔT and τ_0 uncertainties contributing 5% to errors in T_A^* .

The brightness temperatures, $T_R^* = T_A^* / \eta_{fss}$, were next calculated, where $\eta_{fss} = 0.70$ is the forward scattering and spillover efficiency. The values of $I'_{CO} (K [T_R^*] \text{ km s}^{-1}) = \int T_R^* dv$ are given in Table 10. Finally, the intensities were converted to the quantity of relevance in computing molecular hydrogen column densities, which is $I_{CO} (K [T_R] \text{ km s}^{-1})$, where T_R is the brightness temperature in the main beam, $T_R = T_R^* / \eta_c$, and η_c is the beam coupling coefficient. At 115 GHz, for a uniform source of the size of the moon, and at an elevation of 60° , $\eta_c = 1.0$. For a uniform source filling just the main beam (HPBW = $45''$) at 60° elevation, $\eta_c = 0.71$ has been found (Snell and Schloerb 1983). To determine the main beam coupling at individual source positions within M83, a non-axisymmetric CO brightness distribution was constructed from the integrated T_A^* measurements, and the ratio of the power originating

in the main and error beam over the full sky (within the velocity range) versus the power originating within the main beam was estimated. The source model calculation yielded η_c values in the range $\eta_c(60^\circ)=0.65-0.74$ for the various positions in M83. Lastly, an important correction was applied to account for a recently discovered elevation dependence of η_c (at 115 GHz) for the 13.7 m antenna of the FCRAO. Through repeated observations of the centrally peaked CO source IRC+10216, Kenney and Taylor (1987) have determined that η_c decreases monotonically with elevation, and that $\eta_c(17^\circ)/\eta_c(60^\circ)=0.65$. Observations of Venus, of diameter $d \approx 1'$, have yielded similar results. The implication is that, of the power present in the main beam at $el.=60^\circ$, 35% is shifted outward toward the sidelobes in lowering the antenna to $el.=17^\circ$. The reasons for this effect are not well understood. It is also unknown as to whether the power lost is redistributed within or without the diameter of an extended source such as M83 (bright CO diameter, $d_{CO}=8'$). To account for this uncertainty, we estimate for M83, $\eta_c(17^\circ) = 0.8 \pm 0.15 \times \eta_c(60^\circ)$. The upper and lower bounds represent a 5% power loss, and the full 35% power loss seen for IRC+10216, respectively. Additional data, including planetary observations, are now being collected (Kenney and Taylor 1987) to remedy this large uncertainty, but we are herein constrained to report our $I_{CO}(K[T_R] \text{ km s}^{-1})$ measurements with the inclusion of this 15% uncertainty due to η_c . Values for η_c and I_{CO} are given in Table 10. To summarize, the calibration procedure involves four steps:

1) Correction to chopper wheel method:

$$T_A^*(\text{corrected}) = C_{\text{fac}}(T_{\text{amb}}, \Delta T, \tau_0, e1) T_A^*(\text{observed}) \quad (\text{VII.1})$$

2) Forward scattering and spillover:

$$I'_{\text{CO}} = \int T_R^* dv = \int T_A^* / \eta_{\text{fss}} dv \quad (\text{VII.2})$$

3) Main beam coupling to source if at $e1. = 60^\circ$, where η_c is a function of position within the source:

$$I''_{\text{CO}}(e1. = 60^\circ) = I'_{\text{CO}} / \eta_c(60^\circ) = \int T_R^* / \eta_c(60^\circ) dv \quad (\text{K}[T_R] \text{ km s}^{-1}) \quad (\text{VII.3})$$

4) Coupling efficiency as a function of elevation:

$$I_{\text{CO}}(17^\circ) = (\eta_c(60^\circ) / \eta_c(17^\circ)) I''_{\text{CO}} \quad (\text{K}[T_R] \text{ km s}^{-1}) \quad (\text{VII.4})$$

At the central position of our CO map we find $I'_{\text{CO}} = 59 \text{ K}[T_R^*] \text{ km s}^{-1}$. Comparable values are found in other studies: $I'_{\text{CO}} = 50.6 \text{ K km s}^{-1}$ (Rickard and Blitz 1985), $I'_{\text{CO}} = 62 \text{ K km s}^{-1}$ (Young and Sanders 1986). From the computed coupling coefficient at this location, $\eta_c = 0.55 \pm 15\%$, we obtain $I_{\text{CO}} = 108 \text{ K}[T_R] \text{ km s}^{-1} \pm 20\%$, where the additional error originates from signal to noise errors, calibration errors, and baseline errors, all added in quadrature.

To compute $N_p(\text{H}_2)$ at each position, (a measure which implicitly includes the He content of clouds), we used the conversion

$$N_p(\text{H}_2) \text{ (protons cm}^{-2}\text{)} = (6.0 \pm 3.0) \times 10^{20} I_{\text{CO}} \text{ (K}[T_R] \text{ km s}^{-1}\text{)} \cos(i), \quad \text{VII.5}$$

where $i=27^\circ$ is the galaxy's inclination. The motivation for this particular value and a discussion of its use have been given in §IIa and Appendix A. In terms of a mass surface density $\sigma_p(H_2)$, this corresponds to $\sigma_p(H_2)(M_\odot \text{ pc}^{-2}) = 8.0 \times 10^{-21} N_p$ (protons cm^{-2}).

c) HI Observations

The HI column densities were obtained from the VLA observations of Ondrechen (1985). The 30" resolution data were smoothed to 45" and error bars were determined from half the maximum undetected flux, i.e. from regions with $N_p(\text{HI}) < 2.1 \cdot 10^{20}$ (protons cm^{-2}). There appears to be a void in HI at $R_{\text{gal}} < 108''$, including most of the central bar (c.f. Allen et al. 1986) and a ring of HI located at $R_{\text{gal}} \sim 120''$. Ondrechen notes the presence of an HI absorption feature in the inner 30" and the absence of HI absorption in the bar (despite the strong bar continuum emission present). By modeling the absorption feature, Ondrechen is able to place upper bounds on the gas column density present and conclude that there is very little absorbing gas in the inner disk. Integrating over Ondrechen's (1985) HI column density contour map, we find that the total HI mass within $R_{\text{gal}}=115''$ (~ 5 pc) ($R_{\text{sky}}=115''$) is $0.2 \times 10^9 M_\odot$, as compared to the H_2 mass of $15.4 \times 10^9 M_\odot$ within the same radius, derived from this study. Within the central 1.6 kpc (36") the contrast between the two gas distributions is even greater, with $M_{H_2}=4.0 \times 10^9 M_\odot$ and $M_{\text{HI}} < 0.01 \times 10^9 M_\odot$. At all positions in our region of interest, $R_{\text{sky}} < 150''$, the $N_p(H_2)$ distribution dominates over the $N_p(\text{HI})$ distribution by factors of tens

to several hundreds. In the following analysis, the HI number surface density $N_p(\text{HI})$ (protons cm^{-2}) has been added to the number density in the same units for the molecular gas to form N_p , the total number surface density in protons cm^{-2} , and σ_p , in $M_\odot \text{pc}^{-2}$.

d) H-alpha Fluxes And Star Formation Rates

The $\text{H}\alpha$ image was acquired from the M83 U,B,V,R, $\text{H}\alpha$ data base of TJD. A tape of these data was kindly supplied through the efforts of M. Kaufman, K. Rumstay, R. Dufour, and R. Talbot. (The full data base now exists on a FITS format magnetic tape, and is available on request from the author). The data were taken with 1-2" seeing using a 120\AA interference filter at the $\lambda 6563 \text{H}\alpha$ line. The plate images were digitized in a 1000×1000 pixel raster with resolution 0.7" per pixel, and the off-band red continuum was subtracted. The [NII] emission was removed from the image on the basis of the spectroscopic results of Dufour et al. (1980). In their study of 6 HII regions located in bar, bar-end, and spiral arm regions, Dufour et al. found a relatively constant [NII] flux contribution in each region, with $F_{[\text{NII}]} / F_{\text{H}\alpha} = 0.39 \pm 0.2$.

The raw data sensitivity per pixel was $4.0 \times 10^{-16} \text{erg cm}^{-2} \text{s}^{-1} \text{arcsec}^{-2}$, which is where we set our cutoff threshold for integration. Varying this cutoff resulted in little change in the average surface brightness in an aperture, implying that most of the flux comes from regions of higher surface brightness. The possibility

of widespread low level $H\alpha$ flux being missed by these measurements can not be ruled out, but the inclusion of such flux would not alter our results significantly. Integrating the $H\alpha$ image over each of the 21 apertures yielded the average raw $H\alpha$ brightnesses, $f'_{H\alpha}$ ($\text{erg cm}^{-2} \text{ s}^{-1} \text{ arcsec}^{-2}$), which are given in Table 10.

The greatest uncertainty in this study is due to the extinction corrections for the $H\alpha$ flux. Two estimates of the disk extinctions in the disk of M83 have been made. The first is due to Talbot (1980, henceforth T80) who modeled the optical extinction as a radial function on the basis of the radial gradient of metal abundance Z and gas surface density. The resulting correction factor, C , where $f_{H\alpha} = C f'_{H\alpha}$, ranges from $C=2.7$ at $R_{\text{gal}}=0$ to $C=1.5$ at $R=230''$. While this model is simplistic, it has the virtue of yielding values consistent with the Balmer decrement extinctions measured by Dufour et al. for 6 HII regions located throughout this radius range, three of which lie along the central bar.

In a second, more elaborate calculation, JTD examined the photometric intensities for individual pixels (smoothed to resolution $1.5'' = 64 \text{ pc}$) in their images, after first subtracting the flux contribution of the underlying disk. They solved for the blue band extinction, A_B , for each pixel, which would produce (U-B) and (B-V) colors consistent with a point on a theoretical cluster evolutionary track for a Salpeter-like IMF. In this way they obtain not only an A_B for each pixel but a "cluster" age as well. We have obtained the

JTD A_B extinction map (Figure 8c in their paper) in the form of a color slide through the courtesy of R. Dufour, and have made by-eye estimates (accurate to $\sim 30\%$) of the $45''$ beam-averaged correction factors that these extinctions imply for the $H\alpha$ data. The net effect of these corrections is to significantly raise the inferred $H\alpha$ flux along the central bar and bar-ends, giving correction factors, C , in these regions which are a factor of 30% to 70% higher than those from T80.

We consider each of the two extinction estimates described above to be somewhat less than satisfactory. The extinction method of T80 ignores azimuthal gas density variations which we find in this work to be strong. Also, the extinction estimation method of JTD is not internally consistent. Specifically, the extinctions are based on assumed cluster colors using an IMF which is later rejected by the authors, primarily on the basis of the extinction corrected luminosities and inferred ages! They state: "In much of our analysis of the data, we employ as a standard for comparison the Salpeter-like IMF defined previously [see our Table 15]. However, there are a variety of indications in our data that such a power-law IMF is a thoroughly inappropriate approximation to the star-formation processes that we are observing in the inner arms of M83".

For the simple reason that the T80 radial function gives extinction estimates in agreement with the spectroscopic results of Dufour et al., we have chosen to employ these values in our analysis. In an attempt to account for the uncertainties in the corrected flux, we have imposed

a $0.5 A_V$ error term for each HII region, which is approximately a 30% uncertainty in the corrected flux. While we expect a significant scatter in the extinction within each aperture, the mean value of many extinctions is assumed to approach Talbot's radial function, $A_V(R)$. Therefore, we divide the error term for each beam by the square root of the number of HII regions included in the average (N in Table 10) to compute the final uncertainty in $f_{H\alpha}$, σ_f (Table 10). We caution, however, that the true errors may be higher than this statistical treatment implies. The radial range $R=100''-135''$ includes the end of the bright bar, and, as indicated by the JTD analysis, corrected fluxes here may be underestimated.

To convert from corrected $f_{H\alpha}$ values to a SFR ($M_\odot \text{ pc}^{-2} \text{ Gyr}^{-1}$), we use an IMF very similar to that employed by JTD. We have used the extended Miller-Scalo IMF (Kennicutt 1983) because it best explains the observed $H\alpha$ equivalent widths versus $(B-V)$ colors of the 170 spiral galaxies examined in his study. In this regard, an examination of the local $H\alpha$ equivalent widths versus colors in M83 is considered to be an important future work. However, we will test the validity of invoking the extended Miller-Scalo in a different way in §VIII.

The conversion between $f_{H\alpha}$ and the SFR given by this IMF is, for massive stars, $M > 10 M_\odot$:

$$\begin{aligned} \text{MSFR } [M_\odot \text{ pc}^{-2} \text{ Gyr}^{-1}] = \\ 4.71 \times 10^{15} f_{H\alpha} (\text{erg cm}^{-2} \text{ s}^{-1} \text{ arcsec}^{-2}) \cos(i), \quad (\text{IIV.6}) \end{aligned}$$

and for all masses:

$$\text{SFR (M}_0 \text{ pc}^{-2} \text{ Gyr}^{-1}) = 4.54 \times 10^{16} f_{\text{H}\alpha} (\text{erg cm}^{-2} \text{ s}^{-1} \text{ arcsec}^{-2}) \cos(i), \text{ (IIV.7)}$$

where i is the galaxy's inclination. Detailed SFRs are listed in Table 11.

CHAPTER VIII

ANALYSIS AND RESULTS

a) Point By Point Comparisons

The CO map of Figure 12 closely resembles the higher resolution H α map of Figure 11, where each map is shown here on the same scale. The molecular bar stands out as a 100% contrast from the off-bar intensities at each radius. In Figure 12, contours below 15 K km s⁻¹ have been suppressed for clarity. Prominent in the H α and molecular distribution is the emissive southwestern "cusp", which is the region where the bar connects to the outlying spiral pattern. The existence of such cusp regions, characterized by numerous large bright HII regions, is apparent in many barred spiral galaxies (e.g. NGC 1300, NGC 5383). Such regions of enhanced star formation are predicted by the hydrodynamic models of gas responding to a bar potential (Sanders and Tubbs 1980; Roberts, Huntley and van Albada 1979). These models estimate the forces due to the combination of an underlying disk potential, a central bar potential and a connecting outer spiral potential, and the resulting gas motions in this environment are followed. Gas streamlines are found to converge at the bar termini, both from radii interior and exterior to this radius. The model of Roberts et al. predicts the presence of strong gas streaming motions toward the cusp along the inner edge of the spiral shock and larger departures from circular motion than does the Sanders and Tubbs model. In each case, hook-shaped cusps develop, comprising regions of enhanced gas density and star formation. The CO distribution seen in the

southwestern part of Figure 12 provides evidence for this effect. We are able to provide qualitative support for these models from the large scale distribution of gas seen. Discrimination between individual models (characterized by differing bar masses, widths, co-rotation radii, etc.) can not be accomplished without higher spatial resolution observations. In order to identify predicted departures from circular rotation, gas observations on the size scale of a few arcseconds are required (Ondrechen 1985).

We have displayed the $H\alpha$ brightness and CO intensity versus radius in Figure 13a, and have shown the number surface density of HI and H_2 in protons cm^{-2} on a log plot in Figure 13b. The $f_{H\alpha}$ and CO intensities are seen to follow very closely at all radii, with the ends of the optical bar at $100''$ showing a secondary maximum in each distribution. The HI distribution, on the other hand, shows an interior minimum and only rises to 10% of the molecular density outside of $R=100''-150''$. Allen (1986) has suggested that the regions of star formation at this outer bar radius produce the observed HI gas through photodissociation of molecular material. From our data we can conclude that there is certainly an ample supply of H_2 for this purpose.

The strong point by point correlation between α_p and $f_{H\alpha}$ is evident in Figure 14. The best fit to the derived α_p and SFR values (excluding the central position) yields the straight line in this figure, with a slope corresponding to a mean SFE of $0.73 \pm 0.04 \text{ Gyr}^{-1}$, with a correlation coefficient $b = 0.83$. No significant correlation is

Figure 13. a) The I_{CO} (this study) and $f_{H\alpha}$ (Talbot et al. 1979) brightness distributions as a function of radius in the plane of the M83. The resolution is 1.9 kpc as indicated by the bar, and the radius position is the mean radius within each aperture. The two distributions fall steeply outside of the central 50" and show a secondary maximum at $R_{gal}=100''$ corresponding to the bar-end radius. b) The molecular (this study) and HI surface densities (Ondrechen 1985) as a function of radius. The HI shows a central depression while H_2 falls with radius. The molecular surface density of the ISM dominates over the atomic component by factors of 10 to 200 within $R_{gal}=170''$.

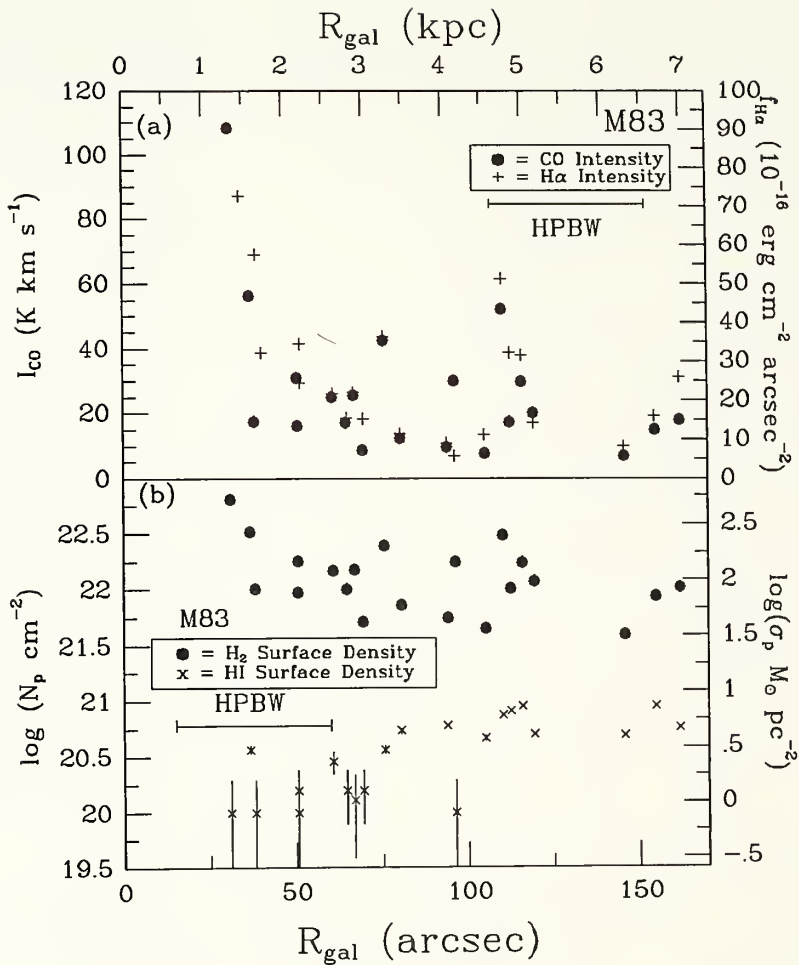
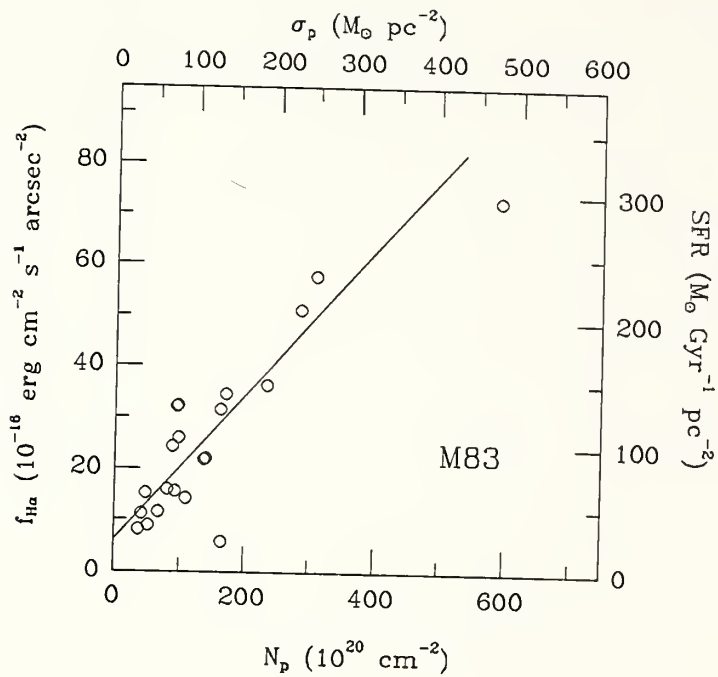


Figure 14. The $f_{H\alpha}$ brightness vs. the total gas surface density (10^{20} protons cm^{-2}) at 21 positions. A linear fit (excluding the central position) yields a slope $\text{SFE} = \text{SFR} / \sigma_{\text{gas}} = 0.81 \pm 0.04 \text{ Gyr}^{-1}$, with a linear correlation coefficient $b=0.82$.



apparent in the HI data (Figure 15).

b) Averaged Values

Azimuthal averages for the three distributions, $H\alpha$, CO, and HI are shown in Figure 16, with data given in Table 12a. Evident here is the strong nuclear emission. On the basis of far-IR photometry, the nucleus of M83 has been characterized as a "mild starburst" by Telesco and Harper (1980). The nucleus is unusually extended, consisting of a bright amorphous region of diameter $d=20''$ in the optical studies of Pastoriza (1975). These findings help account for the strong central peak we see in the $H\alpha$ emission profile in Figure 16.

In this azimuthal average, the peak intensities found at the bar-ends are diluted by the low emission values of the off-bar positions. To see the barred nature of this galaxy more clearly we have made 45° sector averages in azimuth out to $R=150''$ (Figure 17). Here the bar shows up clearly in both distributions, as does the southwest cusp, which is seen as an excess of emission in this plot at $\theta_{\text{sky}}=270^\circ$ in both distributions as well. We have included in this plot the $H\alpha$ brightnesses which would result using the extinction corrections of JTD (dashed line). Flux measurements using these extinctions yield uniformly higher values and 50% to 70% higher peaks are evident at the position angles of the central bar, in the Northeast and Southwest. We view these results with some caution however, for reasons previously discussed, and feel that they suggest, but do not demonstrate, enhanced

Figure 15. The gas surface density in HI against the density in H₂. No correlation is seen, and the molecular gas density exceeds the atomic gas density by factors of 10 to 200.

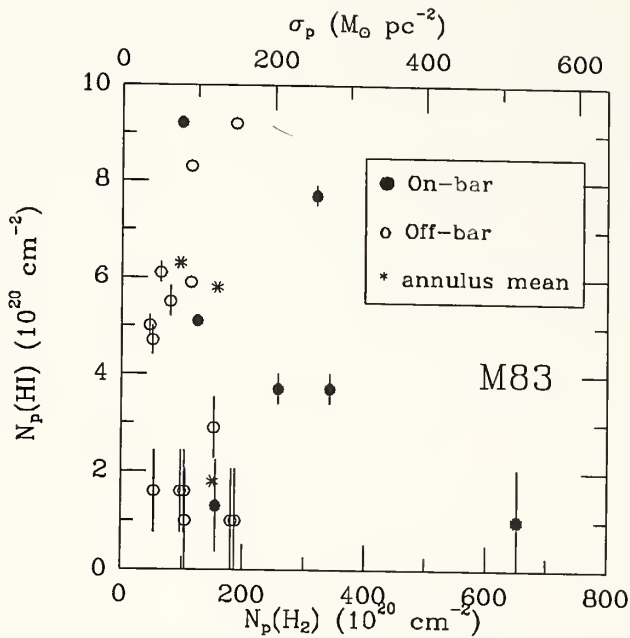


Figure 16. The azimuthally averaged CO, H α , and HI, distributions in the disk of M83. All data are smoothed to 45" resolution and plotted against mean radius in the plane of the galaxy. The HI distribution is plotted to scale relative to the CO such that multiplying the left y-axis value by 6x10²⁰ gives the gas surface density in protons cm⁻² for both the molecular and atomic species.

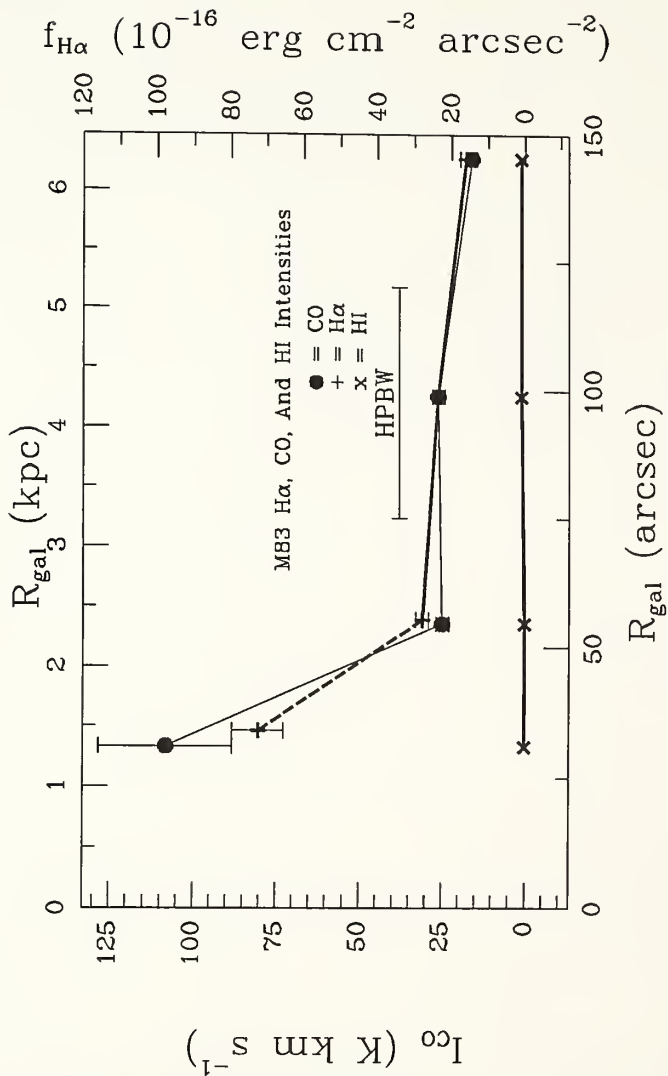


TABLE 12a AND 12b (NOTES)

These azimuth and sector mean values were obtained from the individual data of Tables 10 and 11. All quantities were spatially averaged in the frame of the galaxy with the mean sector values produced through an interpolation and averaging scheme described in §IIIb. The sectors are wedges with a 45° opening angle and extending out to $R_{gal}=160''$. The CO wedges start at the center of the galaxy, while the $H\alpha$ wedges start at $R_{gal}=15''$.

Row (1) i_A is the annulus index, i_S is the sector index.

Row (2) N is the number of observations used to compute the mean.

Row (3) $\langle R_{gal} \rangle$ is the mean radius of an annulus in the plane of the galaxy, $\langle \theta_{gal} \rangle$ is the mean position angle of a sector, measured east of the principle axis $\theta_{sky} = 226^\circ$.

Row (4) $\langle I_{CO} \rangle$ is the mean integrated CO intensity.

Row (5) δI_{CO} is the dispersion of individual I_{CO} values about the mean.

Row (6) $\sigma_{I_{CO}}$ is the uncertainty of $\langle I_{CO} \rangle$ determined from the σ_I values of Table 10.

Row (7) $\langle f_{H\alpha} \rangle$ is the mean brightness over the region.

Row (8) $\delta f_{H\alpha}$ is the dispersion of the individual $f_{H\alpha}$ values about the mean.

Row (9) $\sigma_{f_{H\alpha}}$ is the uncertainty of $\langle f_{H\alpha} \rangle$ determined from the σ_f values of Table 10.

Row (10) $\langle N_p \rangle$ is the average gas (molecular and atomic) surface density in each annulus. The uncertainty is given by $\sigma_{N_p} = 6.0 \times 10^{20} \cos(27) \sigma_{I_{CO}}$.

Row (11) $\langle SFR \rangle$ is the average star formation rate over the region. The uncertainty σ_{SFR} may be obtained from $\sigma_{SFR} = 4.52 \times 10^{16} \cos(27) \sigma_{f_{H\alpha}}$.

Row (12) $\langle SFE \rangle = \langle SFR \rangle / \langle \rho_p \rangle$ where $\langle \rho_p \rangle [M_\odot \text{pc}^{-2}] = 8.0 \times 10^{-21} \langle N_p \rangle$.

Row (13) δSFE is the dispersion of the individual SFE values about the mean.

Row (14) σ_{SFE} is the uncertainty of $\langle SFE \rangle$ determined from the σ_E values of Table 11.

TABLE 12a

AZIMUTHAL MEAN VALUES

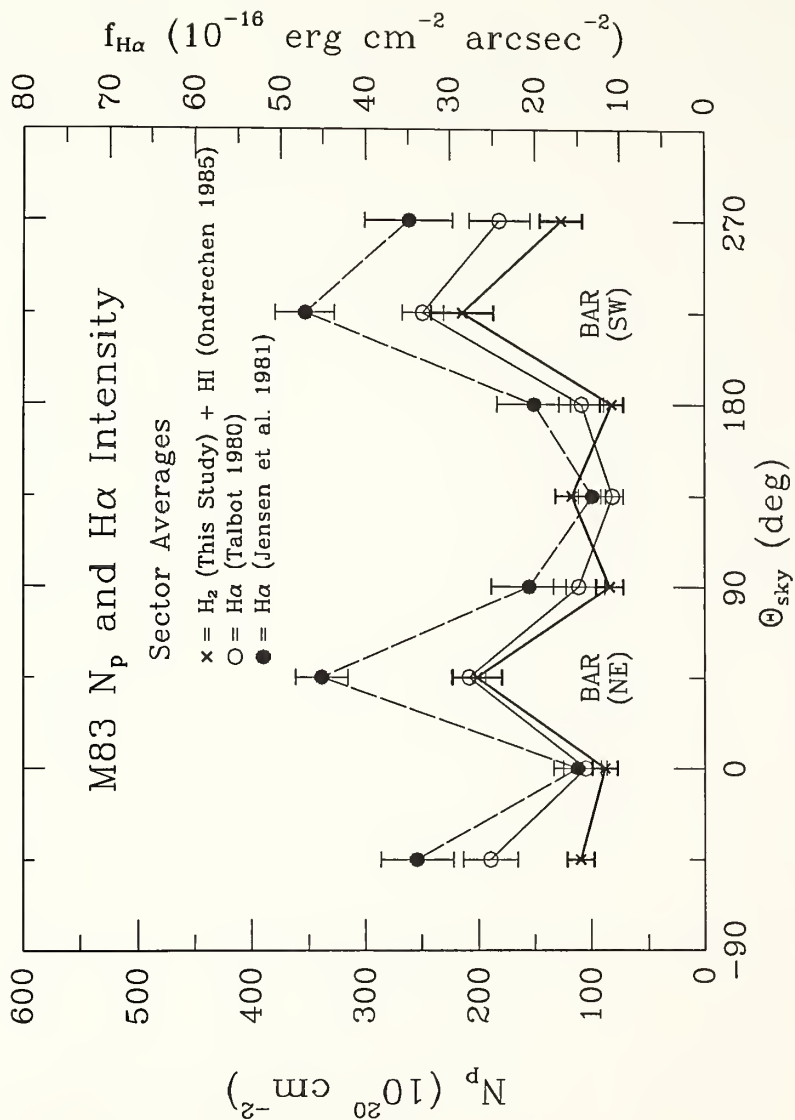
(1) i_A	1	2	3	4
(2) N	1	8	8	8
(3) $\langle R_{gal} \rangle$ (arc seconds)	34	55	99	145
(4) $\langle I_{CO} \rangle$ (K km s ⁻¹)	108	25	25	15
(5) δI_{CO} (K km s ⁻¹)	-	14	15	5
(6) σI_{CO} (K km s ⁻¹)	20.2	1.9	1.9	1.5
(7) $\langle f_{H\alpha} \rangle$ 10 ⁻¹⁶ erg/(cm ² s arcsec ²)	72.6	27.9	23.6	12.9
(8) $\delta f_{H\alpha}$ 10 ⁻¹⁶ erg/(cm ² s arcsec ²)	-	12.9	15.4	6.4
(9) $\sigma f_{H\alpha}$ 10 ⁻¹⁶ erg/(cm ² s arcsec ²)	6.9	1.7	1.4	1.5
(10) $\langle N_p \rangle$ (10 ²⁰ protons cm ⁻²)	586	135	141	86
(11) $\langle SFR \rangle$ (M ₀ pc ⁻² Gyr ⁻¹)	311	120	101	69
(12) $\langle SFE \rangle$ (Gyr ⁻¹)	0.67	1.21	0.97	1.02
(13) δSFE (Gyr ⁻¹)	-	0.33	0.37	0.22
(14) σSFE (Gyr ⁻¹)	0.15	0.12	0.10	0.13

TABLE 12b

SECTOR MEAN VALUES

(1) i_S	1	2	3	4	5	6	7	8
(2) N	2	3	2	3	2	3	2	3
(3) $\langle \theta_{sky} \rangle$ (°)	0	45	90	135	180	225	270	315
(4) $\langle I_{CO} \rangle$ (K km s ⁻¹)	14	33	13	19	13	35	20	17
(5) δI_{CO} (K km s ⁻¹)	9	14	2	10	8	15	10	1
(6) σI_{CO} (K km s ⁻¹)	2	4	2	3	2	5	3	2
(7) $\langle f_{H\alpha} \rangle$ 10 ⁻¹⁶ erg/(cm ² s arcsec ²)	14.1	27.8	14.8	10.9	14.5	33.2	24.2	25.3
(8) $\delta f_{H\alpha}$ 10 ⁻¹⁶ erg/(cm ² s arcsec ²)	10.2	15.7	7.6	7.5	4.8	15.5	8.2	7.5
(9) $\sigma f_{H\alpha}$ 10 ⁻¹⁶ erg/(cm ² s arcsec ²)	2.6	2.0	3.0	1.3	2.6	2.5	3.6	3.2
(10) $\langle N_p \rangle$ (10 ²⁰ protons cm ⁻²)	79	181	76	105	74	193	114	99
(11) $\langle SFR \rangle$ (M ₀ pc ⁻² Gyr ⁻¹)	61	119	64	47	62	143	104	109
(12) $\langle SFE \rangle$ (Gyr ⁻¹)	0.90	0.77	1.02	0.79	1.19	0.91	1.30	1.36
(13) δSFE (Gyr ⁻¹)	0.09	0.10	0.32	0.49	0.20	0.05	0.29	0.32
(14) σSFE (Gyr ⁻¹)	0.23	0.12	0.25	0.13	0.31	0.13	0.29	0.23

Figure 17. The average H α and CO emission within 8 sectors of M83's disk. Each sector extends 45° in azimuth in the plane of the sky and in radius from $R_{\text{gal}}=15''$ to 150'' for H α and from 0'' to 150'' for CO. Two H α distributions are shown here, the first (solid line) using the extinction correction method of T80 (adopted in this study), and the second using the corrections of JTD. The bar stands out clearly in all distributions at $\Theta_{\text{sky}}=45^\circ$ and 225° . The region where the bar connects to the SW spiral arm, $\Theta_{\text{sky}}=270^\circ$ also shows elevated emission in each distribution as well.



H α emission, and thus enhanced star formation rates on the central bar.

c) The Empirical Versus Observed Star Formation Efficiencies

Using the gas surface density results of this study, and the H α fluxes of TJD corrected in the way suggested by T80, we have estimated the empirical star formation efficiency, SFE_e, as motivated by T80 and discussed in §IVd. It is especially appropriate to consider this quantity in the case of M83 because, at first appearance at least, M83 seems to manifest the particular attribute which this treatment requires: a linear relationship between the star formation rate and the gas density. We have seen that for an order of magnitude range in N_p, from 40 to 400 protons cm⁻², there is a single coefficient, SFE=0.73±0.04 Gyr⁻¹ that serves to relate N_p to the total star formation rate. We must, however, keep in mind that the total SFR is an assumed extrapolation from the massive rate, MSFR, as measured by the H α flux, a point to which we will return to below.

Given a situation where the SFR follows N_p over a diverse set of disk locations and conditions, it is a reasonable step forward to assume that it does so over time as well. This leads to the differential equation IV.11 which has for its solution equation IV.12, describing an exponential fall-off of gas density at each location in time. If this description is correct, then the observed current SFE, as measured by the current gas density and SFR, should be obtainable in a second manner, as suggested by equation IV.13. We have called this second SFE

measure the empirical SFE; or SFE_e . It is obtained from the ratio of the total stellar content that has been built up over time in any location, to the amount of remaining gas, and thus bypasses the indirect, IMF-dependent determination of the low mass star forming rate from the high mass star forming rate. The form of the empirical SFE is given as:

$$SFE_e = 1/[T(1-f)] \ln(\sigma_T/\sigma_p), \quad (VIII.1)$$

where T is the age of the galaxy, f is the fraction of gas recycled through astration, σ_T is the total density (stars and gas and dark matter) and σ_p is the remaining observed gas.

To make use of equation VIII.1, we have used the σ_p values found for the four azimuthal annuli of Table 12a, and have obtained total densities, σ_T , from the detailed kinematic models of de Vaucouleurs, Pence and Devoust (1983) and Devoust and de Vaucouleurs (1980). Their best fit to the observed $H\alpha$ kinematics (Model 8) consisted of a two component Toomre model incorporating a central hot spheroid and a cold disk. We have given the model results in Table 13. Also given in Table 13 are total surface densities derived in a different manner using the simplistic equation for a spherical distribution of dynamical mass:

$$M_R = 2.25 \times 10^5 R V_{\text{circ}}^2, \quad (VIII.2)$$

where M_R is the mass within radius R , M is in M_\odot , R is in kpc and V is in km s^{-1} . By differentiating this expression with respect to R ,

TABLE 13
EMPIRICAL STAR FORMATION EFFICIENCIES FOR M83

R_{gal}	(arcsec)	34	55	98	145
D=8.9 Mpc					
R_{gal}	(kpc)	1.46	2.37	4.26	6.25
σ (Spheroid)	($M_{\odot} \text{ pc}^{-2}$)	114	27	5	2
σ (Disk)	($M_{\odot} \text{ pc}^{-2}$)	489	458	370	273
σ (Total)	($M_{\odot} \text{ pc}^{-2}$)	603	485	374	275
σ_T (dM/dR)/(2 πR)	($M_{\odot} \text{ pc}^{-2}$)	-	420	333	243
σ_D (HI+H ₂)	($M_{\odot} \text{ pc}^{-2}$)	521	120	126	77
SFE _e $\pm \sigma_e$	(Gyr ⁻¹)	0.02 \pm 0.02	0.18 \pm 0.01	0.14 \pm 0.01	0.16 \pm 0.01
SFE $\pm \sigma_E$	(Gyr ⁻¹)	0.67 0.15	1.20 0.10	0.97 0.37	1.02 0.22
D=3.7 Mpc					
R_{gal}	(kpc)	0.62	0.98	1.77	2.60
σ_T	($M_{\odot} \text{ pc}^{-2}$)	1452	1168	901	661
SFE _e $\pm \sigma_E$	(Gyr ⁻¹)	0.13 \pm 0.0	0.28 \pm 0.01	0.25 \pm 0.01	0.27 \pm 0.01

$$\sigma_T(R) = (2\pi R)^{-1} d/dR (2.25 \times 10^{-1} R V_{\text{circ}}(R)^2), \quad (\text{VIII.3})$$

and substituting in a quadratic fit to the rotation curve, $V_{\text{circ}}(R)$, (Ondrechen 1985, equation B95), we obtain $\sigma_T(R)$ values which, beyond $R=33''$, agree with the the de Vaucouleurs et al. model within 10% (Table 13). The kinematics of the HI, H α and CO emission are displayed in Table 14. The de Vaucouleurs et al. H α results are employed in the subsequent analysis.

Using the σ_p and σ_T values obtained above, we find that the empirical SFE falls short of the observed star formation efficiency outside of $R=40''$ by a factor of about 6 (Figure 18). The discrepancy at the center position is even larger. Putting the galaxy at the distance preferred by de Vaucouleurs (1979) of 3.7 Mpc (see also Comte 1981) only alleviates the difference slightly, (although it does make the ratio of stellar to H₂ mass more similar to that encountered in other galaxies). What these results indicate is that either M83 is now forming stars more efficiently than it has in the past, or else the IMF employed is not correct and our SFR and SFE measurements are overestimates because a higher fraction of O and B type stars are being produced than the extended Miller-Scalo IMF predicts.

d) Discussion and Conclusions

1) The Previous Study

We wish to compare our results to the earlier, but more extensive study of the star formation rates in M83 (T80; JTD). Before doing so

TABLE 14
M83 MAJOR AXIS PEAK VELOCITIES

index (1)	R_{gal} (arcsec) (2)	R_{gal} (kpc) (3)	V_{circ} (HI) ($km\ s^{-1}$) (4)	V_{circ} (H α) ($km\ s^{-1}$) (5)	V_{circ} (CO) ($km\ s^{-1}$) (6)
19	146	2.42	162	188	166 \pm 9
11	76	1.26	(116)	136	70
3 NE \dagger	39	0.64	(60)	79	48
1 SW \dagger	34	0.57	(54)	59	7.4 \pm 1.1
7	67	1.12	(105)	136	100 \pm 6
15	110	1.83	150	148	153
21	162	2.69	169	177	150

NOTES:

Column (1) Index of CO observation as in Table 10.

Column (2) Mean radius of CO beam (HPBW=45") weighted by the Gaussian response of the beam.

Column (3) Radius in kpc using a distance to M83 of 8.9 Mpc (Sandage and Tammann 1974).

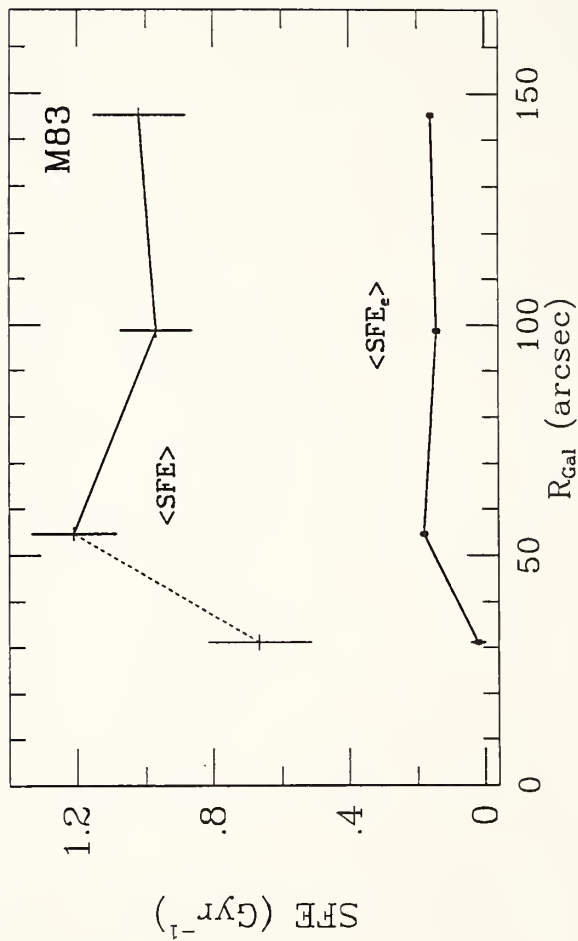
Column (4) Circular velocities obtained from Ondrechen (1985) in his analytic fit to the HI velocities. Values in parentheses are uncertain because they do not fit a bump seen in the linear portion of the curve (Ondrechen 1985).

Column (5) Circular velocities interpolated from Table 6B of the H α velocities of de Vaucouleurs et al. (1983). These velocities have been adjusted to account for the difference in inclination angle ($i=24^\circ$) used in that work, and have been presented consistently in terms of V_{LSR} where for M83, $V_{LSR}=V_{SUN} + 1.9\ km\ s^{-1}$.

Column (6) $V_{circ} = (V_{obs} - V_{sys})/\sin(i)$ along the major axis, where V_{obs} is the peak velocity in the CO line profile, V_{sys} is adopted from de Vaucouleurs et al.; $V_{sys} = 511\ km\ s^{-1}$ (w.r.t. the local standard of rest), and $i=27^\circ$. Uncertainties are derived from differences in the line-peak velocity, and the peak of the best fit Gaussian profile. The systematically lower CO velocities inward of 1.3' are a product of the low resolution employed in this study (HPBW=1.9 kpc), serving to bias the peak velocity by giving higher weight to the inner, more emissive regions in the beam.

Figure 18.

The observed and modeled star formation efficiencies plotted against galactic radius. The upper curve shows the current efficiency $\langle \text{SFE} \rangle = \langle \text{SFR} \rangle / \langle \dot{q} \rangle$ averaged over each radial bin as determined by the H α and CO emission. The SFR is obtained from the H α flux by determining the MSFR and extrapolating to a total SFR using the MSFR Miller-Scalo IMF. The lower curve shows $\langle \text{SFE}_e \rangle = 1 / [T(1-f)] \ln[\sigma_T(R) / \sigma_p(R)]$, a measure of the efficiency averaged over the lifetime of the disk as indicated by the low mass stellar population. Here $T=10$ Gyr and $f=0.2$. The values for σ_T were obtained from the mass model (No. 8) of de Vaucouleurs et al. (1983). The large difference between $\langle \text{SFE} \rangle$ and $\langle \text{SFE}_e \rangle$ at each radius suggests that either the low mass SFR is not linearly related to the gas density over the lifetime of the galaxy (Marson 1986), or else that the IMF employed is incorrect (Jensen et al., 1981).



we review the differences, both in observational data and methodology, that exist between our study and theirs.

In estimating the gas surface densities in the inner disk ($R < 150''$) of M83, $\sigma_p = \sigma_p(\text{H}_2) + \sigma_p(\text{HI})$ ($M_\odot \text{pc}^{-2}$), T80 and JTD use earlier data sets which give $\sigma_p(\text{HI})$ values which are a factor of 8 greater than the VLA results of Ondrechen (1985). The latter values are used here. Also, T80 and JTD use $\sigma_p(\text{H}_2)$ values that are a factor of 12 smaller than those found in this study. The factor of 12 discrepancy arises from the combination of a factor of 2 difference in the I_{CO} intensities measured by Combes et al. (1978) and by ourselves, and a factor of 6 in the conversion factor applied to obtain $\sigma_p(\text{H}_2)$. The net effect is that our $\sigma_p(\text{H}_2 + \text{HI})$ values are an order of magnitude greater than those reported in T80.

Equally large differences exist in the star formation rates derived. Due to the differing extinction corrections, assumed IMFs, and conversion factors from $f_{\text{H}\alpha}$ to SFR, our SFR are about a factor of 3 higher than those of T80, and a factor of 9 higher than those of JTD. We have already discussed our difficulty in determining the best extinction correction to use for the $\text{H}\alpha$ flux. While we have chosen to employ the radial function of T80, we have also presented, in Figure 17, the results which would obtain if the cluster extinctions of JTD were employed. As discussed by JTD, these A_B values yield higher $f_{\text{H}\alpha}$ and SFR values along the central bar. Finally, because T80 and JTD place M83 at a distance $D=3.75$ Mpc, while we use $D=8.9$ Mpc, our derived

total mass surface densities $\sigma_T(R)$ are a factor of 2.4 lower than theirs.

Dispite the large differences in observational input, our analysis and conclusions run parallel to specific parts of JTD's work. Both studies undertake to measure the quantities SFR, SFE, and SFE_e across the disk, and then to explain the large disparity found between the later two of these quantities in terms of departures from the nomnally expected star formation rates and initial mass function.

Three independent measures of the detailed star formation rates were obtained by JTD. The quantity SFR_{UVB} was determined by solving the U-B, B-V colors of each pixel for the disk and star cluster extinction and cluster age. Cluster masses were then calculated from the observed luminosities and using these masses and the ages, current SFRs, termed SFR_{UVB} , were inferred. From the extinction corrected $H\alpha$ flux, a second SFR rate was computed, $SFR_{H\alpha}$, which is completely analogous to the quantity we term SFR. Finally, SFR_e values were obtained from the product ($\alpha_p SFE_e$) which represents the current rate if the the SFR follows the gas density over time and is to account for the total stellar disk density. These three measures are each sensitive to a different mass range: SFR_{UVB} to stars with $M > 3 M_0$; $SFR_{H\alpha}$ to high mass stars, $M=10 M_0 - 60 M_0$; SFR_e to the low mass, $M \approx 0.5 M_0 - 2.5 M_0$ stars, as well as the total gas content.

As a surprising result, TJD find that the three measures predict very different total yields of new formed stars within $R=120''$. They

find SFR_{UBV} values are greater than $SFR_{H\alpha}$ values by factors of 2 to 6, while $SFR_{H\alpha}$ values exceed SFR_e values by factors of 2 to 4. A possible explanation offered by the authors to account for the first discrepancy is that the IMF may actually be truncated at a far lower maximum mass ($25 M_{\odot}$) than anticipated ($60 M_{\odot}$). This adjustment would serve to raise the derived $SFR_{H\alpha}$ as discussed in Appendix A. The major problem with this idea is that, with their data, JDT then find a gas depletion timescale of 100 to 300 million years, a suspiciously short period of time. To remedy the second disparity (between SFR_e and the other two rates) the authors suggest two possible explanations. Either very few low mass stars are produced at the sites of the young clusters (i.e.: a bimodel IMF involving spatially distinct locations for high and low mass star formation) or else M83 is currently undergoing an unusually active phase of star formation. We now relate these findings to our own.

ii) The Implications of Our Results

Using the extended Miller-Scalo IMF the star formation rates we derive from the $H\alpha$ flux are commensurate (to within a factor of 2 at all radii) with JDT's SFR_{UBV} values. This then alleviates the direct need to postulate an unusual IMF to bring SFR_{UBV} and $SFR_{H\alpha}$ into agreement. It is important to note that JTD find other indicators, such as a relation between cluster luminosity and cluster age, which indicate an unusual IMF.

Secondly, we find that with our appreciably larger gas density estimates, the gas depletion time scale is no longer so alarmingly short; we set it at a value ($SFE^{-1} \approx 1 \text{ Gyr}$) similar to that found for other galaxies sampled in this manner (Kennicutt 1983; DeGioia-Eastwood *et al.* 1984). The presence of a rich gaseous disk in M83, with a surface density peaking strongly in the central 30" then provides a natural explanation for the prodigious star formation rates and large surface brightnesses seen.

As for the question of the detailed star forming efficiency on and off the bright central bar, we are left in somewhat of a quandary. While the detailed cluster extinctions of JTD yield enhanced $H\alpha$ fluxes, SFRs, and SFEs on the bar and especially the bar-ends when applied in our study (Figure 17) as in their own, (an effect which is not evident when we employ the radial extinctions of T80), the extinction estimation method of JTD is not internally consistent (SVII.d). We can only conclude that there is the suggestion of higher star forming efficiency on the bar, and bar-ends. This might be naturally explained by the bar's high gas density (our study) and hydrodynamic action (Ondrechen 1985, 1985a) along the bar and cusps. Even so, the $f_{H\alpha}(\tau_{\text{sky}})$ functional form (dashed line) displayed Figure 17 should be regarded as a qualitative and not a quantitative result.

It is interesting that we find a lower SFE in the central region of M83 ($R < 45''$) than in the disk ($45'' < R < 150''$). However, this result too is very uncertain because of our poor knowledge of the extinctions in

the nucleus. Dufour et al. (1980) measure only two Balmer decrement extinction values within this radius. Furthermore, the inner 15" of the TJD H α image, having been "masked-out" due to calibration difficulties, is not included in the calculation of the average H α flux. Looking on the positive side, the inner 15" represents only a tenth of the total area considered for our innermost SFE value, and through other methods, (Bohlin et al. 1983 and references therein), even smaller nuclear extinctions values than those measured by Dufour et al. have been found. Great uncertainty still exists in the SFE measurement here, with one contribution being the possible presence of heated molecular clouds which could cause an overestimation of $\alpha_p(\text{H}_2)$ and thus an underestimation of the SFE. For these reasons we have connected the central SFE point in Figure 18 to the SFE(R) function with a dashed line. If the SFE is indeed lower here than in the outer points, it suggests that while the action of the bar hydrodynamics is efficient in bringing gas to the galaxy's center (Sanders and Tubbs 1980; Tubbs 1982) the star forming efficiency of this process for barred spirals may not be as great as anticipated (e.g. Mountain et al. 1987). If enough molecular clouds are swept into the same region, prodigious star formation may be seen to occur (c.f. Bohlin et al. 1983), without necessarily implying that efficient star formation is occurring. Reasons why, in some circumstances, the hydrodynamic action of barred spirals may actually surpress efficient star formation is given by Tubbs (1982).

Finally, we agree with the finding of T80 that, in M83's disk, $SFE > SFE_e$, and with that of JTD, $SFR_{H\alpha} > SFR_e = \alpha_p SFE_e$, by a factor of ~ 6 , specifically for $45'' < R < 150''$. This result can be interpreted as evidence that a linear relationship between the gas density and the SFR does not hold over a galaxy's lifetime, e.g. that M83 could currently be engaged in a "burst" of star forming activity. Alternatively, the result can be interpreted as providing evidence (JTD) that the concept of a universal IMF cannot be applied with any validity to the individual star forming regions of this galaxy. A combination of these ideas has recently been put forth by Larson (1986). He models a time-evolving IMF for M83, where low mass star formation proceeds at a constant rate while massive star formation follows the gas density in time, albeit nonlinearly ($\alpha_p^{1.4}$). The model is consistent with our finding that an exponential fall off of low mass star formation in time will overestimate the current stellar population of the disk. High mass star formation is also isolated spatially from low mass star formation in Larson's model.

These issues cannot be resolved with the data of this study. Tests still need to be conceived and conducted to search for variations in the IMF from cluster to cluster with a view toward finding a dependence on environment (i.e. arm and bar versus interarm regions). A step in this direction has been taken by Rumstey and Kaufman (1983), who find an environmental dependence on HII region size in M83. One possible way to learn more about the true IMF(s) would be to compile

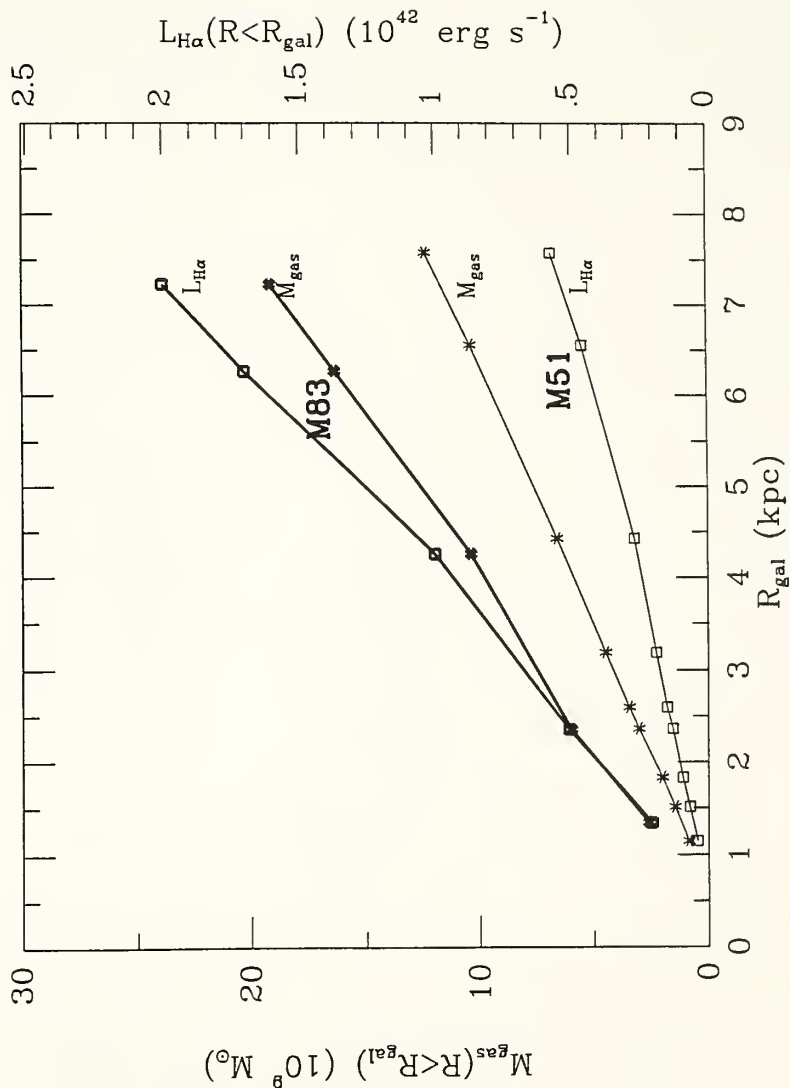
the ratios of the $H\alpha$ equivalent widths to color indices (B-V) for the star clusters associated with HII regions. This might be attempted after detailed Balmer decrement extinction measures are acquired. The $EW(H\alpha)/(B-V)$ ratio, in a statistical sense, can distinguish between various IMFs in the global parameters of galaxy disks (Kennicutt 1983), and the application of this method to individual disk regions within a galaxy seems a logical (if very difficult) next step in studies of this type.

e) A Comparison of M83 and M51

We compare the integrated gas surface density and $H\alpha$ flux for the two galaxies M51 and M83 in Figure 19. The azimuthally averaged distributions were seen to fall off with radius in proportion to $1/R$ (or faster for the inner region of M83), and so the surface integrals: $M = \int \rho_p(R) dA$; $L_{H\alpha} = \int F_{H\alpha} dA$, shown in this figure rise almost linearly with radius (with our 45" resolution). The large $H\alpha$ luminosity and gas mass of M83 is apparent in this figure as well. It is also evident here that the $H\alpha$ emission maintains a higher ratio to the gas mass in M83 than in M51, which has led us to infer higher star formation efficiencies, $SFE_{M83} \approx 0.7 \text{ Gyr}^{-1}$, vs. $SFE_{M51} \approx 0.4 \text{ Gyr}^{-1}$, for this galaxy. From a sample of only two galaxies it is difficult to accredit the difference in mean SFE seen to some a particular aspect of galaxy morphology. Furthermore, it may be inappropriate. An examination of a survey of the star formation rates in 170 disk galaxies (Kennicutt 1983; Elmegreen 1987) shows no obvious distinction

Figure 19.

M51 and M83 integrated H α luminosity and gas mass. The L $H\alpha$ functions are from surface integrals of the PDS H α image of Kennicutt (personal communication) using the extinction functions of van der Hulst and Kennicutt (1987) for M51, and the H α image of Talbot, Jensen, and Dufour (1979) using the extinction functions of Talbot (1980) for M83. The gas mass is computed from the surface integral of $q_{HI} + q_{H_2}$. The HI data is from Rots (personal communication) for M51 and Ondrechen (1985) for M83. The q_{H_2} values are from this study using $q_{H_2} (M_{\odot} pc^{-2}) = 4.8 (M_{\odot} pc^{-2}) / (K[TR]) km s^{-1} x I_{CO} (K[TR]) km s^{-1}) \cos(i)$, for both galaxies. All integrated quantities scale as the distance, D, to the galaxy, where here we have used $D_{M51} = 9.6$ Mpc and $D_{M83} = 8.9$ Mpc.



between the total star formation rates found in Sc galaxies and barred spirals, and a factor of 5 scatter exists in total SFR for each class. Until more is learned about the corresponding total gas content in individual galaxies (often dominated by the molecular component), very little can be said about star forming efficiency versus morphology. We must also stress that the outer disk of M83 ($R > 120''$), which displays well defined spiral arms and a greater HI density than the inner region, has barely been sampled in our molecular observations. Thus, a comparison of the efficiencies of two different spiral patterns has not herein been made.

Given these limitations to our study, the number of similarities found between the two galaxies is striking:

1) The mean SFE with radius in each disk is relatively constant, implying an overall current linear relationship between the gas densities and star formation rates.

2) The empirical star formation efficiency, SFE_e , calculated on the basis of the star forming histories of the galaxies, as indicated by the current supply of gas and the total stellar mass now present, is smaller (by a factor of 2 for M51 and factor of 6 for M83) than the current efficiency found from the H α flux and gas mass of each galaxy. (A similar result was also obtained by T80 for the Milky Way). One explanation of this result is that the star formation rate has not followed the gas content linearly in the past or else has not followed

it with the same proportionality constant as it now does (e.g. the galaxy in question is now in a period of enhanced star formation). A second explanation (conceivable for either galaxy) is that our extrapolation from a high mass to a low mass star formation rate is in error.

3) There is enhanced molecular emission and an inferred enhancement of total molecular gas surface density along the arms of M51 and the bar of M83. This is most likely due to the strong spiral (M51) and bar (M83) potentials present.

4) There appears to be definitive evidence in the case of M51 and suggestive evidence in the case of M83 that enhanced (non-linear) star forming efficiencies result in the regions where cloud orbit crowding occurs (the spiral arms in M51 and bar-ends in M83). If the enhanced molecular emission seen at these locations is the product of cloud heating, and not increased cloud number densities at these positions, this will serve to make the star formation efficiencies we find even higher. Since our star formation rates are measured by the ionized flux from massive stars, these results apply, to first order, to massive star formation rates and efficiencies. These high efficiencies are offset by comparatively lower efficiencies in interarm regions so as to yield an overall linear (current) relation as a function of radius in the disk between the gas content and star formation rate.

APPENDIX A

SUPPLEMENTARY ERROR ANALYSIS FOR M51

a) Introduction

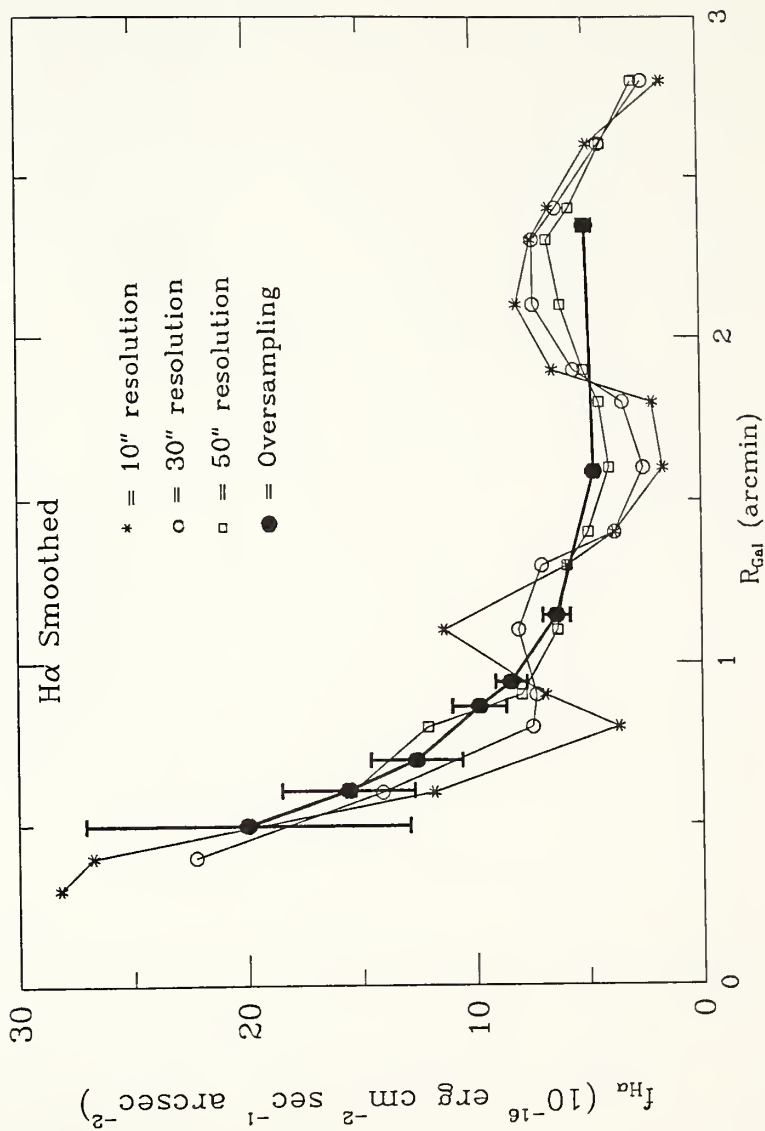
The process of inferring Lyman continuum fluxes from $H\alpha$ observations and subsequently converting these values to massive and total star formation rates is a process full of assumptions and uncertainties. Likewise, the practice of linearly converting integrated CO intensities into nucleon densities is still controversial and involves invoking some of the nuances of average cloud properties. We will undertake in this Appendix to examine the assumptions involved in each conversion process and reach conclusions as to the reliability of our results. Specifically, the assertion that the massive star formation efficiency, (MSFE), and the total SFE is manifestly higher on M51's spiral arms than on the interarms is critically examined, with a view toward finding assumptions, which, if weakened, could simulate this effect. Our results are summarized in SA.e.

b) The Resolution Problem

As can be seen in Figures 1-4, the data presented in this study are oversampled, with high oversampling occurring in the region $R_{\text{sky}} < 100''$. The effect of this oversampling and the averaging of oversampled data values results in a smoothing of all features, i.e. the minima and maxima actually present in each distribution. We are able to gauge the

effect of our sampling scheme only on the $H\alpha$ data set, since here the data are available at 8" resolution. In Figure 20 we present the azimuthally averaged $H\alpha$ distributions smoothed to 10", 30", and 50" for comparison with the oversampled results shown in Figure 4. We can see in Figure 20 that detailed variations in $f_{H\alpha}(R)$ are indeed lost. We readily concede that our resolution of 45" will cause the smearing out of high surface density enhancements in the molecular gas density thereby causing an underestimation of the true gas overdensity in regions such as the spiral arms, but would this necessarily lead to an overestimation of the $SFE=SFR/\sigma_{gas}$? A Gaussian aperture of $HPBW = 45''$ will smear out features possessing an intrinsic scale up to 90", which is wider than the observed optical arms in M51. Thus, if broad molecular arms exist in this galaxy, we are bound to detect a diminished contrast compared to interarm regions. It is exactly for this reason that we have smoothed the other ($H\alpha$, HI) emission distributions to this same resolution. At 45" resolution, the spiral pattern in the $H\alpha$ flux distribution is still readily apparent, while it is not seen at most radii in the gas density distribution, even when an underlying smooth component is subtracted at this resolution. While we do not conclude from this the absence of molecular or HI spiral arms, we do conclude that there is not a region by region linear relation between the gas distribution and the star formation rate. Such a relation would be evident at any resolution. A gas surface density enhancement does not exist with the same strength or confinement as the intense star formation seen on the spiral arms.

Figure 20. The radial $H\alpha$ distribution in M51 under various resolutions. The 10", 30" and 50" resolution results are taken from uniformly weighted annular averages of the indicated widths, with the inner edge of the annulus stepped outward in 10" increments. The oversampled result is from the Gaussian apertures of the CO map shown in Figure 1.



c) Molecular Cloud Masses from Integrated CO Intensities

The Milky Way molecular cloud population has been the object of many global and local studies, and the statistical distribution and correlation of such cloud properties as size, temperature, linewidth and position, are becoming known. Our conversion of CO integrated intensity to an $H_2 + He$ mass surface density, expressed as N_p (protons) cm^{-2} at each beam position is based on both empirical and theoretical results which imply a direct proportionality between these two quantities. We describe these results in turn below.

i) Empirical Results

In observations of 3 dark clouds, Young and Scoville 1982 (YS) compare I_{CO} measurements with the visual extinctions found by Dickman (1978), and assuming a constant gas to dust ratio, obtain a conversion factor $b = N_p / I_{CO} = (5.4 \pm 4) \times 10^{20}$ (protons) cm^{-2} $(K[T_R^*] km s^{-1})^{-1}$. In a similar study of 5 dark clouds, employing a mean ^{12}CO to ^{13}CO ratio found in their galactic plane survey, Sanders, Solomon, and Scoville (1984, henceforth SSS) obtain $b = (7.8 \pm 2.0) \times 10^{20} cm^{-2} (K[T_R^*] km s^{-1})^{-1}$. In a study of the correlation between diffuse galactic gamma ray emission and the CO intensities of two giant molecular clouds, Bloemen et al. (1984) find $b = (5.2 \pm 2.4) \times 10^{20}$, and in a second study comparing high energy (>70 Mev) gamma ray emission with CO and HI surveys which cover more than half of the Milky Way (Bloemen et al. 1986) obtain $b = (5.6 \pm 0.7) \times 10^{20}$ with no dependence,

within the errors, with galactic radius. Reviews of these and other empirical studies may be found in Bloeman et al. (1986), SSS and YS. Most recently, Scoville et al. (1987) have used a compilation of 1427 clouds from the Massachusetts-Stony Brook Galactic Plane Survey to compare the virial masses of individual clouds with their integrated CO luminosity. For the fraction of clouds with known distances (≈ 0.3), a linear proportionality of $b = (4.9 \pm 0.3) \times 10^{20} N_p \text{ cm}^{-2} (K[T_R^*] \text{ km s}^{-1})^{-1}$ was obtained. For the 170 clouds with associated HII regions, the same proportionality, within errors, was found to apply.

ii) Conversions Using a Uniform Sample

While it may seem counterintuitive that an optically thick line can serve to measure a quantity such as the total mass of a molecular cloud, this assertion has a basis not only in empirical results, but exists on a reasonable theoretical footing, as shown, for example, in the treatment of Dickman, Snell and Schloerb (1986, henceforth DSS). Here the number surface density of hydrogen molecules, N_p , measured in protons cm^{-2} within a uniform aperture, A , is related to the mean parameters of an ensemble of molecular clouds observed within that aperture:

$$N_p = N_c A^{-1} (\pi/6) \langle \ell^3 \rho \rangle \quad (\text{A.1})$$

where N_c is the number of clouds, ℓ is the cloud diameter, and ρ is the average cloud density, with brackets indicating an ensemble average. Likewise, the integrated CO intensity is formed by the ensemble average:

$$I_{CO} = N_c A^{-1} (\pi/4) \langle \ell^2 \Delta v \rangle T \quad (A.2)$$

where Δv is the velocity dispersion width at half power of each cloud, and T is the mean radiation temperature. With the assumption of clouds existing in virial equilibrium, $\Delta v = C_1 \rho^{1/2} \ell$, where C_1 is a constant. This yields

$$N_p / I_{CO} = C_2 T^{-1} \langle \ell^3 \rho \rangle / \langle \ell^3 \rho^{1/2} \rangle \quad (A.3)$$

where C_2 is another constant. Removing the average cloud diameter from the ensemble average, and assuming a "standard cloud" radiation temperature of 10 K and density of 200 cm^{-3} (Sanders et al. 1985) directly yields the proportionality constant $b = 5.4 \cdot 10^{20}$ protons $\text{cm}^{-2} (\text{K km s}^{-1})^{-1}$, where $N_p = b I_{CO}$. Rather than make such an assumption concerning cloud densities, which are not a directly observable quantity, DSS instead use the observed size-linewidth dependence, $\Delta v(\ell)$, which characterizes the molecular clouds of the Milky Way (Sanders et al. 1985; Larson 1981). Through this relationship, Δv and ρ may be eliminated in favor of ℓ . The molecular cloud size distribution found for the Milky Way survey by Sanders et al. (1985) was inserted into the ensemble averages to yield $b = 4.6 \pm 0.2 \cdot 10^{20}$ protons $\text{cm}^{-2} (\text{K km s}^{-1})^{-1}$. This result is somewhat smaller than the gamma ray and dark cloud results.

It is important to note that in expression A.3, the final value of b is proportional to T^{-1} . In the DSS analysis, a mean radiation temperature of 10 K was assumed. If this radiation temperature is not

everywhere maintained, e.g. if clouds are heated, say by newly formed stars within them, and the mean cloud temperatures rise, then we are prone to overestimate their surface density. This is considered the most important uncertainty in the DSS treatment (Dickman 1987, personal communication). While Scoville et al. (1987) find no difference in the virial mass to I_{CO} ratio for clouds associated with HII regions in the Milky Way, i.e., those which might be expected to be hotter, there is some concern as to whether the virial mass ($M_{vir} \sim \Delta v^2 \ell$) is truly representative of the actual cloud mass. Observational efforts are underway (R. Snell 1987, personal communication) to study this issue.

In this work we adopt a conversion given by

$$N_p(H_2) = 6 \pm 3 \times 10^{20} I_{CO} \quad (A.4)$$

with the constant $b = 6 \pm 3 \times 10^{20}$ in units of protons cm^{-2} ($K[T_R]$ km s^{-1}) to bracket the range of results presented. Since η_c is near unity for Milky Way molecular cloud observations made at FCRAO ($T_R = T_R^*$), while η_c is typically about 0.70 for extragalactic observations, we convert our temperature units to $T_R = T_R^*/\eta_c$ prior to estimating N_p . Implicit here is the assumption that the molecular clouds in M51 statistically resemble the cloud population of the Milky Way. It should also be noted that even for a value of b as low as 3.0×10^{20} , we still would retain the result that the molecular hydrogen density dominates over the atom hydrogen density in the inner disk of M51. Thus, a change in the conversion factor within the limits we have specified would result

in little change in the relative shape of the total gas surface density herein derived.

iii) A different cloud population on the arms?

The shapes of clouds on spiral arm may be different than those in the interarm. In one model, a cloud, upon entering a spiral density shock, may become flattened and compressed by the sudden increase in surface pressure (Woodward 1978). According to this model (which neglects magnetic or turbulent support) clouds may, for a short time, achieve a pancake-like shape with the long axis oriented orthogonally to the line of motion, and then expand slowly over 10^7 yr to a configuration with a density enhancement 6 to 8 times the preshock value. Even if support against collapse is provided by locked-in magnetic fields, some compression along the leading and trailing surfaces due to the ram pressure seems likely. In such cases we must abandon the virial assumption in the conversion derivation. The basic relationship

$$I_{CO} = N_C A^{-1} \pi/4 \langle \rho^2 \Delta v \rangle T \quad (\text{A.5})$$

then becomes

$$I_{CO} = N_C A^{-1} \pi/4 \langle \ell \ell' \Delta v' T' \rangle \quad (\text{A.6})$$

where ℓ' is the reduced cloud length (assuming face on viewing of the galaxy), $\Delta v'$ is the velocity dispersion of the perturbed cloud, and T' is its new radiation temperature. Under such conditions we would

expect T' and $\Delta v'$ to be elevated while ℓ' is decreased. Therefore, whether or not we see more than the normal emission from such clouds depends then on whether

$$(T'/T) (\Delta v'/\Delta v) > \ell/\ell'. \quad (A.7)$$

Very little is known as to whether these effects actually occur in molecular clouds, or what the magnitudes of the perturbations might be. This is mostly because we do not even have a clear picture of the mechanism providing cloud support. The above arguments imply that if clouds do become compressed in arms such that they present a smaller cross-section to the face-on direction, and this effect is not offset by temperature or velocity enhancements, it might be possible to underestimate the N_p for the observed I_{CO} values.

d) Star Formation Rates from H-alpha Brightnesses

1) Introduction

In this section we describe, in order, the possible paths taken by a Lyman continuum photon originating from a massive star; the production of $H\alpha$ emission; $H\alpha$ extinction corrections for M51; and finally the conversion of $H\alpha$ surface brightness to a star formation rate for various initial mass functions. We shall end by selecting a conversion factor, C , for this purpose, and identify the uncertainties inherent in its use.

ii) The Possible Paths for a Lyman Continuum Photon

After emission from a massive star, $M > 10 M_{\odot}$, a Lyman continuum photon will experience one of the possible paths outlined and discussed below:

I) Absorption by the Dust within an HII Region.

II) Escape from the HII Region,

a) Leading to capture elsewhere in the parent galaxy.

b) To become part of the galaxy's UV continuum.

III) Ionization within the HII Region,

a) Producing an $H\alpha$ photon.

b) Producing other Balmer transitions.

The importance of the Lyman continuum absorption by dust within Milky Way and extragalactic HII regions is still poorly understood. Evidence that such dust exists in quantities capable of competing for the UV flux is given by Sarazin (1976) in a study of extinction and metallicity gradients with galaxian radii in three nearby galaxies. Sarazin ascribes the observed extinction gradient with radius to the presence of local dust which appears to follow the HII region's heavy element abundances, Z . He notes, however, that the observations might alternatively be explained by differences in excitation due to variations in stellar content with radius within these regions. Smith, Biermann, and Mezger (1978) also conclude that dust absorption is

important in the central HII regions of the Milky Way. By modeling the total dust cross section per hydrogen atom as a function of galactic radius, they predict a fractional absorption by dust of the UV continuum of up to 0.5. However, in near-infrared observations of 14 extragalactic HII regions, Strom et al. (1974) found little or no evidence of surviving heated dust grains. Due to the inconsistency of the models and observations, we have chosen not to attempt to correct for the dust absorption of the continuum flux. The effect may be present, and thus our Lyman continuum values obtained from counting recombination photons and our derived star formation rates are correctly regarded as lower limits.

An alternative route for the UV photon is to escape from the HII region entirely (i.e., a density bounded region). Evidence that this generally does not occur is given by Sarazin (1976). Ions possessing low ionization potentials ([OII], [SII], and [NII]) which typically reside in the outer parts of nebulae, are found to exhibit strong emission. Were the HII regions density bounded, much lower emission would be expected. As a more difficult problem, Smith, Biermann, and Mezger (1978) raise the possibility that a large fraction of O stars in the Milky Way may be naked, i.e., possess no surrounding HII region. This situation is difficult to test for in other galaxies and once again implies that the $H\alpha$ -derived massive star formation rate for a galaxy is to be treated as a lower limit. In this regard, Reynolds (1984) has shown that there exists a significant diffuse $H\alpha$ background

in the high latitudes of the Milky Way, implying $2-4 \times 10^6$ Lyman continuum photons s^{-1} per cm^2 of disk. This emission appears to originate predominantly from Milky Way planetary nebulae and/or O stars. But in our study, the bright $H\alpha$ emission from individual HII regions typically exceeds the maximum possible undetected diffuse $H\alpha$ emission in each beam, implying that remote ionization is not an important concern. Escaping UV flux, as mentioned above, may still be important.

We have arrived finally at the most interesting and tractable case: the Lyman continuum ionization of gas within an HII region. In a radiation-bounded HII region virtually all continuum photons (unabsorbed by dust) will lead to ionizations and each continuum photon will eventually produce one Balmer photon. This is true by virtue of the fact that such a region is opaque to Lyman transitions. Lyman recombinations from levels greater than $n=2$ will emit photons that are quickly reabsorbed by the vast supply of ground state hydrogen atoms present. The process will repeat until a Balmer transition occurs followed by a Lyman- α transition. The Lyman- α photon then makes its way out of the region in a random walk of ionizations and recombinations, while the Balmer photon, having little chance of absorption, escapes directly. In an equilibrium situation (Osterbrock 1974, Case B, $T_e=5000$ K) the emergent flux of a single Balmer transition serves to calibrate the entire process, with a relation between the Lyman continuum photon flux, F'_{Ly} and the $H\alpha$ photon flux, $F'_{H\alpha}$, given by $F'_{Ly} = F'_{H\alpha}/0.487$ (Talbot 1980).

We have seen how the $H\alpha$ line measures the ionizing flux, and we must next account for the dust extinction of the $H\alpha$ emission, both from the local dust, and that located in the plane of the parent galaxy. The extinction from the plane of the Milky Way at the $H\alpha$ wavelength of 6563\AA is small, $A_V=0.2-0.3$ magnitudes for galaxies in this study (de Vaucouleurs et al. 1976) and will be accounted for by the extinction corrections discribed below.

iii) The $H\alpha$ Extinction Correction

In this work we use an $H\alpha$ extinction dependence with radius for M51 largely determined by the work of van der Hulst and Kennicutt (1987, henceforth vK). Their study used dual frequency radio continuum maps taken at the Very Large Array (VLA) of the National Radio Astronomy Observatory, and the same $H\alpha$ data which is presented here in Figure 1. By isolating the free-free component of the continuum emission, and identifying corresponding HII regions in the optical image, they were able to directly measure the extinction to the 40 brightest regions, out to $R = 3'$ in the disk. They find the extinction to be very patchy, with adjacent regions in some cases exhibiting over a magnitude of difference in A_V , but that a fairly constant mean value of $\langle A_V \rangle$ was maintained over the observed disk. They find a small trend in this mean value with radius, with average values at the two extremes in radius of $\langle A_V(R=1.2') \rangle = 2.1$ and $\langle A_V(R=2.8') \rangle = 1.6$, and a large dispersion, $\sigma_{A_V} \approx 1.1$, over the entire range. The authors confirmed their results by conducting spectrophotometric observations of the

Balmer decrement in 8 selected regions, which yielded A_V values in good agreement with the values obtained by the radio continuum method. Furthermore, their A_V vs. R trend agrees very well with an analogous study conducted by Klein et al. (1984), which employed multifrequency interferometric observations to compare the derived thermal and H α fluxes for M51, averaged into annular bins. The median value in the vK study was $\langle A_V \rangle = 1.8$, while Klein et al. obtain a mean value of $\langle A_V \rangle = 1.5$.

In examining the vK data set we have noticed a weak correlation between the HII region fluxes and their associated A_V values within the sample, with a linear correlation coefficient $b = 0.22$, and a corresponding probability of uncorrelated distributions of 0.18. For this reason, we have re-averaged the data set after weighting each A_V value with the corresponding radio continuum flux, and used the resulting mean extinction values with radius in applying corrections. In the region $R < 1'$ we have supplemented the vK data set with additional extinction measures from Jensen, Strom, and Strom (1976) which were computed from observed Balmer decrements.

Calling F the corrected flux, F' the observed flux, and $C(R)$ the correction factor with radius, we have, after scaling by 0.7 as per the Whitford reddening law for $\lambda = 6563 \text{ \AA}$,

$$F = 10^{0.7 A_V(R)/2.5} F' = C(R) F' \quad (\text{A.8})$$

The associated uncertainty in the corrected flux in our study, σ_F , using Bevington (1969, 4-12), is then given by,

$$\sigma_F = F' \langle \sigma_C(R) \rangle = F' C(R) (.7/2.5) (\ln 10) \sigma_{A_V}(R) N_R^{-1/2}. \quad (A.9)$$

Here N_R is the number of HII regions within each aperture, as determined from the catalog of 109 HII regions in M51 of Carranza et al. (1969). N_R ranges between 3 and 18 regions in each Gaussian beam, yielding an uncertainty of between 5% and 30% for the flux per aperture. In the two outer disk positions, A and B, we applied no extinction correction because an $A_V = 0$ was found by Smith (1975) at or near these locations. Observed and corrected H α brightness values for all 60 positions are given in Table 1.

We have compared our resultant extinctions with those obtained using the empirical relation between gas density and color excess in the Milky Way, developed by Bohlin, Savage and Drake (1978). Adopting their value $N(\text{HI}+\text{H}_2)/E(\text{B}-\text{V}) = 5.8 \times 10^{21} \text{ cm}^{-2} \text{ mag}^{-1}$, and $A_V/E(\text{B}-\text{V}) = 3.1$, we were able to use our derived gas densities in M51's disk to independently obtain A_V estimates with radius (c.f. DeGioia-Eastwood et al. 1984). The A_V estimates obtained in this manner agree with the results described above, within our uncertainties, but only outside of $R=60''$. Within this radius the extinctions inferred from the gas density exceed the mean value obtained from Balmer decrements by about two magnitudes. This may indicate either that the presence of heated cloud in the central region of M51 is causing an overestimation of the total hydrogen density there (Dickman, personal communication) or perhaps that a more detailed model including the consideration of the spatial distribution of HII regions

at varying optical depths is required (c.f. Talbot 1980, DeGioia-Eastwood et al. 1984).

This concludes the description of our extinction corrections. In principle, any errors in our determination of the $H\alpha$ intensities are chiefly due to possible systematic misestimation of the mean extinction over the regions 2.1 kpc in diameter. The magnitudes of these errors depend on the extent to which we are actually averaging over a statistically well behaved ensemble of HII regions and extinctions. Further evidence that the dust distribution is not clumpy on the scale of our beam comes from the infrared continuum observations of Smith (1982) taken with 49" resolution. His results show a fairly shallow and uniform falloff in dust optical depth outside the central region, thus lending support to this picture.

There remains the possibility that a class of faint HII regions exists which may be completely missed in an $H\alpha$ survey. Indeed, both the PDS and the CCD images show interarm disk regions of scale 0.5 kpc with no detected flux. We have some reassurance that a sizable portion of the $H\alpha$ emission is not being lost, in that Klein et al. found that the observed unreddened line flux could account for most of the observed thermal radio continuum flux.

iv) The Star Formation Rate Conversion

We have shown how a measurement of the $H\alpha$ flux can yield an estimate of the ionizing Lyman continuum flux from massive stars.

Given an ensemble of HII regions and their Lyman continuum flux, one can work backwards to obtain the total mass of ionizing stars (Talbot 1980; Kennicutt 1983; Gallagher, Hunter, and Tutukov 1984; Pogge and Eskridge 1987). With a knowledge of the expected lifetimes of stars as a function of mass, $\tau(M)$ in Gyr = 10^9 yr (e.g. Tutukov and Krugel 1980, henceforth TK), one may obtain the current star formation rate as described below.

The number surface density, $n(M)$ (pc^{-2}), of stars of mass M to $M+dM$ is given in terms of a massive star formation rate per area, MSFR ($M_0 \text{ pc}^{-2} \text{ Gyr}^{-1}$) and the initial mass function IMF(M) as

$$n(M) (\text{pc}^{-2}) = \text{SFR IMF}(M) \tau(M) dM. \quad (\text{A.10})$$

Here IMF(M) dM represents the number of stars formed in the mass range M to $M+dM$ per each solar mass produced, and thus is normalized such that

$$\int M \text{ IMF}(M) dM = 1 \text{ (dimensionless)} \quad (\text{A.11})$$

where the integral is taken over an assumed lower to upper mass range ($M_{\text{low}}, M_{\text{up}}$).

Following equation A.10, the total Lyman continuum flux, F_{Ly} ($\text{erg s}^{-1} \text{ pc}^{-2}$), from massive stars (mass $M > 10 M_0$), each with luminosity $L_{\text{Ly}}(M)$ (erg s^{-1}), is given by

$$F_{\text{Ly}} = \text{SFR} \int \text{IMF}(M) \tau(M) L_{\text{Ly}}(M) dM, \quad (\text{A.12})$$

with the integral is taken from $10 M_{\odot}$, where the continuum flux becomes important, to M_{up} . This may be equated to an $H\alpha$ flux ($\text{erg pc}^{-2} \text{s}^{-1}$) by

$$F_{H\alpha} = C_1 F_{Ly} = \text{SFR} \int \text{IMF}(M) \tau(M) L_{Ly}(M) dM. \quad (\text{A.13})$$

where C_1 is a constant dependent on model HII regions. Introducing a distance independent geometrical factor C_2 to convert flux, $F_{H\alpha}$ ($\text{erg pc}^{-2} \text{s}^{-1}$), to the observed brightness, $f_{H\alpha}$, ($\text{erg cm}^{-2} \text{s}^{-1} \text{arcsec}^{-2}$), we have,

$$f_{H\alpha} = C_1 C_2 \text{SFR} \int \text{IMF}(M) \tau(M) L_{Ly}(M) dM. \quad (\text{A.14})$$

Finally, this gives

$$\text{SFR} = 1/(C_1 C_2 C_3) f_{H\alpha} = C f_{H\alpha} \quad (\text{A.15})$$

with

$$C_3 = \int \text{IMF}(M) \tau(M) L_{Ly} dM, \quad (\text{A.16})$$

and $C=1/(C_1 C_2 C_3)$.

This last integral can be evaluated using a variety of methods (Huchra 1977, Kennicutt 1983; Hunter 1982; Gallagher, Hunter, and Tutukov 1984; Pogge and Eskridge 1987). We have adopted Kennicutt's results in our work because his analysis involved the manual integration of individual stellar evolutionary tracks, treating the Lyman luminosity as a function of mass and time, and accounting for mass loss which serves to increase the lifetimes of the more massive

stars. Other studies have used interpolated fits to evolutionary models or else mean values for the functions τ and L_{Ly} . The interpolated fits of TK will be useful for us in determining the effect that varying the IMF, M_{low} , and M_{up} will have on the conversion constant, C.

Using an extended Miller-Scalo IMF (see Table 15), with $M_{low}=0.1 M_{\odot}$, and $M_{up}=100 M_{\odot}$, Kennicutt obtains:

For massive stars, $M > 10 M_{\odot}$;

$$MSFR [M_{\odot} \text{ pc}^{-2} \text{ Gyr}^{-1}] = 4.71 \times 10^{15} f_{H\alpha} \cos(i), \quad (\text{A.17})$$

$$\int MSFR \text{ dA} [M_{\odot} \text{ yr}^{-1}] = 9.19 \times 10^{-43} L_{H\alpha}, \quad (\text{A.18})$$

It is a simple matter then to use the selected IMF to extrapolate the SFR to the low mass end and obtain a star formation rate conversion constant that gives the rate from M_{low} to M_{up} . For Kennecutt's parameters, we have:

$$SFR [M_{\odot} \text{ pc}^{-2} \text{ Gyr}^{-1}] = 4.54 \times 10^{16} f_{H\alpha} \cos(i) = 9.63 MSFR \quad (\text{A.19})$$

$$\int SFR \text{ dA} [M_{\odot} \text{ yr}^{-1}] = 8.92 \times 10^{-42} L_{H\alpha} = 9.63 \int MSFR \text{ dA}, \quad (\text{A.20})$$

In these formulae the galaxy's inclination, i , is important for the brightness measurements but is implicitly included in spatial integrations over a region of area A in pc^2 . It can be seen from these formulae, that the extended Miller-Scalo IMF puts about 10% of the mass of new stellar material into stars more massive than $10 M_{\odot}$.

TABLE 15
INITIAL MASS FUNCTIONS

Miller-Scalo		
	$0.354 M^{-1.4}$	$M_{1ow} < M < 1 M_0$
$IMF(M) = f_1(M_{1ow}, M_{up}) \times$	$0.354 M^{-2.5}$	$1 M_0 < M < 10 M_0$
	$2.231 M^{-3.3}$	$10 M_0 < M < M_{up}$

Extended Miller-Scalo		
	$1.0 M^{-1.4}$	$M_{1ow} < M < 1 M_0$
$IMF(M) = f_2(M_{1ow}, M_{up}) \times$	$1.0 M^{-2.5}$	$10 M_0 < M < M_{up}$

Salpeter		
$IMF(M) = f_3(M_{1ow}, M_{up}) \times$	$1.0 M^{-2.35}$	(all M)

Jensen, Talbot, and Dufour (1981)

	$0.175 M^{-1.6}$	$M_{1ow} < M < 1.8 M_0$
$IMF(M) = f_4(M_{1ow}, M_{up}) \times$	$0.272 M^{-2.35}$	$1.8 M_0 < M < M_{up}$

The functions, $f_{1-4}(M_{1ow}, M_{up})$, provide normalization such that $\int IMF(M) M dM = 1$, integrated from M_{1ow} to M_{up} . The constant coefficients listed above serve to make the functions continuous.

The fact that the conversion factor is fairly insensitive to the upper mass limit, M_{up} , in equation A.19 is shown in Figure 21. Here we display the normalized logarithm of the terms of equation A.16 along with the normalized logarithm of their product $[\tau(M) L_{Ly}(M) IMF(M)]$. The forms for $\tau(M)$ and $L_{Ly}(M)$ are from the interpolated fits of TK (and references therein) with the Lyman continuum luminosities taken by these authors from nongray atmospheric models. The IMF used is an extended Miller-Scalo function. We see that the stellar contribution, per mass interval, to the total Lyman continuum flux (labeled "Product" in Figure 21) falls off after $M=40 M_{\odot}$ with increasing stellar mass, dropping to -0.5 dex (1/3) of this value by $90 M_{\odot}$. The point here is that the IMF weighted continuum emission drops off per interval of stellar mass after $40 M_{\odot}$, making the conversion factor, C , insensitive to the upper mass cutoff M_{up} . We see also in this figure the dramatic drop in Lyman continuum flux for stars less massive than $15 M_{\odot}$.

We have used the functional forms of TK for τ and L_{Ly} to find the conversion factors for different IMFs and mass ranges. In Figures 22 and 23 we trace the variation in C with M_{up} and M_{low} , respectively, for the four IMFs given in Table 15. The Miller-Scalo IMF, with its steeply declining high-mass end, is seen to yield a conversion factor about three times larger than that of the other IMFs. This is due to the fact that with this IMF, the $H\alpha$ flux is accredited to lower mass stars which are less efficient in producing L_{Ly} continuum flux. All of the IMFs yield higher conversion factors for smaller values of M_{up} for

Figure 21. The terms used in computing the star formation rate conversion factor, C. The IMF used is the extended Miller-Scalo function (Table A.1) with $M_{\text{low}} = 0.1 M_{\odot}$ and $M_{\text{up}} = 100 M_{\odot}$. All values are normalized to 1 at $M = 35 M_{\odot}$, and the term labeled Product is $(\text{IMF}(M) \tau(M) L_{\text{Ly}}(M))$, which is the Lyman continuum contribution per mass interval.

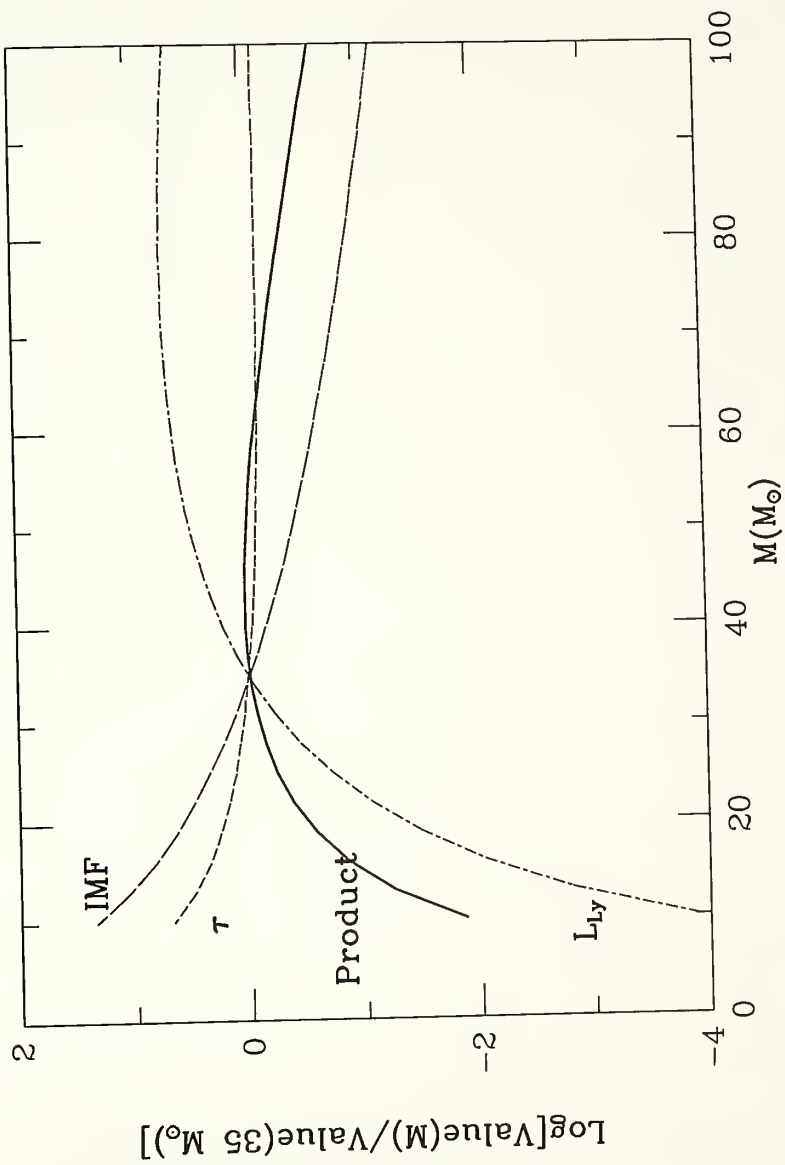


Figure 22. The conversion factor, C , against the high-mass cutoff for four initial mass functions. C is measured in units of $M_{\odot} \text{ Gyr}^{-1} \text{ pc}^{-2} / (\text{erg cm}^{-2} \text{ s}^{-1} \text{ arcsec}^{-2})$. The low-mass cutoff is held at $0.1 M_{\odot}$. The power-law falloff of the each IMF results in little relative contribution of $\text{H}\alpha$ flux from very massive stars.

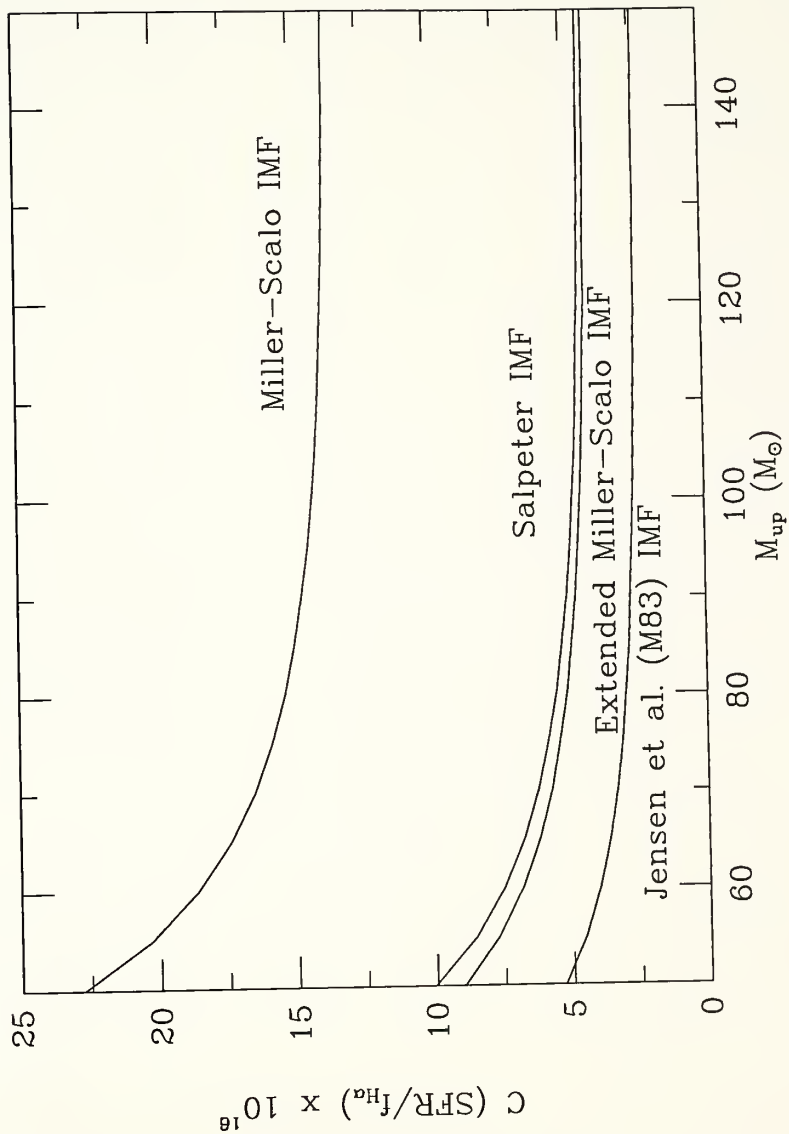
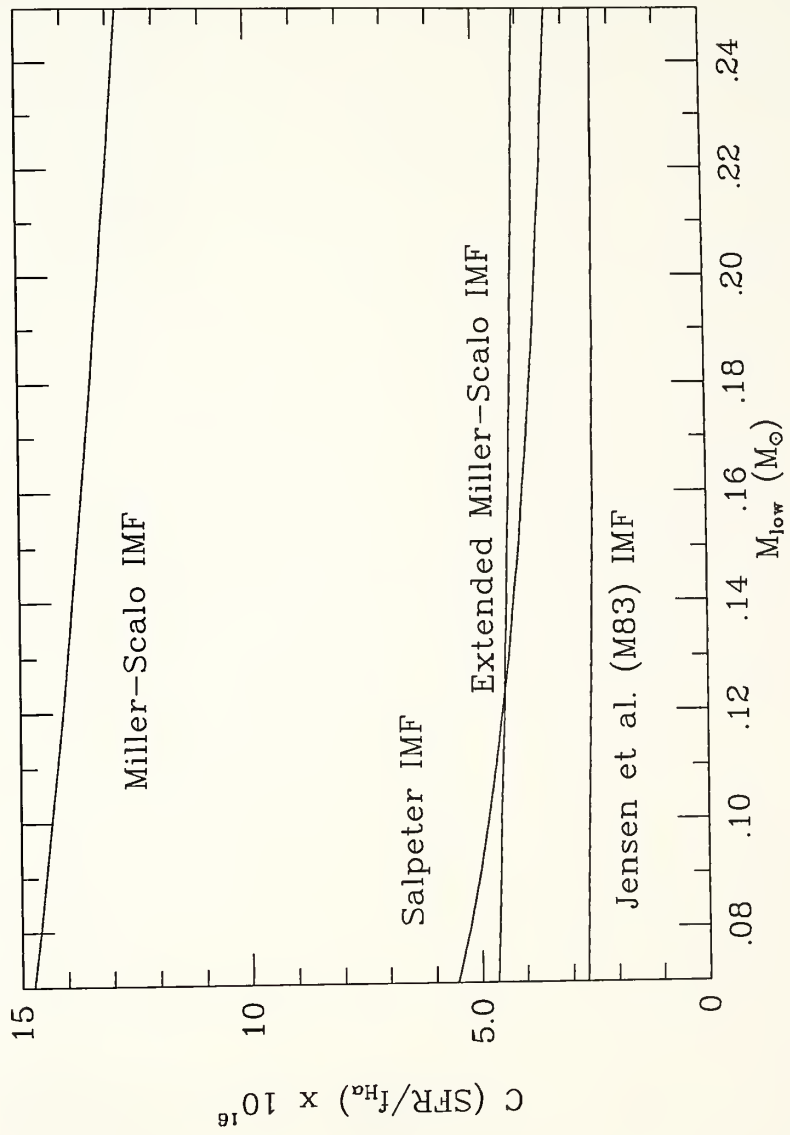


Figure 23. The conversion factor, C , against the low-mass cutoff for four initial mass functions. The high-mass cutoff is held at $100 M_{\odot}$. The conversion factors are relatively insensitive to the low-mass cutoff.



this same reason. The IMF functions of Figure 23 are seen to give conversion factors which are fairly insensitive to variations in $M_{1\text{low}}$. The Salpeter and Miller-Scalo functions give slightly larger conversion factors for a lower cutoff value in part because the normalization of these functions places more mass into the same inefficient L_{Ly} stars discussed above. Figures 24 and 25 show the fraction of the newly formed stellar mass which goes into high mass stars for each IMF and $M_{1\text{low}}$, M_{up} limits. The multiplication of a selected conversion factor, C , by the fraction shown in Figures 24 and 25 will recover the conversion factor to high mass stars ($M > 10 M_{\odot}$) alone. Again, it can be seen in these figures that varying M_{up} or $M_{1\text{low}}$ will not have a very strong effect on the number of solar masses going into massive star formation for a particular IMF. The important result of this analysis is that the choice of the particular power-law IMF is crucial in determining the star formation rates, while the choice of mass range has a much smaller effect, so long as M_{up} is above about $60 M_{\odot}$. Finally, we must caution that the uncertainty in these results grows with M_{up} , since there is little observational data above $M=30 M_{\odot}$ with which to constrain the evolutionary models.

v) Choice of an Initial Mass Function

We wish to select an appropriate initial mass function to use in converting $H\alpha$ fluxes to star formation rates. We have taken note that the relative values of the global $H\alpha$ equivalent width (EW) and the (B-V) color of a galaxian disk can serve as a sensitive discriminator

Figure 24. The fraction of total mass in high mass stars against high-mass cutoff for four initial mass functions. The low-mass cutoff is held at $0.1 M_{\odot}$.

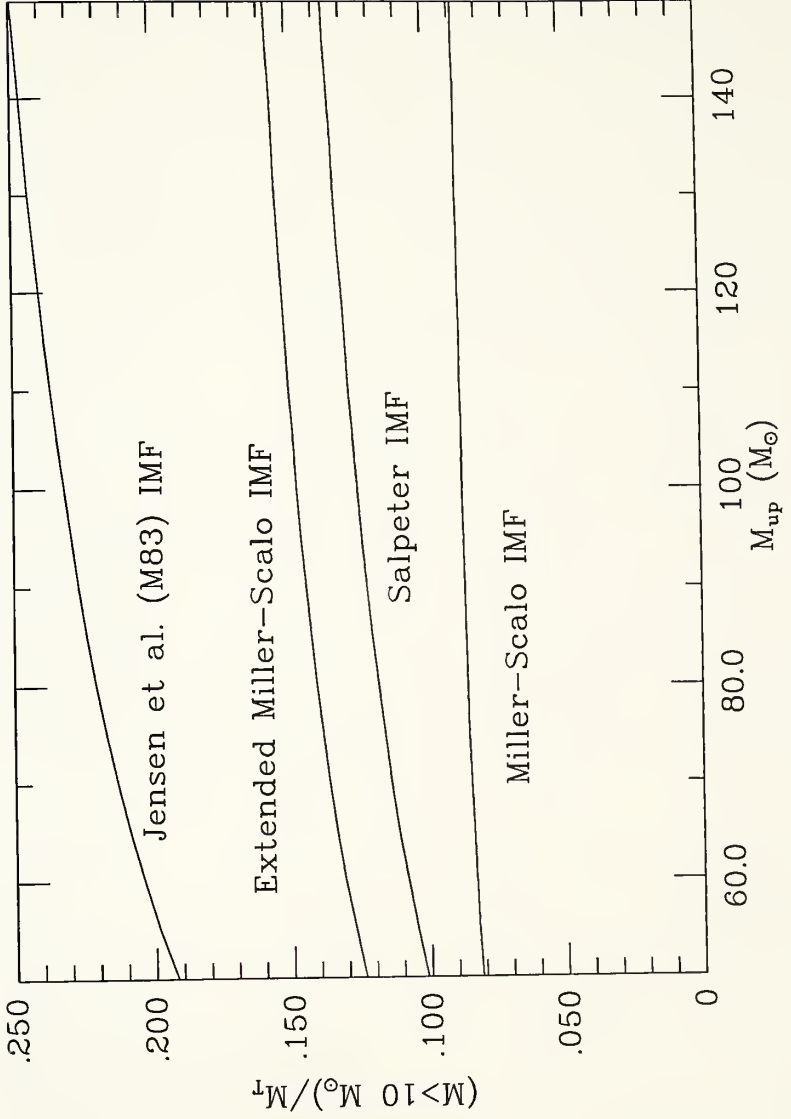
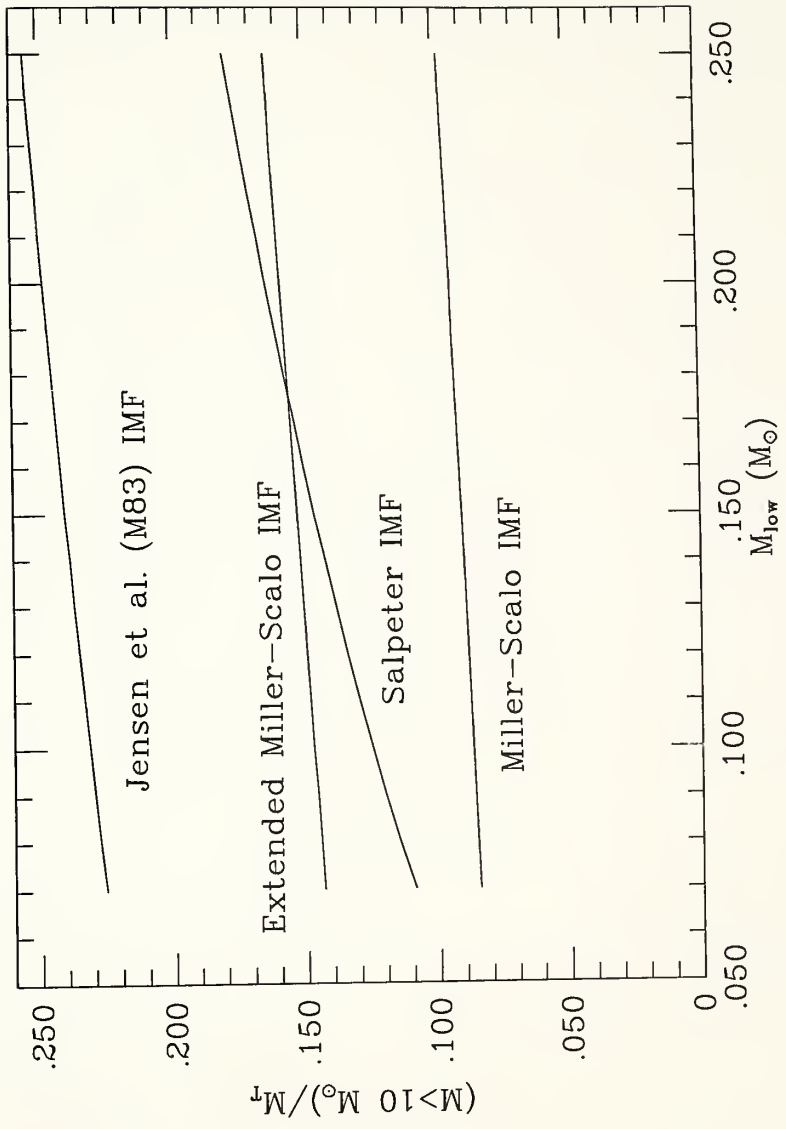


Figure 25. The fraction of total mass in high mass stars against low-mass cutoff for four initial mass functions. The high-mass cutoff is held at $100 M_{\odot}$.



between various IMFs as shown by Kennicutt (1983). In this study, the color and H α emission evolution were estimated for model galaxies using different IMFs and different star formation rate dependencies on time. The model disks were evolved for 15×10^9 yrs under the assumptions of linearly increasing, constant, and various exponentially decreasing star formation rates. A range of final EW and (B-V) colors resulted, and are represented by curves on the EW-color diagram (Figure 26, reproduced from Kennicutt 1983). The advantage of comparing the H α EW with the (B-V) colors is that the results for a particular IMF (due to its slope between $30 M_{\odot}$ and $60 M_{\odot}$) are distinct. The three regions in this figure represent: a "shallow IMF", $\text{IMF}(M) \sim M^{-2}$, top curve; the Salpeter-like "extended Miller-Scalo IMF", $\text{IMF}(M) \sim M^{-2.5}$, middle curve; and the Miller-Scalo IMF, $\text{IMF}(M) \sim M^{-3.3}$, lower curve. The extension of each curve across the EW-color diagram is due to the various star formation rate histories assumed for the model disks; those with increasing star formation rates appearing on the left (blue) side and disks with no remaining star formation appearing on the right (red) side. The points on this figure are from the measured global (B-V) T_0 colors (de Vaucouleurs, de Vaucouleurs, and Corwin 1976), and the EW(H α +N[II]) values (Kennicutt and Kent 1983). The colors and EW values are not corrected for extinction, but because the red and H α flux are measured from the same wavelength band, the equivalent widths may be extinction-independent. This will not be the case, however, if extinction is preferentially present in the sites of new star formation, e.g., dusty HII regions. The hatched regions in this

Figure 26. Initial mass function discrimination method. Reproduced from Kennicutt (1983). The three shaded areas represent model disk galaxy colors corresponding to different IMFs. The lower region is the steep Miller-Scalo IMF; the central region is the extended Miller-Scalo IMF; the upper region is a shallow IMF (exponent of -2). Superposed are the observed parameters for 120 disk galaxies, with M51 indicated.

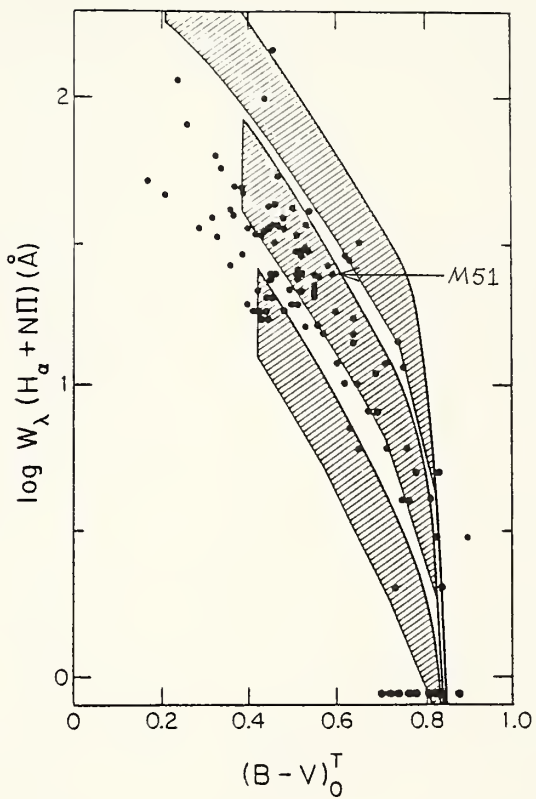


figure take into account this effect, with the lower bound in each region corresponding to an A_V of 1.2 affecting just the $H\alpha$ emission.

Most of the 120 disk galaxies examined show colors that are inconsistent with the Miller-Scalo IMF and the shallow IMF, but are consistent with the extended Miller-Scalo IMF. The position of M51, with values $EW(H\alpha+[NII])= 24 \text{ \AA}$, and $(B-V)^T_0 = 0.6$ is indicated in this figure and is seen to be consistent with the extended Miller-Scalo function. We should add that Kennicutt used his IMF discrimination method in a statistical treatments of large numbers of galaxies, and not for the characterization of a individual disk. One obstacle in applying the method to an individual disk is the problem of knowing the mean extinction, an obstacle we believe has been surmounted here.

We have adopted the extended Miller-Scalo IMF, and use the conversions given in equations A.17-A.21. An important remaining question is the validity of applying this global value to individual regions within the disk. We cannot rule out the possibility that the spiral density wave may be responsible for the production of a different IMF, i.e., one biased more toward the massive end than is found in interarms regions in M51. The difficulty in determining local departures from a global IMF can scarcely be exaggerated. Apart from actually counting stars of various spectral types (an impractical procedure here) no method has been devised to indirectly infer a local IMF. The difficulty originates from three sources. First, it is an unhappy fact that the major contribution of low mass stars, $M < 1 M_\odot$,

is simply their mass. The colors of any particular galaxian region are dominated by stars of mass greater than $1 M_{\odot}$. Secondly, in attempting to discern color differences on the spiral arms caused by the relative abundance of stars of mass $1 M_{\odot} - \sim 100 M_{\odot}$, we must first be able to separate out the contribution of any enhanced stellar number density of old stars due to the compressive action of the spiral density wave. Various stellar types, each possessing an intrinsic mean velocity dispersion, are expected to respond to the spiral density wave differently, compounding the problem. Finally, as Equation A.10 indicates, the stellar distribution at any location is dependent on the past star formation rate there, as well as the IMF. The presence of HII regions arranged along the spiral arms indicates that the arms are sites of recent enhanced star formation. A 50% enhancement in the SFR, lasting $10^7 - 10^8$ yr can dramatically alter the (U-B), (B-V) colors and the $H\alpha$ and $H\beta$ equivalent widths, as has been shown by the composite (steady state plus burst) models of Huchra (1977). The SFR(t) and IMF terms are not easily separated when SFR(t) is non-monotonic and largely unknown. For these three reasons, color differences between the arms and interarms are difficult to uniquely interpret.

With this restriction in mind, we briefly review investigations of the arm colors in M51. Two studies (Schweizer 1976; Burkhead 1977) have looked for a color gradient across the spiral arms in M51 which might indicate the reddening of newly formed clusters as they age while moving downstream. In these studies the spiral arms (A) were seen to

be slightly bluer than the interarms (IA), with $(B-O)_{IA}=1.01$ and $(B-O)_A=0.76$ (Schweizer 1976) and maximum departures of $(B-V)_{IA}=0.75$, $(B-V)_A=0.5$, $(U-V)_{IA}=-0.5$, $(U-V)_A=0.0$ (Burkhead 1977, at Northeast arm region "G"). However, no spatial color gradients were detected. In these studies, at many locations, the arms were found to be almost uniformly more luminous than the interarms at all wavelengths, an effect which Schweizer accredits to density enhancements of the old stellar disk. Similarly, in a comparison of the I-band and B-band intensities at 20 arm and interarm locations in M51, Elmegreen and Elmegreen (1984) found that about half of these locations maintained a B/I intensity ratio of 1.5 ± 0.2 while the remaining half had a B/I ratio near unity, $B/I=1.0 \pm 0.2$. Again, the conclusions of this study was that the enhancement in stellar number density was producing the majority of the arm light, and not the new stellar populations. None of these studies were able to overcome the difficulties in determining a local IMF listed above.

We are then left with two areas of uncertainty regarding the initial mass function in M51. The first is whether a spatially variable IMF could simulate the result that the total star formation rates are higher on M51's arms than its interarms, and the second is whether a spatially variable IMF could simulate the result that the massive star formation rate is higher on the arms. The answer to the first question is yes, but only if the spiral arm IMF entails a low mass cutoff or slope which generally excludes the formation of low mass

$M < 1 M_{\odot}$ stars. The answer to the second question is yes as well, but only if the IMF on the arms is highly skewed to star of mass $15 M_{\odot} - 30 M_{\odot}$, i.e., efficient L_{Ly} producers. Such an effect is suggested by Silk (1986), who argues that the action of the spiral density wave is to build up clouds sufficiently massive to produce O and B stars. These stars in turn heat the clouds, and under such conditions the critical mass required for collapse is raised, further favoring massive star formation and thus establishing a feedback mechanism. We point out that this scenario is one of enhanced massive star formation, the only question being if the mechanism is capable of skewing the IMF to such high masses that our calculation of the total number of solar masses produced is overestimated. If this model turns out to be correct (there is still very little observational evidence) the result of efficient massive star production on M51's spiral arms remains valid as a qualitative assertion.

e) Summary

We have discussed the methods and uncertainties involved in deriving H_2 surface densities from CO intensities and star formation rates from $H\alpha$ brightness measurements. While the sources of possible error are plentiful, what stands out in this discussion is the direction these uncertainties take. The conversion to H_2 surface densities assumes that a mean radiation temperature (10 K) applies to ensembles of molecular clouds, and that the cloud virial mass ($M_{vir} \sim \Delta v^2 \ell$) represents the true mass. If clouds in a region are

hotter than we have supposed or have a larger velocity dispersion (e.g. due to star formation events such as cloud collisions or stellar winds) then we will have overestimated the cloud masses and the H_2 surface densities. Star formation rates, on the other hand, are very prone to underestimation, for the variety of reasons given. We have seen why it is difficult to overestimate the ionizing flux from massive stars, but very easy to underestimate it. Our estimates of L_{Ly}/M_{H_2} are therefore lower limits.

To convert the Lyman luminosity to total star formation rates, we have used an extended Miller-Scalo IMF for M51, and have given evidence that the use of this IMF is appropriate, at least on a global scale. That the IMF is spatially constant on a local scale is given some support by the small color variations across the disk, but this observation in no way constitutes a proof. If there exists a dramatic shift of the IMF range and/or slope between the arms and interarms, our relative values for the massive star formation rates and efficiencies could be wrong. These values could be overestimated on the arms, for example, if the arm clouds preferentially produce stars of mass $M > 20 M_{\odot}$.

We list below our results in order of increasing uncertainty:

- 1) The result that the production of ionizing stellar emission per nucleon of gas on the arms is higher than on the interarms seems firm.

- 2) The result that the MSFE on the arms is higher than on the interarms seems likely. An alternative explanation is the selective production of higher mass stars (as opposed to more total mass in high mass stars) on the arms. To check this possibility, a determination of the effective temperature of the exciting stars in on-arm and off-arm regions might be attempted.

- 3) The extrapolation of the above result to total SFEs is very uncertain because it difficult to distinguish between newly formed low mass stars on the arms and those present due to the action of the spiral density wave. It might be possible to remedy this by measuring the $H\alpha$ equivalent widths of and red light contribution from on-arm and off-arm HII regions, after first subtracting off the red disk and "old red arm" light.

APPENDIX B

A MASS INFALL MODEL FOR M51

a) Introduction

Here we are interested in critically examining the result that, over the disk of M51, $SFE > SFE_e$, where the former term is the current SFE, and the latter term is the empirical value inferred from the current gas density and total star formation rate averaged over the galaxy's lifetime. Our concern is important in that, if SFE is indeed larger than SFE_e , this might indicate that the galaxy is currently engaged in a "burst" of star formation.

We have discussed in Appendix A the various errors that could contribute to a misestimation of the observed SFE. In §IVe we found that the error in $SFE = SFR / \alpha_p$ would have had to be an overestimate by a factor of over 3 to bring the SFE into agreement with with the SFE_e . Because of H α extinction uncertainties and related factors, the inferred SFRs are most likely to be underestimated. Also, the α_p values obtained from the I $_{CO}$ intensities are most likely to be overestimates if the mean cloud radiation temperature is elevated in regions heated by newly formed stars, as discussed in Appendix A. Both of these trends are in the wrong direction to align SFE with SFE_e . The highest uncertainty in computing the SFE values originates in converting the Lyman continuum flux to a star formation rate. Errors could arise variously from incorrect assumptions regarding the IMF

slope, the upper mass cutoff, and the spatial consistency of the function. If, as suggested by Shu, Adams, and Lizano (1987), and Scoville et al. (1986), the IMF is weighted to the high mass end on spiral arms, then the SFR could be overestimated in the $\langle \text{SFR}(R) \rangle$ averages. We can not dismiss this possibility, but for the moment, we ignore it, and ask if the SFE_e measurements could be underestimated, and if by altering the assumptions that went into their formulation, we can bring the SFE_e and SFE values into agreement.

Specifically, our SFE_e values may be underestimates because we have ignored gas infall over the lifetime of the galaxy. The star formation efficiency could have been higher than SFE_e throughout the past because, while we correctly estimate the total mass of stars created, we overestimate the density of gas from which they form by including in $\sigma_p(t)$ the future infall gas mass. In the following treatment, we compute constant infall rates which will bring the SFE_e 's into agreement with the observed SFEs.

b) Formulation

Following Talbot (1980), we call v_e the constant SFE, such that, in the absence of infall the rate of change of the gas surface density in time, $\sigma_p(t)'$, may be related to the rate of new star formation as:

$$\sigma_p(t)' = -(1-f)v_e\sigma_p(t), \quad (\text{B.1})$$

where f is the fraction of material recycled back to the ISM. If we consider this process over the age of the galaxy, where t goes from

zero to the present time, this leads to

$$\sigma_p(t) = \sigma_T \exp[-(1-f)\nu_e t] \quad (\text{B.2})$$

$$\nu_e = 1/[T(1-f)] \ln(\sigma_T/\sigma_p) \quad (\text{B.3})$$

where T is the galaxy's age and $\sigma_T = \sigma_p(0)$ is the total density, stars and gas, and ν_e is the empirical time averaged SFE measured in Gyr^{-1} .

In the presence of a constant infall in time, σ_{1n}' (where the prime denotes a time derivative) with units $M_\odot \text{pc}^{-2} \text{Gyr}^{-1}$, the differential equation becomes:

$$\sigma_p(t)' = -(1-f)\nu \sigma_p(t) + \sigma_{1n}' \quad (\text{B.4})$$

with

$$\sigma_T(t) = \sigma_p(0) + \sigma_{1n}' t. \quad (\text{B.5})$$

The solution is

$$\sigma_p(t) = \sigma_{1n}' \tau + (\sigma_p(0) - \sigma_{1n}' \tau) \exp(-t/\tau) \quad (\text{B.6})$$

where $\tau = 1/[(1-f)\nu]$.

Here we have left off the subscript to ν , so that we may use the observed SFE as ν , and compare it with the $\nu_e = 1/[T(1-f)] \ln[\sigma_T(T)/\sigma_p(T)] = \text{SFE}_e$ values obtained in §IVd. The goal here is to find $\sigma_p(0)$, σ_{1n}' values that will yield both our observed ν and our empirical ν_e values consistently. Setting $\sigma_T(T)$, $\sigma_p(T)$, and τ from §IVe, and with $t=T$, we have two equations, B.5 and B.6, and two unknowns, $\sigma_p(0)$, and σ_{1n}' .

We show the solutions in Table 16 for the two cases, $T=10$ Gyr, and $T=15$ Gyr. In each case we also show $\sigma_{\text{in}}'T/\sigma_T(T)$, which is the fraction of total current density which has arrived via infall in this model.

The required infall rates, $16-70 M_{\odot} \text{pc}^{-2} \text{Gyr}^{-1}$, are much too high to make the model plausible. The galaxy would have to accrete one to three times its original mass over its lifetime, and such reserves of gas are not apparent nearby. While there do exist peripheral HI clouds surrounding the NGC 5194/5195 system (Haynes, Giovanelli and Burkhead 1978, A. Rots 1985, personal communication), the total outlying HI mass is put at $\sim 10^8 M_{\odot}$ (Haynes *et al.* 1978), which is three orders of magnitude too low for the required constant infall per Gyr. Furthermore, tidal interaction most likely causes outward streaming, with each passage of the companion producing the various components of the plumes and debris clouds seen. We therefore discount gas infall as an insufficient means with which to account for the observed difference between the time averaged SFE_e and the currently observed SFE.

TABLE 16 (NOTES)

The infall models for two galaxian ages, 10×10^9 yrs and 15×10^9 yrs. The purpose of the models is to produce the currently measured values $\sigma_T(T)$, $\sigma_p(T)$, SFE, and SFE_e via infall so that there is no contradiction implied by $SFE \neq SFE_e$.

Row (1) $\sigma_T(T)$ is the total disk surface density (stars and gas).

Row (2) $\sigma_p(T)$ is the gas surface density.

Row (3) SFE is the observed quantity $SFR/\sigma_p(T)$.

Rows (4,9) T is the current age of the galaxy.

Rows (5,10) σ_{in}' is the constant gas infall rate, from time $t=0$ to $t=T$.

Rows (6,11) $\sigma_p(0)$ is the initial disk density, assumed to be entirely gaseous.

Rows (7,12) $\sigma_{in}'T/\sigma_T(T)$ is the fraction of current total disk density acquired through infall.

Rows (8,13) SFE_e is the empirical star formation efficiency for the non-infall case, $SFE_e = [T(1-f)]^{-1} \ln(\sigma_T(T)/\sigma_p(T))$, where T is given in row 4 and 9, and f is set at 0.2.

TABLE 16
GAS INFALL MODEL RESULTS

Row	R_{gal} (arcsec)	30	36	42	52	56	69	95	141
(1)	$\sigma_T(T)$ ($M_\odot \text{ pc}^{-2}$)	1380	1098	862	677	599	531	369	250
(2)	$\sigma_p(T)$ ($M_\odot \text{ pc}^{-2}$)	209	178	161	129	108	83	59	44
(3)	$SFE_e = v$ (Gyr^{-1})	0.41	0.42	0.42	0.33	0.36	0.33	0.36	0.48
(4) $T=10$ Gyr									
(5)	σ_{in}' ($M_\odot \text{ pc}^{-2} \text{ Gyr}^{-1}$)	63	56	52	30	28	17	14	16
(6)	$\sigma_p(0)$ ($M_\odot \text{ pc}^{-2}$)	754	537	344	376	322	359	226	86
(7)	$\sigma_{in}'T / \sigma_T(T)$	0.4	0.5	0.6	0.4	0.5	0.3	0.4	0.6
(8)	$SFE_e = v_e$ (Gyr^{-1})	0.24	0.24	0.23	0.21	0.22	0.24	0.24	0.23
(9) $T=15$ Gyr									
(10)	σ_{in}' ($M_\odot \text{ pc}^{-2} \text{ Gyr}^{-1}$)	68	60	54	34	31	22	17	17
(11)	$\sigma_p(0)$ ($M_\odot \text{ pc}^{-2}$)	355	200	53	162	135	206	118	0
(12)	$\sigma_{in}'T / \sigma_T(T)$	0.7	0.8	0.9	0.8	0.8	0.6	0.7	1.0
(13)	$SFE_e = v_e$ (Gyr^{-1})	0.16	0.16	0.15	0.14	0.15	0.16	0.16	0.15

APPENDIX C

EXCESS EMISSION DIAGRAMS FOR M51

Figures 27 to 29 show the I_{CO} , $f_{\text{H}\alpha}$ and SFE excesses above the radial average in M51. The CO and H α data from each of the 57 positions from $R_{\text{gal}} = 45''$ to $160''$ was interpolated to give a smooth distribution for each parameter. At each $2''$ interval in R_{gal} the azimuthal mean value of each parameter was computed. The mean value was first subtracted from the parameter at each $2''$ by $2''$ position, and then divided into the result, yielding the fractional excess, F_{ex} , from the mean emission, $\langle E \rangle$, at each point; $F_{\text{ex}} = (E - \langle E \rangle) / \langle E \rangle$. The excess SFE was obtained by first dividing the interpolated H α and CO maps, and then applying this procedure. In each figure the inner dust lanes of the spiral arms are traced. The method outlined has the difficulty that one arm can suppress the other by raising the mean above the true interarm intensity. The arm in the West in these figures is suppressed in this way in the H α map. Evident in all three figures are the bright Northeast and Southwest complexes.

Figure 27. The fractional CO emission above the azimuthal mean in M51.
Contours are 0.0, 0.3, and 0.6.

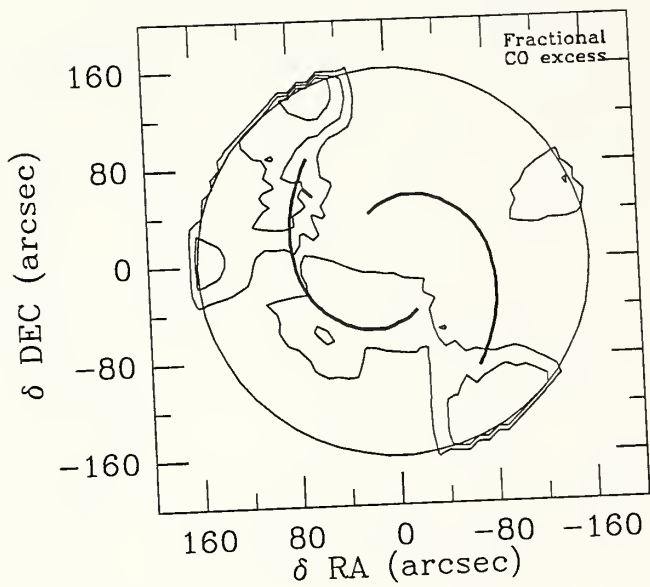


Figure 28. The fractional H α emission above the azimuthal mean in M51. Contours are from 0.3 to 1.9, spaced by 0.3.

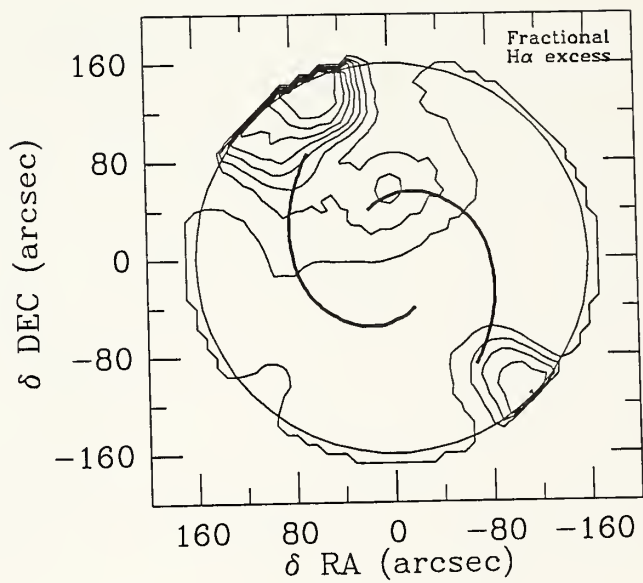
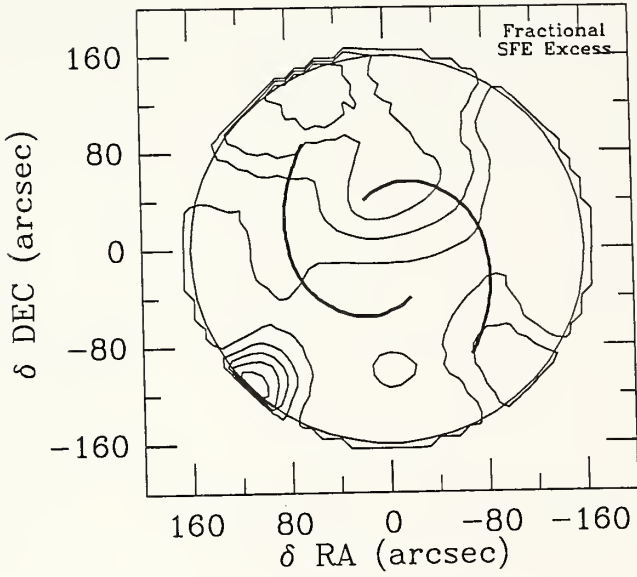


Figure 29. The fractional SFE above the azimuthal mean in M51.
Contours are from -0,2 to 1.4, spaced by 0.4.



BIBLIOGRAPHY

- Allen, R.J., Atherton, P.D. and Tilanus, R.P.J. 1986, Nature, 319, 296.
- Ables, H.D. 1971, Pub. US Naval Obs., Series II, Vol. 20, Part 4.
- Bash, F.N. 1979, Ap. J., 233, 524.
- Bash, F.N. and Peters, W.L. 1976, Ap. J., 205, 786.
- Bevington, P.R. 1969, Data Reduction and Error Analysis for the Physical Sciences, (New York: McGraw-Hill).
- Bloemen, J.B.G.M., Caraveo, P.A., Hermsen, W., Lebrun, F., Maddalena, R.J., Strong, A.W. and Thaddeus, P. 1984, Astr. Ap., 139, 37.
- Bloemen, J.G.B.M, Strong, A.W., Blitz, L., Cohen, R.S., Dame, T., Gabelsky, D.A., Hermen, W., Lebrun, F., Mayer-Hasselwander, H.A. and Thaddeus, P. 1986, Astr. Ap., 154, 25.
- Bohlin, R.C., Savage, B.D. and Drake, J.F. 1978, Ap. J., 224, 132.
- Bohlin, R.C., Cornett, R.H., Hill, J.K., Smith, A.M. and Stecher, T.P. 1983, Ap. J. Let., 274, L53.
- Boroson, T. 1981, Ap. J. Suppl., 46, 177.
- Brinks, E. 1984, Ph.D. dissertation, Leiden University.
- Burkhead, M.S. 1978, Ap. J. Suppl., 38, 147.
- Garranza, G., Crillon, R. and Monnet, G. 1969, Astr. Ap., 1, 479.
- Clemens, D.P. 1985, Ap. J., 295, 422.
- Combes, F., Encrenaz, P.J., Lucas, R. and Wellichew, L. 1977a, Astr. Ap., 55, 311.
 ----- 1977b, Astr. Ap., 61, L7.
 ----- 1978, Astr. Ap., 67, L13.
- Comte, G. 1981, Astr. Ap. Suppl., 44, 441.
- Davis, J.H. and Vanden Bout, P. 1973, Ap. J., 15, 43.
- DeGioia-Eastwood, K. 1982, Ph.D. dissertation, University of Wyoming.
- DeGioia-Eastwood, K., Grasdalen, G.L., Strom, S.E. and Strom, K.M. 1984, Ap. J., 278, 564.

- de Vaucouleurs, G., de Vaucouleurs, A. and Corwin, H.C. 1976, Second Reference Catalogue of Bright Galaxies, (Austin: University of Texas Press).
- de Vaucouleurs, G. 1979, A.J., 84, 9.
- de Vaucouleurs, G., Pence, W.D. and Davoust, E. 1983, Ap. J. Suppl., 53, 17.
- Devoust, E. and de Vaucouleurs, G. 1980, Ap. J., 242, 30.
- Dickman, R.L. 1978, Ap. J. Suppl., 37, 407.
- Dickman, R.L., Snell, R.L. and Schloerb, F.P. 1986, Ap. J., 309, 326 (DSS).
- Dopita, M.A. 1985, Ap. J. Let., 295, L5.
- Dufour, R.J., Talbot, R.J., Jensen, E.B., and Shields, G.A. 1980, Ap. J., 236, 119.
- Elmegreen, D.M. and Elmegreen, B.G. 1984, Ap. J. Suppl., 54, 127.
- Elmegreen, B.G. 1987, IAU Symposium No. 115, Star Forming Regions, eds. M. Peimbert and J. Jugaku, (Reidel), in press.
- Ford, H., Crane, P., Jacoby, G., Lawrie D. and van der Hulst, J.M. 1985, Ap. J., 293, 132.
- Gallagher, J.S., III, Hunter, D.A. and Tutukov, A.V. 1984, Ap. J., 284, 544.
- Goad, J.W., De Veny, J.B. and Goad, L.E. 1979, Ap. J. Suppl., 39, 439 (GDG).
- Goad J.W. and Gallagher, J.S. 1985, Ap. J., 297, 98.
- Gusten, R. and Mezger, P.G. 1982, Vistas in Astronomy, 26, 159 (GM).
- Haynes, M.P., Giovanelli, R. and Burkhead, M.S. 1978, A. J., 83, 938.
- Hodge, P.W. and Kennicutt, R.C. 1983, A. J., 88, 296.
- Huchra, J.P. 1977, Ap. J., 217, 928.
- Hunter, D.A. 1982, Ap. J., 260, 81.

- Hunter, D.A., Gallagher, J.S. and Rautenkranz 1982, Ap. J. Suppl., 49, 53.
- Jensen, E.B. 1977, Ph.D. dissertation, University of Arizona.
- Jensen, E.B., Strom, K.M. and Strom, S.E. 1976, Ap. J., 209, 748.
- Jensen, E.B., Talbot, R.J., Jr. and Dufour, R.J. 1981, Ap. J., 243, 716 (JTD).
- Julian, W.H. and Toomre, A. 1966, Ap. J., 146, 810.
- Kenney, J.D. 1987, Ph.D. dissertation, University of Massachusetts.
- Kenney, J.D. and Taylor, D.K. 1987, FCRAO Report, in preparation.
- Kennicutt, R.J., Jr. 1981, A. J., 86, 1847.
----- 1983, Ap. J., 272, 54.
- Kennicutt, R.J., Jr. and Kent, S.M. 1983, A. J., 88, 1094.
- Kimura, T. and Tosa, M. 1985, Publ. Astron. Soc. Japan, 37, 669.
- Klein, U., Wielebinski, R. and Beck, R. 1984, Astr. Ap., 135, 213.
- Kormendy, J. and Norman, C.A. 1979, Ap. J., 233, 539.
- Kwan J. and Valdez F. 1987, Ap. J., April 1987 (KV).
- Larson, R.B. 1981, M.N.R.A.S., 194, 809.
----- 1986, M.N.R.A.S., 218, 409.
- Lo, K.Y., Berge, G., Claussen, M., Heiligman, G., Keene, J., Masson, C., Phillips, T., Sargent, A., Scoville, N., Scott, S., Watson, D. and Woody, D. 1984, in U.R.S.I. Symposium on Millimeter and Sub-millimeter Wave Astronomy, ed. J. Gomez-Gonzales, (Granada:U.R.S.I.).
- Lo, K.Y., Ball, R., Masson, C.R., Phillips, T.G., Scott, S., Woody, D.P. 1987, Ap. J., (in press).
- Mathewson, D.S., van der Kruit, P.C. and Brouw, W.N. 1972, Astr. Ap., 17, 468.
- Morris, M. and Rickard, L.J. 1982, Ann. Rev. Astr. Ap., 20, 517.
- Mountain, C.M., Hawarden, T.G., Joseph, R.D. and Leggett, S.K. 1987, IAU Symposium No. 115, Star Forming Regions, eds. M. Peimbert and J. Jugaku, (Reidel), in press.

- Nelson, A.H., Johns, T. and Tosa, M. 1985, in IAU Symposium No. 106, The Milky Way, eds. H. van Woerden, R.J. Allen and W.B. Burton, (Dordrecht:Reidel).
- Onrechen, M.P. 1985, Ph.D. dissertation, University of Minnesota.
----- 1985a, A. J., 90, 1474.
- Osterbrock, D.E. 1974, Astrophysics of Gaseous Nebulae, (San Francisco: Freeman).
- Pastoriza, M.G. 1975, Ap. Space Sci., 33, 173.
- Penzias A.A. and Burrus, C.A. 1973, Ann. Rev. Astr. Ap., 11, 51.
- Pogge, R.W. and Eskridge, P.B. 1987, A. J., 92, 291.
- Reynolds, R.J. 1984, Ap. J., 282, 191.
- Rickard, L.J., Palmer, P., Morris, M., Zuckerman, B. and Turner, B.E. 1975, Ap. J. Let., 199, L75.
- Rickard, L.J. and Palmer, P. 1981, Astr. Ap., 102, L13.
- Rickard, L.J. and Blitz, L. 1985, Ap. J. Let., 292, L57.
- Roberts, W.W. 1969, Ap. J., 167, 7.
- Roberts, W.W., Jr., Huntley, J.M. and van Albada G.D. 1979, Ap. J., 233, 67.
- Rumstay, K.S. and Kaufman, M. 1983, Ap. J., 274, 631.
- Rydbeck, G., Hjalmarson, Å. and Rydbeck, O.E.H. 1985, Astr. Ap., 144, 282 (RHR).
- Ryden, B.S. and Stark, A.A. 1986, Ap. J., 305, 823.
- Salpeter, E.E. 1955, Ap. J., 137, 758.
- Sandage, A. and Tammann, G. 1975, Ap. J., 196, 313.
- Sanders, R.H. and Tubbs, A.D. 1980, Ap. J., 235, 808.
- Sanders, D.B. 1981, Ph.D. dissertation, State University of New York at Stony Brook.
- Sanders, D.B., Solomon, P.M. and Scoville, N.Z. 1984, Ap. J., 276, 182 (SSS).

- Sanders, D.B., Scoville, N.Z. and Solomon, P.M. 1985, Ap. J., 289, 373.
- Sarazin, C.L. 1976, Ap. J., 208, 323.
- Schmidt, M. 1959, Ap. J., 129, 243.
- Schommer, R.A. and Sullivan, W.T. 1976, Ap. Let., 17, 191.
- Schweizer, F. 1976, Ap. J. Suppl., 31, 313.
 ----- 1977, Ap. J., 211, 324.
- Scoville N.Z. and Hersh, K. 1979, Ap. J., 229, 578.
- Scoville, N.Z. and Young, J.S. 1983, Ap. J., 265, 148 (SY).
- Scoville, N.Z., Sanders, D.B. and Clemens, D.P. 1986, Ap. J. Let., 310, L77.
- Scoville, N.Z., Yun, M.S., Clemens, D.P., Sanders, D.B. and Waller, W.H. 1987, Ap. J. Suppl., 63, 821.
- Seiden, P.E. and Gerola, H. 1979, Ap. J., 233, 56.
- Shu, F.H., Adams, F.C. and Lizano, S. 1987, preprint.
- Snell, R.L. and Schloerb, F.P. 1983, FCRAO Report # 220.
- Silk, J. 1986, in IAU Symposium No. 116, Luminous Stars and Associations in Galaxies, eds. C.W.H. De Loore, A.J. Willis, and P. Laskarides, (Dordrecht:Reidel).
- Smith, H.E. 1975, Ap. J., 199, 591.
- Smith, J. 1982, Ap. J., 261, 463.
- Smith, L.F., Biermann, P. and Mezger, P.G. 1978, Astr. Ap., 66, 65.
- Solomon, P.M., Sanders, D.B. and Rivolo, A.R. 1985, Ap. J. Let., 292, L19.
- Stark, A.A. 1979, Ph.D. dissertation, Princeton University.
- Strom, S.E., Strom, K.M., Grasdalen, G.L. and Capps, R.W. 1974, Ap. J. Let., 193, L7.
- Tacconi, L.J. and Young, Y.S. 1986, Ap. J., 308, 600.
- Talbot, R.J., Jr. 1980, Ap. J., 235, 821 (T80).

- Talbot, R.J., Jr., Jensen, E.B. and Dufour, R.J. 1979, Ap. J., 229, 91 (TJD).
- Telesco, C.M. and Harper, D.A. 1980, Ap. J., 235, 392.
- Tinsley, B.M. 1980, Fundamentals of Cosmic Physics, 5, 287.
- Toomre, A. and Toomre, J. 1972, Ap. J., 178, 623.
- Tubbs, A.D. 1982, Ap. J., 255, 458.
- Tully, R.B. 1972, Ph.D. dissertation, University of Maryland.
 ----- 1974a, Ap. J. Suppl., 27, 415.
 ----- 1974b, Ap. J. Suppl., 27, 437.
 ----- 1974c, Ap. J. Suppl., 27, 449.
- Tutukov A. and Krugel, E. 1981, Soviet Astr., 24, 539 (TK).
- van der Hulst, J.M. and Kennicutt, R.C., Jr. 1987, in Star Formation in Galaxies, ed. C. Persson, in press (vK).
- Verschuur, G.L. 1974, in Galactic and Extragalactic Radio Astronomy, eds. G.L. Verschuur and K.I. Kellermann, (New York:Springer-Verlag).
- Weliachew, L. and Gottesman, S.T. 1973, Astr. Ap., 24, 59.
- Woodward, P.R. 1978, Ann. Rev. Astron. Ap., 16, 555.
- Young, J.S. and Scoville, N.Z. 1982, Ap. J., 258, 467.
- Young, J.S. and Sanders, D.B. 1986, Ap. J., 302, 680.
- Young, J.S. 1987, IAU Symposium No. 115, Star Forming Regions, eds. M. Peimbert and J. Jugaku, (Reidel), in press.
- Young, J.S., Xie, S., Kenney, J.D. and Rice, W.L. 1987, A.J., submitted.
- Zanstra, H. 1931, Pub. Dominion Astroph. Obs., 4, 209.

